

# Spin-orbital Models in Optical Lattices

Von der Fakultät für Mathematik und Physik  
der Gottfried Wilhelm Leibniz Universität Hannover

zur Erlangung des Grades

Doktor der Naturwissenschaften  
Dr. rer. nat.

genehmigte Dissertation von

**M.Sc. Gaoyong Sun**

geboren am 27. August 1983 in Jiangsu, China

2014

Referent : Prof. Dr. Temo Vekua  
Koreferent : Prof. Dr. Luis Santos  
Tag der Promotion : 12.01.2015

*to my wife*



# Abstract

In this thesis, two types of spin-orbit coupled many-body systems of ultra-cold gases loaded in optical lattices are investigated by means of exact diagonalization and density matrix renormalization group methods. The ground state phases and the phase transitions are studied and determined by many different methods, such as level crossings of the low lying energy levels, fidelity susceptibility, following excitation energy gaps, correlation functions, and other order parameters.

It is shown that two component dipolar fermions or bosons in zig-zag optical lattices can simulate orbitally degenerate systems of solid state physics. Exotic phases and novel macroscopic behavior are found due to the Hund effect and fluctuations of the degenerate orbitals in the frustrated geometry, including a novel spin liquid phase with spontaneously broken  $SU(2)$  symmetry and unsaturated ferromagnetism, as well as topological order-by-disorder. The novel spin liquid phase is shown to result from bound states of magnons and kinks, whereas topological order-by-disorder stems from the instability of the paramagnetic state against the quantum fluctuations of orbitals. In addition, other interesting phases are also discussed, including a quartic dimerized phase with period four, boundary states with nonlocal entangled edge spins, and more.

We show as well that counter-propagating Raman lasers can realize other type of spin-orbital models that mimic relativistic spin-orbit coupling in condensed matter. Many phases of that model including rung singlet, Néel phase, ferromagnetic striped phase are found and characterized in ladder-like optical lattices.

We end the thesis with a recent work on fidelity susceptibility, which is a key technique to map phase transitions as those discussed in other parts of the thesis. We show in particular that the fidelity susceptibility near the Berezinskii-Kosterlitz-Thouless quantum phase transition does not diverge, but converges logarithmically.

Key words: spin-orbit coupling, dipolar, fidelity susceptibility.



# Zusammenfassung

In dieser Arbeit werden zwei Arten von Vielteilchensystemen mit Spin-Orbit Wechselwirkung im Kontext von ultrakalten Gasen in optischen Gittern mithilfe von exakter Diagonalisierung und der Dichtematrixrenormierungsgruppen-Methode (DMRG) untersucht. Die Grundzustandsphasen und Phasen-Übergänge werden auf verschiedene Arten charakterisiert, z.B. durch Level-Kreuzungen der niedrigen Energie Zustände, Fidelity-Suszeptibilitäten, Energie-Lücken Betrachtungen oder anderer Ordnungsparameter.

Es wird gezeigt, dass zwei-komponentige dipolare Fermionen in optischen Zick-Zack-Gittern ein System entarteter Orbitale aus der Festkörperphysik simulieren können. Aufgrund des Hund-Effekts und Fluktuationen der entarteten Orbitale in der frustrierten Geometrie können exotische Quantenphasen und neuartige makroskopische Effekte beobachtet werden, wie z.B. eine neuartige Spin-Liquid Phase mit spontan gebrochener  $SU(2)$  Symmetrie, nicht-saturierter Ferromagnetismus und ein Phänomen, das als topologischer Ordnungs-Unordnungs-Übergang bezeichnet wird. Die neuartige Spin-Liquid Phase wird durch gebundene Zustände von Magnonen und Kinks erklärt. Das Ordnungs-Unordnungs Phänomen lässt sich durch die Instabilität des Paramagnetischen Zustands gegen Quantenfluktuationen erklären. Darüberhinaus werden in dieser Arbeit weitere interessante Phasen beschrieben, wie z.B. eine quartische Dimer-Phase mit Periodizität 4 und Randzustände mit nichtlokal-verschränkten Rand-Spins.

Im nächsten Kapitel zeigt wie durch gegenläufige Raman-Laser ein weiteres Spin-Orbit-Modell, das eine relativistische Spin-Orbit Wechselwirkung nachahmt, experimentell realisiert werden kann. Viele Phasen dieses Modells, wie die Néel-Phase oder die ferromagnetische-gestreifte Phase werden in einem leiterartigen optischen Gitter gefunden und charakterisiert.

Schließlich wird die Fidelity-Suszeptibilität in der Nähe eines Berezinskii Kosterlitz Thouless Quanten Phasenübergangs untersucht. Es wird gezeigt, dass sie nicht divergiert, sondern logarithmisch langsam konvergiert.

Schlagnworte: Spin-Orbit Wechselwirkung, dipolare, Fidelity-Suszeptibilität.





# Contents

<b>Abstract</b>	<b>v</b>
<b>Zusammenfassung</b>	<b>vii</b>
<b>1 Introduction</b>	<b>1</b>
<b>2 Concepts</b>	<b>5</b>
2.1 Optical lattices . . . . .	5
2.2 Scattering theory . . . . .	8
2.3 Dipolar interactions . . . . .	12
2.4 Spin-orbital physics . . . . .	13
2.5 Hubbard models in optical lattices . . . . .	15
2.6 Perturbation theory . . . . .	19
2.7 Fidelity and fidelity susceptibility . . . . .	24
<b>3 Numerical methods</b>	<b>27</b>
3.1 Exact diagonalization . . . . .	27
3.2 Matrix product states . . . . .	32
3.2.1 Density matrix renormalization group . . . . .	32
3.2.2 Time evolution . . . . .	40
<b>4 Spin-orbital models of dipolar fermions in zig-zag optical lattices</b>	<b>45</b>
4.1 Introduction . . . . .	45
4.2 Spin-orbital model for fermions . . . . .	46
4.3 No Hund effect regime . . . . .	49
4.4 Relevant regime in solid-state systems . . . . .	51

---

4.5	Regime beyond solid-state systems . . . . .	54
4.6	Experimental realization . . . . .	61
4.7	Conclusion . . . . .	62
<b>5</b>	<b>Spin-orbital models of dipolar bosons in zig-zag optical lattices</b>	<b>65</b>
5.1	Introduction . . . . .	65
5.2	Spin-orbital model for bosons . . . . .	66
5.3	Ground state phases for classical orbitals . . . . .	67
5.4	Topological order-by-disorder . . . . .	69
5.5	Full ground state phase diagram . . . . .	72
5.6	Conclusion . . . . .	76
<b>6</b>	<b>Spin-orbit coupled fermions in ladder-like lattices</b>	<b>79</b>
6.1	Introduction . . . . .	79
6.2	Effective spin models for fermions . . . . .	80
6.3	USOC for decoupled chains . . . . .	82
6.4	USOC along the ladder rungs . . . . .	86
6.5	USOC along the ladder legs . . . . .	89
6.6	Two-leg ladder with a non-Abelian vector potential . . . . .	91
6.7	Experimental realizations . . . . .	94
6.8	Conclusion . . . . .	95
<b>7</b>	<b>Fidelity susceptibility at Berezinskii-Kosterlitz-Thouless transition</b>	<b>97</b>
7.1	Scaling of the FS at phase transitions . . . . .	97
7.2	Fidelity susceptibility at BKT transitions . . . . .	100
7.3	Fidelity susceptibility at BKT transitions in other lattice models . . .	101
7.4	Conclusion . . . . .	103
<b>8</b>	<b>Conclusions and outlook</b>	<b>105</b>
	<b>Bibliography</b>	<b>107</b>
	<b>Appendix</b>	<b>123</b>

<b>Contents</b>	<b>xi</b>
<b>A Wannier functions</b>	<b>123</b>
<b>B Peierls substitution</b>	<b>125</b>
<b>C On-site interaction energies of dipolar bosons</b>	<b>127</b>
<b>Acknowledgements</b>	<b>129</b>
<b>Publications</b>	<b>131</b>
<b>Curriculum Vitae</b>	<b>133</b>



# Chapter 1

## Introduction

Strongly correlated many-body systems, where interactions play the dominant role and particles are strongly entangled, are very intriguing and of broad interest both in condensed matter as well as in ultracold quantum gases communities. These systems exhibit novel phenomena, such as high-temperature superconductivity [1], spin liquid behavior realized in quantum magnets [2, 3], spin-charge separation in one dimensional electron systems [4], and so on. There are no general analytical methods for understanding such systems because of the strong interactions making the well known perturbation theory and mean-field like approximation schemes fail. Simulations, including both classical numerical simulations and quantum simulators, have been becoming a rapid developing field in modern physics, aiming to shed light on the understanding of the many body physics of strongly correlated systems. As a bonus one expects to find novel (exotic) states realized possibly beyond the solid state realization.

Quantum many-body systems cannot be exactly simulated by classical computers due to the exponentially increasing system size [5] with number of particles. One of the well known approaches is the numerical renormalization group method, initially developed for the Kondo problem, where the particles are formed into blocks and Hilbert space is truncated according to the lowest-lying energy eigenstates [6]. Nowadays, the most powerful numerical simulation for one-dimensional systems is the density matrix renormalization group (DMRG) [7, 8] method, a generalization of the numerical renormalization group for strongly correlated many-body systems.

Although we will mainly focus on DMRG calculations in one-dimension, it is important to note that generalizations of DMRG to two dimensional or higher dimensional systems, i.e. projected entangled pair states (PEPS) [9] and the multi-scale entanglement renormalization ansatz (MERA) [10], have been introduced and are being worked on intensively currently.

The idea of quantum simulation was first proposed by R. P. Feynman in 1982 [5]. Nowadays, many proposed simulators are explored for quantum simulations, for example those based on: polar molecules, neutral atoms, trapped ions, quantum dots, nuclear spins, etc. [11]. In real solid state materials, the interactions between the constituent particles are fixed by nature, being very difficult to modify. Optical lattices offer a controllable potential and geometries for trapping and manipulating quantum gases, making them promising candidates for quantum simulators [12, 13]. In addition quantum gases can mimic real solid state systems with adjustable coupling constants, allowing us to explore potentially vast phase diagrams not accessible by specific realization of condensed matter compound. New unconventional phases (exotic states of matter) can emerge with strong correlations by inducing long range dipolar interactions e.g. in polar molecules, Rydberg atoms, Coulomb interacting ionic chain, or by reducing dimensionality and enhancing quantum fluctuations, e.g. creating two-dimensional and one-dimensional geometries or ladder-like lattices.

A milestone development in quantum simulation is provided by the realization of the Bose-Hubbard model [14, 15] using ultracold quantum gases in optical lattices, after which many interesting proposals and experiments were carried on. Recently, spin-orbit coupled Bose-Einstein condensates [16] and spin-orbit coupled degenerate Fermi gases [17, 18] have been realized using counter-propagating Raman lasers, showing an interesting and tunable band structure. Degenerate  $p$ -bands are also realized by pumping bosons to excited states in optical lattices [19], showing a novel time-reversal symmetry breaking  $p_x \pm ip_y$  phase. Current and possible future experiments on ultra-cold gases have motivated us to study the ground state phases of spin-orbit coupled systems, especially for searching exotic phases.

The structure of his thesis is as follows. In chapter 2 we introduce key concepts employed later on in the thesis. Key numerical methods employed in our calculations

are discussed in chapter 3. Chapters 4 and 5 are devoted to the simulation of spin-orbital models using, respectively, fermions and bosons in zig-zag optical lattices. Chapter 6 analyzes a different type of realization of spin-orbit models in ladder like lattices. Finally chapter 7 analyzes in detail the behavior of a key technique for the analysis of phase transitions through this thesis, the so-called fidelity susceptibility, in the vicinity of a Berezinskii-Kosterlitz-Thouless transition.





# Chapter 2

## Concepts

In this chapter we introduce some key ideas and concepts that will be of crucial importance later on in later chapters, including the idea of optical lattices, the basics of scattering theory, the physics of dipolar systems and systems with spin-orbit coupling, the Hubbard model, perturbation theory, and the ideas of fidelity and fidelity susceptibility.

### 2.1 Optical lattices

Optical lattices, produced by counter-propagating laser beams, provide a controllable set-up for simulating many-body systems with ultra-cold atomic and molecular gases [12, 13]. An optical lattice is based on the so-called AC Stark effect. When placing an atom into a laser light field  $E(\mathbf{r}, t)$ , a dipole moment  $\mathbf{d}$  is induced as,

$$d_i = \sum_{j=x,y,z} \alpha_{ij}(\omega_L) E_j(\mathbf{r}, t) \quad (2.1.1)$$

where  $\alpha_{ij}(\omega_L)$  is the polarizability, which depends on the laser frequency  $\omega_L$ . If one of the excited states at frequency  $\omega_1$  is much closer to the resonance than the others, the polarizability will be proportional to the laser detuning from the resonance  $\Delta = \omega_L - \omega_1$ , and the energy shift will be proportional to the laser intensity  $I(\mathbf{r})$  via the AC Stark effect as

$$\Delta E(\mathbf{r}) = \mathbf{d} \cdot \mathbf{E} = \sum_{i,j=x,y,z} \alpha_{ij}(\omega_L) \langle E_i(\mathbf{r}) E_j(\mathbf{r}) \rangle \propto \frac{I(\mathbf{r})}{\Delta} \quad (2.1.2)$$

Thus the atoms will feel an optical potential

$$V_{opt} = \Delta E(\mathbf{r}) \propto \frac{I(\mathbf{r})}{\Delta} \quad (2.1.3)$$

The optical potential depends on the laser intensity  $I(\mathbf{r})$  and the sign of the laser detuning  $\Delta$ . If the laser is red-detuned ( $\Delta < 0$ ), the atoms are attracted to the maximal intensity of the laser beams. If the laser is blue-detuned ( $\Delta > 0$ ), the atoms gather at the minimal intensity of the laser beams [12,13]. Below we discuss some examples of possible optical lattice geometries:

### (a) One dimensional (1D) lattices

Let us consider two plane waves  $A_1 = V_1 e^{ikx} \mathbf{e}_1$  and  $A_2 = V_2 e^{-ikx} \mathbf{e}_2$  counter-propagating in  $x$  direction, with wave vector  $k = \frac{2\pi}{\lambda}$ , amplitudes  $V_1, V_2$ , and polarization  $\mathbf{e}_1, \mathbf{e}_2$ . The intensity distribution, considering  $\mathbf{e}_1 = \mathbf{e}_2$ , is

$$I = |A_1 + A_2|^2 = V_1^2 + V_2^2 + 2V_1V_2 \cos(2kx) = V_0 \cos^2(kx) \quad (2.1.4)$$

where we have assumed equal amplitudes  $V_1 = V_2 = V$ , and  $V_0 = 4V^2$ . Sufficiently cold atoms or molecules may be loaded at the lattice minima, realizing in this way a 1D lattice gas.

### (b) Two dimensional (2D) square lattices

Two pairs of counterpropagating lasers may be employed to realize a 2D square lattice. Two pairs of plane waves  $V_1 e^{\pm i\mathbf{k}_1 \cdot \mathbf{r}} \mathbf{e}_1$  and  $V_2 e^{\pm i\mathbf{k}_2 \cdot \mathbf{r}} \mathbf{e}_2$  result in an intensity distribution of the form:

$$I = 4V_1^2 \cos^2(\mathbf{k} \cdot \mathbf{r}_1) + 4V_2^2 \cos^2(\mathbf{k} \cdot \mathbf{r}_2) + 8V_1V_2 \cos(\mathbf{k} \cdot \mathbf{r}_1) \cos(\mathbf{k} \cdot \mathbf{r}_2) \mathbf{e}_1 \cdot \mathbf{e}_2 \quad (2.1.5)$$

If  $\mathbf{k} \cdot \mathbf{r}_1 = kx$ ,  $\mathbf{k} \cdot \mathbf{r}_2 = ky$ ,  $\mathbf{e}_1 \cdot \mathbf{e}_2 = 0$ ,  $V_1 = V_2 = V$ , and  $V_0 = 4V^2$ , the intensity distribution acquires the form:

$$I = V_0 (\cos^2(kx) + \cos^2(ky)) \quad (2.1.6)$$

This intensity distribution is plotted in Fig.2.1. Clearly the intensity minima (or maxima) form a square lattice.

### (c) Two dimensional honeycomb and triangular lattices

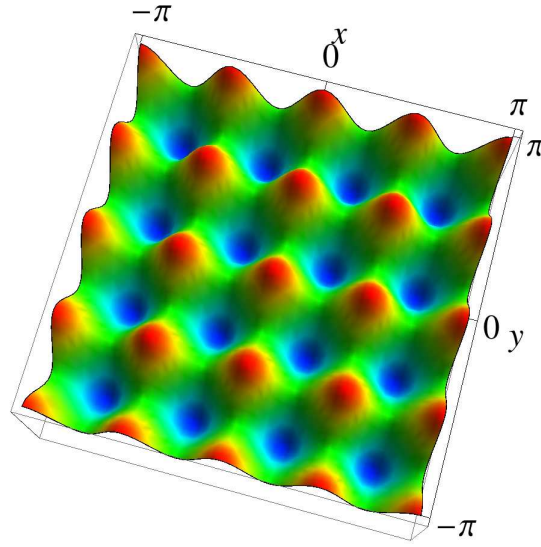


Figure 2.1: Two dimensional optical lattice potential with wave vector  $k = 2$ , and  $V_0 = 1$ . The particles are trapped in the potential minima (blue holes) in the experiments.

Honeycomb and triangular lattices may be created by interfering three plane waves [20]. Let us consider for example three plane waves propagating at an angle  $2\pi/3$  between each other, i.e.  $A_{j=1,2,3} = V_j e^{i\mathbf{k}_j \cdot \mathbf{r}} \mathbf{e}_j$ , with  $\mathbf{k}_1 \cdot \mathbf{r} = kx$ ,  $\mathbf{k}_2 \cdot \mathbf{r} = -\frac{1}{2}kx + \frac{\sqrt{3}}{2}ky$ ,  $\mathbf{k}_3 \cdot \mathbf{r} = -\frac{1}{2}kx - \frac{\sqrt{3}}{2}ky$ . The intensity distribution acquires the form:

$$I = V_1^2 + V_2^2 + V_3^2 + 2V_1V_2 \cos(\mathbf{k}_1 \cdot \mathbf{r} - \mathbf{k}_2 \cdot \mathbf{r}) \mathbf{e}_1 \cdot \mathbf{e}_2 + 2V_1V_3 \cos(\mathbf{k}_1 \cdot \mathbf{r} - \mathbf{k}_3 \cdot \mathbf{r}) \mathbf{e}_1 \cdot \mathbf{e}_3 + 2V_2V_3 \cos(\mathbf{k}_2 \cdot \mathbf{r} - \mathbf{k}_3 \cdot \mathbf{r}) \mathbf{e}_2 \cdot \mathbf{e}_3 \quad (2.1.7)$$

If  $\mathbf{e}_1 = \mathbf{e}_2 = \mathbf{e}_3$ ,  $V_1 = V_2 = V_3 = V$ , and  $V_0 = 4V^2$ , then:

$$I = V_0 \left[ \frac{3}{4} + \frac{1}{2} \left( \cos\left(\frac{3}{2}kx - \frac{\sqrt{3}}{2}ky\right) + \cos\left(\frac{3}{2}kx + \frac{\sqrt{3}}{2}ky\right) + \cos(\sqrt{3}ky) \right) \right] \quad (2.1.8)$$

The potential of Eq.(2.1.8) is plotted in Fig.2.2 (Left) with wave vector  $k = 3$ , and amplitude  $V_0 = 1$ . The potential minima (dark blue regions) form a honeycomb lattice. With the same set up we may realized a triangular lattice, if we employ  $\mathbf{e}_1 \cdot \mathbf{e}_2 = \mathbf{e}_1 \cdot \mathbf{e}_3 = \mathbf{e}_2 \cdot \mathbf{e}_3 = \cos(2\pi/3) = -1/2$ , resulting in an intensity:

$$I = V_0 \left[ \frac{3}{4} - \frac{1}{4} \left( \cos\left(\frac{3}{2}kx - \frac{\sqrt{3}}{2}ky\right) + \cos\left(\frac{3}{2}kx + \frac{\sqrt{3}}{2}ky\right) + \cos(\sqrt{3}ky) \right) \right] \quad (2.1.9)$$

This intensity will give the triangular geometry (blue color regions) shown in Fig.2.2 (Right) with the wave vector  $k = 3$ , and  $V_0 = 1$ .

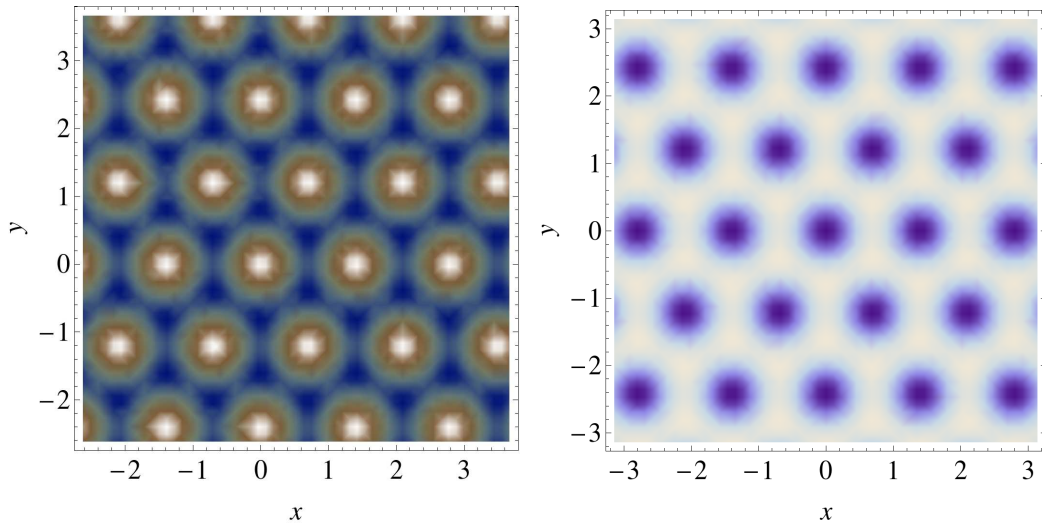


Figure 2.2: Two dimensional honeycomb (Left) and triangular (Right) optical lattice potential with wave vector  $k = 3$ , and  $V_0 = 1$ . The particles are trapped in the potential minima (dark blue color regions) in the experiments.

For the creation of more complex lattice geometries, one may use standard super-lattice techniques based on the incoherent superposition of aligned optical lattices [21,22]. For instance, one may combine another lattice potential  $I_1 = V_1 \cos(\frac{\sqrt{3}}{4}ky + \frac{\pi}{4})$  to the triangular potential Eq.(2.1.9), then the super-lattice potential

$$\begin{aligned}
 I_{sup} &= I + I_1 \\
 &= V_0 \left[ \frac{3}{4} - \frac{1}{4} \left( \cos\left(\frac{3}{2}kx - \frac{\sqrt{3}}{2}ky\right) + \cos\left(\frac{3}{2}kx + \frac{\sqrt{3}}{2}ky\right) + \cos(\sqrt{3}ky) \right) \right] \\
 &\quad + V_1 \cos\left(\frac{\sqrt{3}}{4}ky + \frac{\pi}{4}\right)
 \end{aligned} \tag{2.1.10}$$

will realize a zig-zag lattice geometry, as shown in Fig.2.3 (this specific geometry will be employed later on in this thesis). We may use similar techniques to create other lattice geometries [12, 15, 23].

## 2.2 Scattering theory

Two body scattering plays a crucial role in the understanding of ultra-cold gases. The two-body collision theory may be found in many textbooks or review articles [24–28]. In the following, we shortly review the scattering physics of two

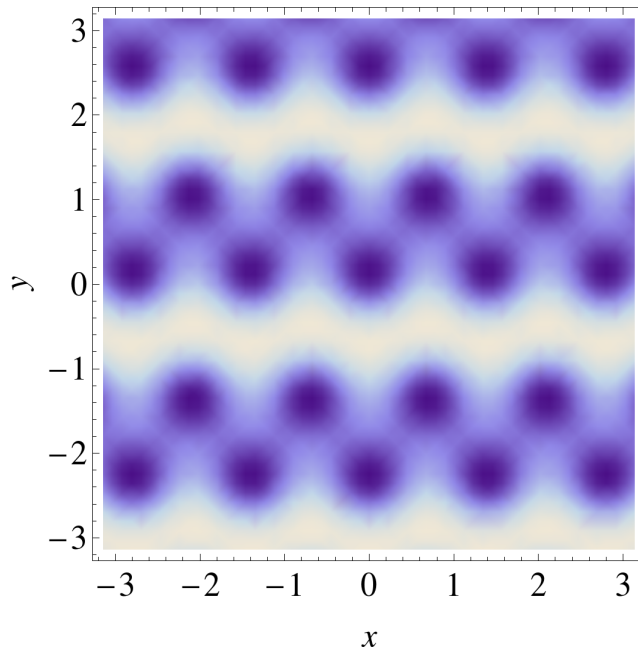


Figure 2.3: Two dimensional zig-zag optical lattice potential with wave vector  $k = 3$ , amplitudes  $V_0 = 1$  and  $V_1 = 1.5V_0$ . The particles are trapped in the potential minima (blue color regions) in the experiments.

particles and take the contact interaction as an example (see references [24–28] for details). Let us consider two particles with mass  $m_1$  and  $m_2$  interacting via the interaction potential  $V(\mathbf{r}_1 - \mathbf{r}_2)$ . In the center-of-mass reference frame, the motion of the relative coordinate is given by the Schrödinger equation:

$$\left( \frac{p^2}{2m_r} + V(\mathbf{r}) \right) \psi_{\mathbf{k}}(\mathbf{r}) = E_{\mathbf{k}} \psi_{\mathbf{k}}(\mathbf{r}) \quad (2.2.1)$$

with the reduced mass  $m_r = m_1 m_2 / (m_1 + m_2)$ , relative position  $\mathbf{r} = \mathbf{r}_1 - \mathbf{r}_2$  and momentum  $\mathbf{p} = \mathbf{p}_1 - \mathbf{p}_2 = \hbar \mathbf{k}$ , and the energy  $E_k = \frac{\hbar^2 k^2}{2m_r}$ . The solution of the Schrödinger equation should have a large distance ( $r \rightarrow \infty$  or  $r \gg r_0$ ) asymptotic form,

$$\psi \approx e^{ikz} + f(k, \theta) \frac{e^{ikr}}{r}, \quad (2.2.2)$$

representing the incoming wave  $e^{ikz}$  plus the outgoing spherical wave  $f(k, \theta) \frac{e^{ikr}}{r}$ , where  $\theta$  is the scattering angle between the  $z$ -direction and the direction of scattered particles,  $r_0$  is the range of interaction  $V(\mathbf{r})$  and  $f(k, \theta)$  is called the scattering amplitude. To find the form of  $f(k, \theta)$ , we need to solve the Schrödinger equation.

One may expand the wave function in terms of Legendre polynomials  $P_l(\cos \theta)$  if the interaction potential has spherical symmetry,  $V(\mathbf{r}) = V(r)$

$$\psi = \sum_{l=0}^{\infty} A_l P_l(\cos \theta) R_{kl}(r) \quad (2.2.3)$$

where the  $A_l$  are constants and the radial wave function  $R_{kl}(r)$  satisfies the equation

$$R''_{kl}(r) + \frac{2}{r} R'_{kl}(r) + \left[ k^2 - \frac{l(l+1)}{r^2} - \frac{2m_r}{\hbar^2} V(r) \right] R_{kl}(r) = 0 \quad (2.2.4)$$

After solving equation Eq.(2.2.4) and performing some calculations, the scattering amplitude could be written as

$$\begin{aligned} f(k, \theta) &= \frac{1}{2ik} \sum_{l=0}^{\infty} (2l+1)(e^{2i\delta_l} - 1) P_l(\cos \theta) \\ &= \sum_{l=0}^{\infty} (2l+1) f_l P_l(\cos \theta), \end{aligned} \quad (2.2.5)$$

where  $l = 0, 1, 2, \dots$  refer to the  $s, p, d, \dots$  partial wave contributions.  $\delta_l$  are the phase shifts of the corresponding partial waves, and  $f_l = \frac{1}{2ik}(e^{2i\delta_l} - 1)$  are called the partial scattering amplitudes. From the scattering amplitudes one may get the total scattering cross sections

$$\begin{aligned} \sigma &= 2\pi \int_0^\pi |f(k, \theta)|^2 \sin \theta d\theta \\ &= \frac{4\pi}{k^2} \sum_l (2l+1) \sin^2 \delta_l \end{aligned} \quad (2.2.6)$$

The phase shifts  $\delta_l$  depend on the form of  $V(r)$ . For an interaction decreasing with distance as  $V(r) \approx \beta r^{-n}$  and in the low energy scattering theory ( $kr_0 \ll 1$ ), the phase shifts  $\delta_l$  vary as

$$\delta_l \propto \begin{cases} k^{2l+1}, & \text{for } l < \frac{n-3}{2} \\ k^{n-2}, & \text{for } l \geq \frac{n-3}{2} \end{cases} \quad (2.2.7)$$

For example, for van der Waals potential  $n = 6$ , only  $l = 0$  and  $l = 1$  satisfy the first condition of Eq.(2.2.7), whereas all other phase shifts of  $l$ -th partial waves are given by the second condition of Eq.(2.2.7). In low energy limit ( $k \rightarrow 0$ ), we may only consider the  $l = 0$  (s-wave scattering) partial wave. The s-wave scattering length is defined by

$$a_s = -f_0 = -\lim_{k \rightarrow 0} \frac{\tan \delta_0}{k} = -\frac{\delta_0}{k} \quad (2.2.8)$$

Thus the total cross section of low energy scattering is

$$\sigma = \frac{4\pi\delta_0^2}{k^2} = 4\pi a_s^2 \quad (2.2.9)$$

However, if we consider the long-range dipole-dipole interaction ( $n = 3$ ), all the partial waves will contribute to the low energy scattering as shown in the second condition of Eq.(2.2.7).

Instead of solving the Schrödinger equation, one may calculate the scattering properties by the Born approximation, that is the first order approximation of the perturbation theory. It is given by

$$f_0 = -\frac{m_r}{2\pi\hbar^2} \int e^{i(\mathbf{k}-\mathbf{k}')\cdot\mathbf{r}} V(\mathbf{r}) d\mathbf{r} \quad (2.2.10)$$

With it, one may easily compute the  $s$ -wave scattering length  $f_0$  for contact interaction  $V(\mathbf{r}_1 - \mathbf{r}_2) = g\delta(\mathbf{r}_1 - \mathbf{r}_2)$ , which is

$$a_s = -f_0 = \frac{gm_r}{2\pi\hbar^2} = \frac{gm}{4\pi\hbar^2} \quad (2.2.11)$$

Then we may get the effective interaction in terms of scattering length

$$V_{eff}(\mathbf{r}) = g\delta(\mathbf{r}) = \frac{4\pi\hbar^2 a_s}{m} \delta(\mathbf{r}) \quad (2.2.12)$$

where the masses of the two particles are assumed the same ( $m_r = m/2$ ). This potential is called pseudo-potential. Hence, the true short-range interaction potential can be replaced by the pseudo potential with the same  $s$ -wave scattering length. The above discussion is for distinguishable particles. For indistinguishable particles, one needs to consider the symmetric wave function for bosons or antisymmetric wave functions for fermions, which are

$$\psi \approx (e^{ikz} \pm e^{-ikz}) + (f(k, \theta) \pm f(k, \pi - \theta)) \frac{e^{ikr}}{r} \quad (2.2.13)$$

The  $\theta$  ranges from  $0 \leq \theta \leq \pi/2$ . The total cross sections are

$$\begin{aligned} \sigma &= 2\pi \int_0^{\pi/2} |f(k, \theta) \pm f(k, \pi - \theta)|^2 \sin \theta d\theta \\ &= \frac{8\pi}{k^2} \sum_{l, \text{even}(l, \text{odd})} (2l+1) \sin^2 \delta_l \end{aligned} \quad (2.2.14)$$

where "+" refers to bosons and "-" refers to fermions. For bosons, only even partial waves ( $s$ -wave,  $d$ -wave, ...) contribute to the cross sections, while for fermions, only odd partial waves ( $p$ -wave,  $f$ -wave, ...) contribute.

## 2.3 Dipolar interactions

The interaction between two particles with dipole moments along unit vectors  $\hat{\mathbf{e}}_1$  and  $\hat{\mathbf{e}}_2$ , is described by [28, 29],

$$V_{dd} = \frac{c_{dd}}{4\pi} \frac{\hat{\mathbf{e}}_1 \cdot \hat{\mathbf{e}}_2 - 3(\hat{\mathbf{e}}_1 \cdot \hat{\mathbf{r}})(\hat{\mathbf{e}}_2 \cdot \hat{\mathbf{r}})}{r^3}, \quad (2.3.1)$$

where  $\hat{\mathbf{r}} = \mathbf{r}/r$  is the unit relative vector between the two dipoles. The coupling constant is  $c_{dd} = \mu_0 \mu^2$  for magnetic dipole moments and  $c_{dd} = d^2/\epsilon_0$  for electric dipole moments, where  $\mu_0$  is the magnetic permeability,  $\epsilon_0$  is the vacuum electric permittivity, and  $\mu$  and  $d$  are, respectively, the magnitude of the magnetic and electric dipole moments. If the dipolar particles are polarized along the same direction  $z$ , the dipole-dipole interaction of Eq.(2.3.1) is reduced to

$$V_{dd} = \frac{c_{dd}}{4\pi} \frac{1 - 3 \cos^2 \theta}{r^3} \quad (2.3.2)$$

where  $\theta$  is the angle between the direction of polarization  $z$  and the relative position of these two dipole moments. The dipole-dipole interaction could be either repulsive or attractive depending on the angle  $\theta$ . As the interaction of dipolar particles decays as  $r^{-3}$ , the scattering of dipolar particles is quite different from that for the contact interaction since all the partial waves will equally contribute to the scattering amplitude.

The scattering properties of the dipole-dipole interaction may be described by multichannel scattering theory in the low energy limit, from which the second-order perturbation induces an effective potential for  $l = 0$  that decays as van der Waals interaction ( $r^{-6}$ ) at large distances. Therefore, by replacing the van der Waals interaction by the pseudo-potential, the effective interaction for dipolar particles is given by [30, 31]

$$V_{eff}(r) = \frac{4\pi a_s}{m} \delta(\mathbf{r}) + \frac{c_{dd}}{4\pi} \frac{1 - 3 \cos^2 \theta}{r^3} \quad (2.3.3)$$

where  $a_s$  is the  $s$ -wave scattering length. It is important to note that the scattering length could be tuned by Feshbach resonances. Near Feshbach resonances, the scattering length  $a$  is given by [12, 28, 29]

$$a = a_{bg} \left( 1 - \frac{\Delta}{B - B_0} \right) \quad (2.3.4)$$



where  $a_{bg}$  is the background scattering length,  $B$  is the external magnetic field,  $B_0$  is resonance position and  $\Delta$  is the resonance width.

## 2.4 Spin-orbital physics

Spin-orbit coupling, which describes the interaction between the spin and the orbital degrees of freedom, is related to a variety of phenomena in physics, such as topological insulators, Majorana fermions, orbitally-degenerate states, and more. There are two types of spin-orbit coupling namely relativistic and non-relativistic according to the interactions between the spin of the particle and its orbital motion. In the following, we give a brief introduction to these two types of spin-orbit coupling.

### (a) Relativistic Spin-orbit Coupling

Relativistic spin-orbit coupling describes linear coupling between the spin of the particle and its orbital motion [32], following Pauli approximation of the relativistic Dirac equation describing spin-1/2 particles,  $H_{soc} \approx \mathbf{k} \cdot \boldsymbol{\sigma}$ , where  $\hbar\mathbf{k}$  refers to the momentum with  $\mathbf{k} = (k_x, k_y, k_z)$ , and  $\boldsymbol{\sigma} = (\sigma^x, \sigma^y, \sigma^z)$  are the Pauli matrices connected to the spin  $\mathbf{S} = \hbar\boldsymbol{\sigma}/2$ . In solid-state physics, there are two kinds of important relativistic spin-orbit coupling, one is the Rashba spin-orbit coupling [33] given by the interaction  $H_{soc}^R = \alpha_R(k_x\sigma^y - k_y\sigma^x)$ , the other one is linear Dresselhaus spin-orbit coupling [34] given by the interaction  $H_{soc}^D = \alpha_D(k_x\sigma^y + k_y\sigma^x)$ .

Let us consider a 1D system to illustrate the physics related to spin-orbit coupling. The single-particle Hamiltonian with equal contributions of Rashba type and Dresselhaus type spin-orbit couplings (i.e.  $H_{soc} = \alpha k_x\sigma^y$ ) and the presence of Zeeman fields is:

$$H = \frac{p_x^2}{2m}\sigma^0 + \frac{\alpha}{\hbar}p_x\sigma^y - \frac{h}{2}\sigma^y + \frac{\delta}{2}\sigma^z \quad (2.4.1)$$

$\sigma^0$  is the identical matrix,  $\alpha$  is the spin-orbit coupling constant,  $h$ ,  $\delta$  are the Zeeman fields, and  $p_x = \hbar k_x$  is the momentum. The single particle spectrum for  $h = 0$  is

$$E^\pm = \frac{\hbar^2 k_x^2}{2m} \pm \sqrt{(\alpha k_x)^2 + (\delta/2)^2} \quad (2.4.2)$$

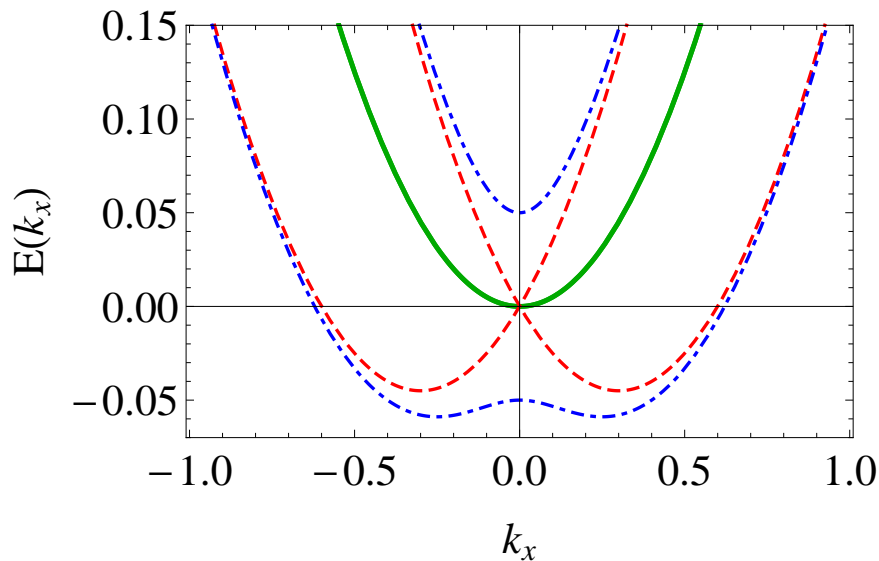


Figure 2.4: Single-particle energy spectra for 1D system. The green solid lines show the band structure of free particles  $\alpha = 0, \delta = 0$ , the red dashed lines show the band structure with only spin-orbit coupling  $\alpha = 0.3, \delta = 0$ , the blue dot-dashed lines show the band structure with spin-orbit coupling and Zeeman field  $\alpha = 0.3, \delta = 0.1$ .

The energy spectra for spin up and spin down particles have the same quadratic functions (green solid lines in Fig.2.4). With only spin-orbit coupling, the single-particle energy spectra splits, with momenta shift  $k'_x = k_x \pm k_0$  (with  $k_0 = \frac{\alpha m}{\hbar^2}$ ) (red dashed lines in Fig.2.4). When the Zeeman field  $\delta$  is added, a gap  $\Delta E = \delta$  opens (blue dot-dashed lines in Fig.2.4). For a sufficiently low chemical potential (or density) we may project out the higher band, realizing spinless fermions. By adding the s-wave superconductor term  $\Delta\psi_\uparrow\psi_\downarrow$  to the spin-orbit Hamiltonian Eq.(2.4.1), one may engineer Majorana fermions similar to the Kitaev toy model for spinless fermions [35, 36].

The Hamiltonian Eq.(2.4.1) with spin-orbit coupling may be easily written in a gauge form by subtracting a constant as

$$H = \frac{1}{2m}(p_x - A_x)^2 - \frac{\hbar}{2}\sigma^y + \frac{\delta}{2}\sigma^z, \quad (2.4.3)$$

where  $A_x = -\frac{\alpha m}{\hbar}\sigma^y = -\hbar k_0\sigma^y$  is the synthetic gauge potential that does not commute with the scalar potential  $\Phi = -\frac{\hbar}{2}\sigma^y + \frac{\delta}{2}\sigma^z$ . We come back to this type of spin-orbit coupling in chapter 6.

### (b) Non-relativistic Spin-orbit Coupling

The non-relativistic spin-orbit coupling describes orbitally degenerate systems without Dirac-like linear coupling term, in contrast to the relativistic spin-orbit coupling. This type of model was first introduced by Kugel and Khomskii to describe the magnetic properties of the strongly correlated perovskite system  $\text{KCuF}_3$  [37,38],

$$H = \frac{t^2}{U} \sum_{\langle ij \rangle} [4(\mathbf{S}_i \cdot \mathbf{S}_j)(\tau_i^\alpha - \frac{1}{2})(\tau_j^\alpha - \frac{1}{2}) + (\tau_i^\alpha + \frac{1}{2})(\tau_j^\alpha + \frac{1}{2}) - 1], \quad (2.4.4)$$

where the  $\mathbf{S}_i$  denotes spin degrees of freedom, the  $\tau_i^\alpha$  denotes orbital degrees of freedom, with  $\alpha = (a, b, c)$  and  $\tau_i^{a,b} = \frac{1}{4}(-\sigma_i^z \pm \sqrt{3}\sigma_i^x)$  and  $\tau_i^c = \frac{1}{2}\sigma_i^z$ . The Kugel-Khomskii model describes the interplay of spin and orbital degrees of freedom via the super-exchange interaction. The additional orbital freedom generates richer physics than that for the purely spin model. The interaction between spin and orbital degrees of freedom suppresses long-range order making disordered phases i.e. spin liquid exist. In chapter 4, we will derive the Kugel-Khomskii-like spin-orbital models for dipolar particles in the  $p$ -bands of optical lattices.

## 2.5 Hubbard models in optical lattices

The Hubbard model plays an important role in theoretical solid state physics due to its simplicity and generality. It contains the simplest form of kinetic and interaction terms. When particles are placed in deep optical lattices, they behave similarly to electrons in solid crystals because of the tight binding properties of the lattice localizing them near the minima potential. Thus Wannier functions will be used to describe the low energy physics as one does in solid-state physics. In the following, we derive the multi-band Hubbard model for two-component particles (fermions and bosons). Consider two-component particles trapped in a lattice potential  $V(\mathbf{r})$ . The

Hamiltonian has the following second quantization form [3],

$$\begin{aligned}
H = & \sum_{\sigma} \int \psi_{\sigma}^{\dagger}(\mathbf{r}) \left[ -\frac{\hbar^2}{2m} \nabla^2 + V(\mathbf{r}) \right] \psi_{\sigma}(\mathbf{r}) d\mathbf{r} \\
& + \sum_{\sigma, \sigma'} \int \psi_{\sigma}^{\dagger}(\mathbf{r}_1) \psi_{\sigma'}^{\dagger}(\mathbf{r}_2) \frac{U(\mathbf{r}_1 - \mathbf{r}_2)}{2} \psi_{\sigma'}(\mathbf{r}_2) \psi_{\sigma}(\mathbf{r}_1) d\mathbf{r}_1 d\mathbf{r}_2
\end{aligned} \tag{2.5.1}$$

where  $\psi_{\sigma}(\mathbf{r})$  and the  $\psi_{\sigma}^{\dagger}(\mathbf{r})$  are particle annihilation and creation operators at position  $\mathbf{r}$ ,  $V(\mathbf{r})$  is on-site lattice potential, and  $U(\mathbf{r}_1 - \mathbf{r}_2)$  is the interaction potential between the particles.  $m$  is the mass of single particles, and  $\sigma$  and  $\sigma'$  represent the spin indices that in the case of neutral atoms usually enumerate different hyperfine components. One may expand the field operator in terms of Bloch states  $\phi_{\alpha\mathbf{k}}(\mathbf{r})$  or Wannier functions  $w_{\alpha}(\mathbf{r} - \mathbf{R}_j)$  (see Appendix A for details) [3],

$$\psi_{\sigma}(\mathbf{r}) = \sum_{\alpha, \mathbf{k}} \phi_{\alpha\mathbf{k}}(\mathbf{r}) c_{\alpha\mathbf{k}\sigma} = \sum_{\alpha, j} w_{\alpha}(\mathbf{r} - \mathbf{R}_j) c_{\alpha j\sigma} \tag{2.5.2}$$

where  $c_{\alpha\mathbf{k}\sigma}$  ( $c_{\alpha j\sigma}$ ) are the annihilation operations, in  $\mathbf{k}$  space and real space, respectively. The coefficient  $\alpha$  denotes the band,  $\mathbf{k}$  is the wave number in the first Brioullin zone, and  $j$  is the real space position. Substituting the decompositions Eq.(2.5.2) into Eq.(2.5.1), one may arrive at the multi-band Hubbard model with nearest neighbour tunneling and on-site interactions (here we consider  $p$ -bands,  $\alpha = p_x$  or  $p_y$ ),

$$H = H_k + H_{int} \tag{2.5.3}$$

where  $H_k$  is the kinetic part describing the particles hopping from one site to another or one band to another

$$H_k = - \sum_{\alpha, j, \sigma} \left[ t_{\alpha} (c_{\alpha, j, \sigma}^{\dagger} c_{\alpha, j+1, \sigma} + c_{\alpha, j+1, \sigma}^{\dagger} c_{\alpha, j, \sigma}) + \lambda_{\alpha} c_{\alpha, j, \sigma}^{\dagger} c_{\bar{\alpha}, j, \sigma} \right] \tag{2.5.4}$$

and  $H_{int}$  is the on-site interaction between particles

$$\begin{aligned}
H_{int} = & \frac{1}{2} \sum_{\alpha, j, \sigma, \sigma'} U_{\alpha} c_{\alpha, j, \sigma}^{\dagger} c_{\alpha, j, \sigma'}^{\dagger} c_{\alpha, j, \sigma'} c_{\alpha, j, \sigma} \\
& + \frac{1}{2} \sum_{\alpha, j, \sigma, \sigma'} U_{\alpha\bar{\alpha}} c_{\alpha, j, \sigma}^{\dagger} c_{\bar{\alpha}, j, \sigma'}^{\dagger} c_{\bar{\alpha}, j, \sigma'} c_{\alpha, j, \sigma} \\
& + \frac{1}{2} \sum_{\alpha, \beta, j, \sigma, \sigma'} J_{\alpha\beta} c_{\alpha, j, \sigma}^{\dagger} c_{\beta, j, \sigma'}^{\dagger} c_{\beta, j, \sigma'} c_{\bar{\alpha}, j, \sigma}
\end{aligned} \tag{2.5.5}$$

The tunneling coefficients  $t_\alpha, \lambda_\alpha$  and the interaction coefficients  $U_\alpha, U_{\alpha\bar{\alpha}}, J_{\alpha\beta}$  are,

$$t_\alpha = - \int w_\alpha^*(\mathbf{r} - \mathbf{R}_j) \left[ -\frac{\hbar^2}{2m} \nabla^2 + V(\mathbf{r}) \right] w_\alpha(\mathbf{r} - \mathbf{R}_{j+1}) d\mathbf{r} \quad (2.5.6)$$

$$\lambda_\alpha = - \int w_\alpha^*(\mathbf{r} - \mathbf{R}_j) \left[ -\frac{\hbar^2}{2m} \nabla^2 + V(\mathbf{r}) \right] w_{\bar{\alpha}}(\mathbf{r} - \mathbf{R}_j) d\mathbf{r} \quad (2.5.7)$$

$$U_\alpha = \int |w_\alpha(\mathbf{r}_1 - \mathbf{R}_j)|^2 U(\mathbf{r}_1 - \mathbf{r}_2) |w_\alpha(\mathbf{r}_2 - \mathbf{R}_j)|^2 d\mathbf{r}_1 d\mathbf{r}_2 \quad (2.5.8)$$

$$U_{\alpha\bar{\alpha}} = \int |w_\alpha(\mathbf{r}_1 - \mathbf{R}_j)|^2 U(\mathbf{r}_1 - \mathbf{r}_2) |w_{\bar{\alpha}}(\mathbf{r}_2 - \mathbf{R}_j)|^2 d\mathbf{r}_1 d\mathbf{r}_2 \quad (2.5.9)$$

$$J_{\alpha\beta} = \int w_\alpha^*(\mathbf{r}_1 - \mathbf{R}_j) w_\beta^*(\mathbf{r}_2 - \mathbf{R}_j) U(\mathbf{r}_1 - \mathbf{r}_2) w_{\bar{\beta}}(\mathbf{r}_2 - \mathbf{R}_j) w_{\bar{\alpha}}(\mathbf{r}_1 - \mathbf{R}_j) d\mathbf{r}_1 d\mathbf{r}_2 \quad (2.5.10)$$

The coefficients  $\alpha$  and  $\beta$  specify the  $p$ -bands indices  $(p_x, p_y)$ , and  $\bar{\alpha}$  and  $\bar{\beta}$  always refer to the opposite bands of  $\alpha$  and  $\beta$ , respectively. There are two terms in the kinetic part  $H_k$ . One is the  $t_\alpha$  term that describes the particles tunneling from one site to its nearest neighbour sites, the other one is  $\lambda_\alpha$  terms that describes the particles hopping only on different bands in a single site. The first line in Eq.(2.5.5) describes the on-site density-density interaction of two particles in one of the  $p_x$  or  $p_y$  bands. The second line in Eq.(2.5.5) represents the on-site interaction of two particles in different bands. The last line in Eq.(2.5.5) are the Hund interaction terms including both the Hund exchange interaction when two particles occupy different bands and the pair hopping terms of two particles tunneling from one band to another. Hereafter we simply consider  $t_{p_x} = t_{p_y} = t$ ,  $\lambda_{p_x} = \lambda_{p_y} = \lambda$ ,  $U_{p_x} = U_{p_y} = U$  and  $U_{p_x, p_y} = U_{p_y, p_x} = V$  due to the symmetric properties (no difference) of  $p_x$  and  $p_y$  bands. If Wannier functions are real functions, the coefficients  $J_{\alpha\beta}$  will have the same expression, which is  $J_{p_x, p_x} = J_{p_y, p_y} = J_{p_x, p_y} = J_{p_y, p_x} = J_H$ . If the interaction is the contact interaction, then  $U_\perp = J_H$ . So far we have discussed the general Hubbard model for both fermions and bosons. In the following, we will discuss the  $p$ -bands fermionic Hubbard model and the bosonic Hubbard model separately.

### (a). Fermionic Hubbard model

Fermions obey the anti-commutation relations, which are

$$\{c_{\alpha j\sigma}, c_{\alpha' j' \sigma'}^\dagger\} = \delta_{\alpha\alpha'} \delta_{jj'} \delta_{\sigma\sigma'} \quad (2.5.11)$$

$$\{c_{\alpha j\sigma}, c_{\alpha' j' \sigma'}\} = \{c_{\alpha j\sigma}^\dagger, c_{\alpha' j' \sigma'}^\dagger\} = 0 \quad (2.5.12)$$

Two identical fermions are not allowed to occupy the same band in a single site due to Pauli exclusion principle. Therefore, the terms with two particles occupying the same state are eliminated from Eq.(2.5.5). However, the kinetic term that describes the particles tunneling from either different sites or different bands is not affected by the Pauli principle. With some transformations, one may easily arrive at the  $p$ -bands fermionic Hubbard model,

$$\begin{aligned} H_f = & -t \sum_{\alpha, j, \sigma} (c_{\alpha, j, \sigma}^\dagger c_{\alpha, j+1, \sigma} + c_{\alpha, j+1, \sigma}^\dagger c_{\alpha, j, \sigma}) - \lambda \sum_{\alpha, j, \sigma} c_{\alpha, j, \sigma}^\dagger c_{\bar{\alpha}, j, \sigma} \\ & + U \sum_{\alpha, j} n_{\alpha, j, \uparrow} n_{\alpha, j, \downarrow} + V \sum_{j, \sigma, \sigma'} n_{p_x, j, \sigma} n_{p_y, j, \sigma'} \\ & - 2J_H \sum_j \left[ \mathbf{S}_{p_x, j} \cdot \mathbf{S}_{p_y, j} + \frac{n_{p_x, j} n_{p_y, j}}{4} \right] \\ & + J_H \sum_j (c_{p_x, j, \uparrow}^\dagger c_{p_x, j, \downarrow}^\dagger c_{p_y, j, \downarrow} c_{p_y, j, \uparrow} + c_{p_y, j, \uparrow}^\dagger c_{p_y, j, \downarrow}^\dagger c_{p_x, j, \downarrow} c_{p_x, j, \uparrow}) \end{aligned} \quad (2.5.13)$$

where we introduce the notations  $\sigma = \uparrow$  or  $\downarrow$  for spin-up and spin-down fermions. The  $n_{\alpha, j, \uparrow}$  and  $n_{\alpha, j, \downarrow}$  refer to spin-up and spin-down density operators for a fermion on  $p_x$  or  $p_y$  band of  $j$  site. The spin operators  $\mathbf{S}_j$  and the total density  $n_j$  on single site are given by,

$$S_j^z = \sum_{\alpha} S_{\alpha j}^z = \frac{1}{2} \sum_{\alpha} (c_{\alpha, j, \uparrow}^\dagger c_{\alpha, j, \uparrow} - c_{\alpha, j, \downarrow}^\dagger c_{\alpha, j, \downarrow}) \quad (2.5.14)$$

$$S_j^+ = \sum_{\alpha} S_{\alpha j}^+ = \sum_{\alpha} c_{\alpha, j, \uparrow}^\dagger c_{\alpha, j, \downarrow} \quad (2.5.15)$$

$$\mathbf{S}_j = \sum_{\alpha} \mathbf{S}_{\alpha, j} = \frac{1}{2} \sum_{\alpha, \sigma, \sigma'} c_{\alpha, j, \sigma}^\dagger \boldsymbol{\sigma} c_{\alpha, j, \sigma'} \quad (2.5.16)$$

$$n_j = \sum_{\alpha} n_{\alpha j} = \sum_{\alpha} (c_{\alpha, j, \uparrow}^\dagger c_{\alpha, j, \uparrow} + c_{\alpha, j, \downarrow}^\dagger c_{\alpha, j, \downarrow}) \quad (2.5.17)$$

where  $\boldsymbol{\sigma}$  denotes the Pauli matrices. We will use the Hamiltonian Eq.(2.5.13) in our discussion of chapter 4.

## (b) Bosonic Hubbard model

Bosons obey the commutation relations, which are

$$\left[ b_{\alpha j \sigma}, b_{\alpha' j' \sigma'}^\dagger \right] = \delta_{\alpha \alpha'} \delta_{j j'} \delta_{\sigma \sigma'} \quad (2.5.18)$$

$$\left[ b_{\alpha j \sigma}, b_{\alpha' j' \sigma'} \right] = \left[ b_{\alpha j \sigma}^\dagger, b_{\alpha' j' \sigma'}^\dagger \right] = 0 \quad (2.5.19)$$

where  $b_{\alpha j \sigma}^\dagger$  ( $b_{\alpha j \sigma}$ ) are bosonic operators. After some transformations, we may obtain the two components  $p$ -band bosonic Hubbard model,

$$\begin{aligned} H_b = & -t \sum_{\alpha, j, \sigma} (b_{\alpha, j, \sigma}^\dagger b_{\alpha, j+1, \sigma} + b_{\alpha, j+1, \sigma}^\dagger b_{\alpha, j, \sigma}) - \lambda \sum_{\alpha, j, \sigma} b_{\alpha, j, \sigma}^\dagger b_{\bar{\alpha}, j, \sigma} \\ & + \frac{U}{2} \sum_{\alpha, j, \sigma, \sigma'} b_{\alpha, j, \sigma}^\dagger b_{\alpha, j, \sigma'}^\dagger b_{\alpha, j, \sigma'} b_{\alpha, j, \sigma} + V \sum_{j, \sigma, \sigma'} b_{p_x, j, \sigma}^\dagger b_{p_y, j, \sigma'}^\dagger b_{p_y, j, \sigma'} b_{p_x, j, \sigma} \\ & + 2J_H \sum_j \left[ \mathbf{S}_{p_x, j} \cdot \mathbf{S}_{p_y, j} + \frac{n_{p_x, j} n_{p_y, j}}{4} \right] \\ & + J_H \sum_j (b_{p_x, j, \uparrow}^\dagger b_{p_x, j, \downarrow}^\dagger b_{p_y, j, \downarrow} b_{p_y, j, \uparrow} + b_{p_y, j, \uparrow}^\dagger b_{p_y, j, \downarrow}^\dagger b_{p_x, j, \downarrow} b_{p_x, j, \uparrow}) \\ & + \frac{J_H}{2} \sum_{j, \sigma} (b_{p_x, j, \sigma}^\dagger b_{p_x, j, \sigma}^\dagger b_{p_y, j, \sigma} b_{p_y, j, \sigma} + b_{p_y, j, \sigma}^\dagger b_{p_y, j, \sigma}^\dagger b_{p_x, j, \sigma} b_{p_x, j, \sigma}) \end{aligned} \quad (2.5.20)$$

The notations and the definitions of the spin operators  $\mathbf{S}_j$  and the total density  $n_j$  on single site are the same as that for fermions. One can easily arrive at the single band fermionic (or bosonic) Hubbard model by omitting the band index  $\alpha$  or spinless  $p$ -bands fermionic (or bosonic) Hubbard model by omitting the spin index  $\sigma$ , respectively. We will employ the Hamiltonian Eq.(2.5.20) in our discussion of chapter 5.

## 2.6 Perturbation theory

In most cases, there are no exact solutions for strongly-correlated many-body systems. However, perturbation theory of an exactly solvable model may shed some light on the properties of systems of interest. In the following, we illustrate the use of perturbation theory for a case particularly relevant for this thesis, namely an  $N$ -component  $SU(N)$  (Fermi- or Bose-) Hubbard model with a strong on-site repulsion at  $1/N$  filling [3]. The results discussed below will be used directly for our analysis of  $p$ -bands systems within this thesis (chapters 4, 5, and 6).

The SU(N) Hubbard model for a single band has the form:

$$\begin{aligned} H &= H_K + H_U \\ &= -t \sum_{\langle ij \rangle} (c_{i,\sigma}^\dagger c_{j,\sigma} + c_{j,\sigma}^\dagger c_{i,\sigma}) + \frac{U}{2} \sum_i n_i(n_i - 1) \end{aligned} \quad (2.6.1)$$

where  $\langle ij \rangle$  denotes nearest neighbours,  $n_i = \sum_\sigma c_{i,\sigma}^\dagger c_{i,\sigma}$ ,  $\sigma = -S, \dots, S$  and  $N = 2S + 1$ . For tunneling  $t = 0$ , the ground state is exactly known, with one particle in each site and an energy  $E_0 = 0$ . Then we may add a perturbing tunneling term (with  $t \ll U$ ). It is convenient to introduce a projector operator to make sure that there is only particle per site,

$$P = \prod_i \left( \sum_{\sigma=-S}^S |\sigma\rangle_i \langle \sigma|_i \right) \quad (2.6.2)$$

where  $|\sigma\rangle_i = c_{i,\sigma}^\dagger |0\rangle_i$ , and  $|0\rangle$  is the vacuum state. If the particles are spin 1/2 fermions, the projector operator could be simply written as  $P = \prod_i (1 - n_{i,\uparrow} n_{i,\downarrow})$ . Then we need to find an effective Hamiltonian with one-particle-per-site eigenstates  $P|\psi\rangle$ . We introduce  $Q = 1 - P$  (where  $P^2 = P$ ,  $Q^2 = Q$ ,  $QP = PQ = 0$  hold). Hence:

$$H|\psi\rangle = E|\psi\rangle \quad (2.6.3)$$

$$H(P + Q)|\psi\rangle = E(P + Q)|\psi\rangle \quad (2.6.4)$$

We want to eliminate  $Q|\psi\rangle$ . Multiplying  $Q$  from the left and using  $Q^2 = Q$  to replace one  $Q$  in the left side, we get

$$QH(P + Q^2)|\psi\rangle = QE(P + Q)|\psi\rangle \quad (2.6.5)$$

$$(QHQ - E)Q|\psi\rangle = -QHP|\psi\rangle \quad (2.6.6)$$

Putting  $Q|\psi\rangle = -(QHQ - E)^{-1}QHP|\psi\rangle$  into Eq.(2.6.4), we may arrive at

$$(H - H(QHQ - E)^{-1}QH)P|\psi\rangle = E(P + Q)|\psi\rangle \quad (2.6.7)$$

Multiplying  $P$  from left side and use  $P + Q = 1, P^2 = P, PQ = 0$ , we get

$$(PHP - PH(P + Q)(QHQ - E)^{-1}QHP)P|\psi\rangle = EP|\psi\rangle \quad (2.6.8)$$



From Eq.(2.6.1), we may obtain the following relations,

$$PHP = PH_K P = PH_U P = PH_U Q = QH_U P = 0 \quad (2.6.9)$$

$$PHQ = PH_K Q, QHP = QH_K P \quad (2.6.10)$$

Using these relation, Eq.(2.6.8) becomes,

$$-PH_K Q(QHQ - E)^{-1}QH_K PP|\psi\rangle = EP|\psi\rangle \quad (2.6.11)$$

For any state  $|\psi\rangle$ , after the projector  $P$  or  $P^2$ , there is just one particle per site. Then, after the operator  $H_K$ , there will be one particle hopping from one site to another. So there would be just one hole and one double occupation state left after the operator  $QH_K P|\psi\rangle$ . For small tunneling  $t$ , we may just replace  $QHQ = U$  and  $E = 0$  up to zero order of  $t$ , since  $PHQ$  and  $QHP$  are in second order of  $t$ . By replacing  $QHQ = U, E = 0$  and inserting  $PH_K P = 0, Q^2 = Q, P + Q = 1$  we may arrive at the effective model,

$$H_{eff} = -\frac{(PH_K Q)(QH_K P)}{U} = -\frac{PH_K(P + Q)H_K P}{U} = -P\frac{H_K^2}{U}P \quad (2.6.12)$$

Let us give the form of the  $H_{eff}$ . From Eq.(2.6.12), one knows that if there is one particle hopping from site  $j$  to site  $i$ , there must be one particle hopping back, otherwise  $H_{eff}$  would be zero. Thus, From Eq.(2.6.1), we obtain,

$$\begin{aligned} PH_K^2 P &= t^2 \sum_{\langle ij \rangle, \sigma, \sigma'} P [c_{i,\sigma}^\dagger c_{j,\sigma} c_{j,\sigma'}^\dagger c_{i,\sigma'} + c_{j,\sigma}^\dagger c_{i,\sigma} c_{i,\sigma'}^\dagger c_{j,\sigma'}] P \\ &= 2t^2 \sum_{\langle ij \rangle, \sigma, \sigma'} P c_{i,\sigma}^\dagger c_{j,\sigma} c_{j,\sigma'}^\dagger c_{i,\sigma'} P \\ &= 2t^2 \sum_{\langle ij \rangle, \sigma, \sigma'} P c_{i,\sigma}^\dagger (\delta_{\sigma,\sigma'} \pm c_{j,\sigma'}^\dagger c_{j,\sigma}) c_{i,\sigma'} P \end{aligned} \quad (2.6.13)$$

with  $+$  for bosons,  $-$  for fermions. If one-particle-per-site constraint  $\sum_\sigma c_{i,\sigma}^\dagger c_{i,\sigma} = 1$  is used, one may remove the projector operator  $P$ . Then we obtain the effective model with the form

$$H_{eff} = \sum_{\langle ij \rangle} \frac{2t^2}{U} (-1 \pm P_{ij}) \quad (2.6.14)$$

where  $+$  for fermions,  $-$  for bosons, and the permutation operator is

$$P_{ij} = \sum_{\sigma, \sigma'} c_{i, \sigma}^\dagger c_{j, \sigma'}^\dagger c_{j, \sigma} c_{i, \sigma'} \quad (2.6.15)$$

For spin 1/2 fermions or bosons, we may obtain  $P_{ij} = 2\mathbf{S}_i \mathbf{S}_j + \frac{1}{2}$  by defining the spin operator  $\mathbf{S}_i = \frac{1}{2} \sum_{\sigma, \sigma'} c_{i, \sigma}^\dagger \boldsymbol{\sigma} c_{i, \sigma'}$  and using  $\boldsymbol{\sigma}_{\alpha, \beta} \cdot \boldsymbol{\sigma}_{\alpha', \beta'} = 2\delta_{\alpha, \beta'} \delta_{\alpha', \beta} - \delta_{\alpha, \beta} \delta_{\alpha', \beta'}$ . So we may get the usual Heisenberg type effective model

$$H_{eff} = \begin{cases} \frac{4t^2}{U} \sum_{\langle ij \rangle} (\mathbf{S}_i \mathbf{S}_j - \frac{1}{4}), & \text{for spin 1/2 fermions} \\ \frac{4t^2}{U} \sum_{\langle ij \rangle} (-\mathbf{S}_i \mathbf{S}_j - \frac{3}{4}), & \text{for spin 1/2 bosons} \end{cases} \quad (2.6.16)$$

Up to this point we have assumed that a spin-independent scattering length. If the scattering length depends on the total spin saying  $S^T$  of the two colliding particles, one needs to define the projector operator on the subspace of the total spin  $S^T$  to be

$$P_{ij}(S^T) = \sum_{M=-S^T}^{S^T} |S^T, M\rangle_{ij} \langle S^T, M|_{ij} \quad (2.6.17)$$

with the completeness relation

$$\sum_{S^T=0}^{2S} P_{ij}(S^T) = 1 \quad (2.6.18)$$

Inserting Eq.(2.6.18) into Eq.(2.6.11), we get

$$-PH_K Q(QHQ - E)^{-1}QH_K P \sum_{S^T=0}^{2S} P_{ij}(S^T) P|\psi\rangle = EP|\psi\rangle \quad (2.6.19)$$

One can then obtain the effective model:

$$\begin{aligned} H_{eff} &= \sum_{\langle ij \rangle} \sum_{S^T=0}^{2S} \frac{2t^2}{U_{S^T}} (-1 \pm P_{ij}) P_{i,j}(S^T) \\ &= \sum_{\langle ij \rangle} \sum_{S^T=0}^{2S} \frac{2t^2}{U_{S^T}} (-1 \pm (-1)^{S^T+2S}) P_{i,j}(S^T) \end{aligned} \quad (2.6.20)$$

where the permutation operator  $P_{ij}$  is given by the summation of the projector operators  $P_{i,j}(S^T)$  in the form  $P_{ij} = \sum_{S^T=0}^{2S} (-1)^{S^T+2S} P_{i,j}(S^T)$ , and the relation  $P_{i,j}(S_1^T) P_{i,j}(S_2^T) = \delta_{S_1^T, S_2^T} P_{i,j}(S_1^T)$  has been employed.

Let us obtain the projector operator  $P_{i,j}(S^T)$  in terms of the spin operator  $\mathbf{S}_i$  and  $\mathbf{S}_j$ . Since  $2\mathbf{S}_i\mathbf{S}_j = (\mathbf{S}_i + \mathbf{S}_j)^2 - \mathbf{S}_i^2 - \mathbf{S}_j^2$  and  $(\mathbf{S}^T)^2|S^T\rangle = (\mathbf{S}_i + \mathbf{S}_j)^2|S^T\rangle = S^T(S^T + 1)|S^T\rangle$ , we have the following eigenequation,

$$\mathbf{S}_i\mathbf{S}_j|S^T\rangle = \frac{1}{2} (S^T(S^T + 1) - 2S(S + 1)) |S^T\rangle \quad (2.6.21)$$

Therefore we may obtain the  $2\mathbf{S}_i\mathbf{S}_j$  in terms of the projector operator  $P_{i,j}(S^T)$

$$\mathbf{S}_i\mathbf{S}_j = \sum_{S^T=0}^{2S} \frac{1}{2} (S^T(S^T + 1) - 2S(S + 1)) P_{i,j}(S^T) \quad (2.6.22)$$

For spin 1/2 fermions or bosons, we may easily have the expression of  $\mathbf{S}_i\mathbf{S}_j$  for singlet and triplet states  $|S^T = 0\rangle$  and  $|S^T = 1\rangle$ ,

$$\mathbf{S}_i\mathbf{S}_j = -\frac{3}{4}P_{i,j}(S^T = 0) + \frac{1}{4}P_{i,j}(S^T = 1) \quad (2.6.23)$$

Squaring the Eq.(2.6.23) and using  $(\mathbf{S}_i\mathbf{S}_j)^2 = \frac{3}{16} - \frac{1}{2}\mathbf{S}_i\mathbf{S}_j$ , and  $P_{i,j}^2(S^T = 0) = P_{i,j}(S^T = 0)$ ,  $P_{i,j}^2(S^T = 1) = P_{i,j}(S^T = 1)$ ,  $P_{i,j}(S^T = 0)P_{i,j}(S^T = 1) = 0$ , one may derive the expression of projector operator  $P_{i,j}(S^T)$  for singlet and triplet states  $|S^T = 0\rangle$  and  $|S^T = 1\rangle$ ,

$$P_{i,j}(S^T = 0) = -\mathbf{S}_i\mathbf{S}_j + \frac{1}{4} \quad (2.6.24)$$

$$P_{i,j}(S^T = 1) = \mathbf{S}_i\mathbf{S}_j + \frac{3}{4} \quad (2.6.25)$$

Putting these into Eq.(2.6.20), one could derive the effective Heisenberg model for spin 1/2 fermions or bosons,

$$H_{eff} = \begin{cases} -\frac{4t^2}{U_0}P_{i,j}(S^T = 0) = \frac{4t^2}{U_0} \sum_{\langle ij \rangle} (\mathbf{S}_i\mathbf{S}_i - \frac{1}{4}), & \text{for spin 1/2 fermions} \\ -\frac{4t^2}{U_1}P_{i,j}(S^T = 1) = \frac{4t^2}{U_1} \sum_{\langle ij \rangle} (-\mathbf{S}_i\mathbf{S}_i - \frac{3}{4}), & \text{for spin 1/2 bosons} \end{cases} \quad (2.6.26)$$

It is clear that fermions prefer to form singlet states, whereas bosons prefer to form triplet states. We will come back to effective spin models in our discussion of chapters 4, 5, and 6.

## 2.7 Fidelity and fidelity susceptibility

In the bulk of this thesis we present ground state phase diagrams for spin-orbit models that we have studied. We have used different detection schemes for studying phase transitions between various phases. There is an important observable, developed initially in quantum information theory, for the numerical study of quantum phase transitions in 1D many-body systems, namely the so-called fidelity and fidelity susceptibility (FS). In this section, we present and discuss this method, which we have employed throughout this thesis.

Given any Hamiltonian  $H(\lambda) = H_0 + \lambda H_I$ , with the eigenstates  $|\Psi_n(\lambda)\rangle$ , ground states wave function  $|\Psi_0(\lambda + \delta\lambda)\rangle$  under a small change  $\delta\lambda$  may be written as

$$|\Psi_0(\lambda + \delta\lambda)\rangle = |\Psi_0(\lambda)\rangle + \delta\lambda \sum_{n \neq 0} \frac{\langle \Psi_n(\lambda) | H_I | \Psi_0(\lambda) \rangle}{E_0(\lambda) - E_n(\lambda)} |\Psi_n(\lambda)\rangle \quad (2.7.1)$$

up to first order in perturbation theory. If one wants to know the (Hilbert space) 'distance' between  $|\Psi_0(\lambda)\rangle$  and  $|\Psi_0(\lambda + \delta\lambda)\rangle$ , one may compute their overlap,

$$F = \langle \Psi_0(\lambda) | \Psi_0(\lambda + \delta\lambda) \rangle \quad (2.7.2)$$

The absolute value norm  $|F|$  is called fidelity [39–42], a concept from quantum information, which measures the information loss after the change of the parameter  $\lambda$ . Let us expand  $F$  in Taylor series up to second order,

$$F = 1 + \delta\lambda \langle \Psi_0(\lambda) | \frac{\partial}{\partial \lambda} \Psi_0(\lambda) \rangle + \frac{(\delta\lambda)^2}{2} \langle \Psi_0(\lambda) | \frac{\partial^2}{\partial \lambda^2} \Psi_0(\lambda) \rangle \quad (2.7.3)$$

Squaring the norm of the fidelity  $|F|^2$  and using the identities  $\frac{\partial}{\partial \lambda} \langle \Psi_0(\lambda) | \Psi_0(\lambda) \rangle = 0$  and  $\frac{\partial^2}{\partial \lambda^2} \langle \Psi_0(\lambda) | \Psi_0(\lambda) \rangle = 0$ , one arrives at the following expression of fidelity in terms of fidelity susceptibility [41, 42]

$$|F| = 1 - \frac{(\delta\lambda)^2}{2} \chi_F \quad (2.7.4)$$

Therefore the fidelity susceptibility in terms of the fidelity  $|F|$  is

$$\chi_F = \frac{2(1 - |F|)}{(\delta\lambda)^2} = \lim_{\delta\lambda \rightarrow 0} \frac{-2 \ln |F|}{\delta\lambda^2} \quad (2.7.5)$$

This expression can be used for numerical calculations. The fidelity susceptibility in terms of the wave function is also known,

$$\chi_F = \left\langle \frac{\partial}{\partial \lambda} \Psi_0(\lambda) \middle| \frac{\partial}{\partial \lambda} \Psi_0(\lambda) \right\rangle - \left\langle \frac{\partial}{\partial \lambda} \Psi_0(\lambda) \middle| \Psi_0(\lambda) \right\rangle \left\langle \Psi_0(\lambda) \middle| \frac{\partial}{\partial \lambda} \Psi_0(\lambda) \right\rangle \quad (2.7.6)$$

$$= \sum_{n \neq 0} \frac{|\langle \Psi_n(\lambda) | H_I | \Psi_0(\lambda) \rangle|^2}{(E_n(\lambda) - E_0(\lambda))^2} \quad (2.7.7)$$

FS is widely used as an unbiased indicator of quantum phase transitions, especially in one-dimensional systems where a very accurate numerical calculation of the ground state wave function is possible thanks to the well-developed DMRG technique.

FS shows a scaling behavior near the quantum critical point  $\lambda = \lambda_c$  characterized by the correlation length  $\xi \sim |\lambda - \lambda_c|^{-\nu} = \delta\lambda^{-\nu}$  for  $L = \infty$ . Indeed,  $F(\lambda, \delta\lambda)$  is dimensionless and  $\chi_F = (1 - F^2)/\delta\lambda^2$ , hence,

$$\chi_F(\lambda \simeq \lambda_c) \sim \delta\lambda^{-2} f(L/\xi) \sim \delta\lambda^{-2} f(L\delta\lambda^\nu)$$

$f(L\delta\lambda^\nu) \rightarrow \tilde{f}(L^{1/\nu}\delta\lambda)$  requiring that  $\chi_F$  remains finite for a finite system when  $\delta\lambda \rightarrow 0$  (no singularities for finite system),  $\tilde{f}(L^{1/\nu}\delta\lambda) \sim (L^{1/\nu}\delta\lambda)^2 \rightarrow$ :

$$\chi_F(\lambda_c) \sim L^{2/\nu} \sim L^{2d+2z-2\Delta_V}, \quad (2.7.8)$$

where  $\Delta_V$  is the scaling dimension of the driving operator coupled to  $\lambda$  at the critical point  $\lambda_c$  and  $z$  is the dynamic exponent. Only  $d = 1$  and  $z = 1$  cases are studied in this thesis. Hence FS per site diverges at  $L \rightarrow \infty$  as  $\chi_L = \chi_F/L \propto L^{1+2z-2\Delta_V}$ , as long as  $\Delta_V < z + 1/2$ . In chapter 7 we analyze in detail the peculiar behavior of the FS at a Berezinskii-Kosterlitz-Thouless transition.



# Chapter 3

## Numerical methods

In this chapter we discuss the numerical methods employed in this thesis, including exact diagonalization, density matrix renormalization group, time-evolving block decimation, and time-dependent density matrix renormalization group.

### 3.1 Exact diagonalization

In many-body strongly correlated systems, there are limited exact analytical solutions due to the complexity of many-body states. However, one may exactly solve small systems by means of the so-called exact diagonalization (ED). Exact diagonalization may be applied in one-dimensional, two-dimensional and three-dimensional systems. Note that ED is a somewhat ambiguous term, since it is sometimes understood as full ED (finding all eigenstates and eigenvalues in full Hilbert space) and other times as the Lanczos algorithm (finding only few lowest lying eigenstates and eigenvalues in a sparse sub-space). Hereafter we employ ED meaning full ED, considering separately the Lanczos algorithm. In the following, we discuss the ED and Lanczos algorithm in details (see Ref. [43] for more information).

#### (a) Exact diagonalization

Let us start with the time independent Schrödinger equation

$$\hat{H}|\Psi\rangle = E|\Psi\rangle \quad (3.1.1)$$

Given any orthonormal  $\{\langle n|m\rangle = \delta_{nm}\}$  and complete  $\{\sum_{n=1}^M |n\rangle\langle n| = 1\}$  basis  $\{|n\rangle\}$  in

the  $M$ -dimensional Hilbert space, the Hamiltonian  $\hat{H}$  and the wave function  $|\Psi\rangle$  can be written as  $\hat{H} = \sum_{m,n=1}^M H_{mn}|m\rangle\langle n|$  and  $|\Psi\rangle = \sum_{n=1}^M \psi_n|n\rangle$ , where  $H_{mn} = \langle m|\hat{H}|n\rangle$  are Hamiltonian elements and the coefficients  $\psi_n = \langle n|\Psi\rangle$  are complex numbers. Putting  $\hat{H}$  and  $|\Psi\rangle$  into Eq.(3.1.1), we arrive at the matrix representation of the Schrödinger equation  $\sum_{n=1}^M H_{mn}\psi_n = E\psi_m$ , which is,

$$\begin{pmatrix} H_{11} & H_{12} & \cdots & H_{1M} \\ H_{21} & H_{22} & \cdots & H_{2M} \\ \vdots & \vdots & \ddots & \vdots \\ H_{M1} & H_{M2} & \cdots & H_{MM} \end{pmatrix} \begin{pmatrix} \psi_1 \\ \psi_2 \\ \vdots \\ \psi_M \end{pmatrix} = E \begin{pmatrix} \psi_1 \\ \psi_2 \\ \vdots \\ \psi_M \end{pmatrix} \quad (3.1.2)$$

This matrix may be exactly diagonalized numerically. Thus one can get all the eigenstates  $\psi^n = [\psi_1^n, \psi_2^n, \psi_3^n, \dots, \psi_M^n]^T$  and all the energy  $E_n$ , and therefore in principle know all the information (i.e. ground states properties, all the excitations, correlation functions, finite temperature and dynamic properties) of the system. However the computational cost is proportional to  $M^3$  and memory for storage is proportional to  $M^2$ , which limits ED to  $L = 12 - 14$  spin-1/2 particles because of the huge matrix dimension  $M = 2^L$  of the Hilbert space.

Usually, for realistic physical systems, the Hamiltonian matrix is sparse due to the symmetries of the system. Thus, one just needs to store the non-zeros matrix elements by implementing the symmetries, which allows for handling up to  $L = 20 - 24$  spin 1/2 particles. Many symmetries (such as, magnetization conservation, particle number conservation, momentum conservation, reflection symmetry ...) may be employed. If the symmetries are implemented, the Hamiltonian becomes block diagonal as shown in Fig.3.1 by grouping together the elements labeled by the same quantum number. For example, the matrix dimension for the Heisenberg model with conserved magnetization is  $M_b = N!/(N_\uparrow N_\downarrow)$ . Then one may diagonalize each block separately, both reducing the memory and increasing the speed of performance. In the following, we take the conservation of magnetization of spin 1/2 Heisenberg type models (i.e. SU(2) symmetric Heisenberg model  $H = \mathbf{S}_i \cdot \mathbf{S}_{i+1}$ ) as an example to show how to implement the symmetry for the exact diagonalization.

There is a quicker but very inefficient way to implement the magnetization con-



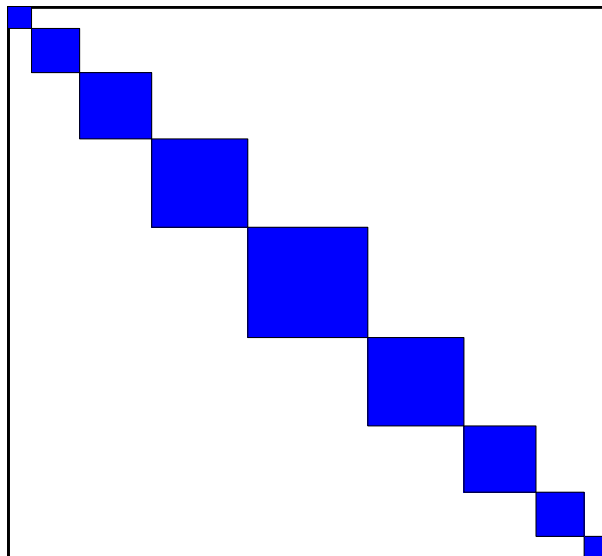


Figure 3.1: The Hamiltonian matrix is divided into blocks characterized by conserved quantum numbers. This structure represents 4-sites spin 1/2 Heisenberg model with conservation of magnetization, which is divided into 9 blocks with  $(S^z)^T = \sum_i S_i^z = -4, -3, -2, -1, 0, 1, 2, 3, 4$

conservation symmetry. Since the projector for  $(S^z)^T = \sum_i S_i^z = M_z$  is given by

$$P(M_z) = \frac{1}{(N/2 + M_z)!(N/2 - M_z)!} \prod_{j=-N/2, j \neq M_z}^{N/2} [(S^z)^T - j] \quad (3.1.3)$$

one may project the Hamiltonian into the  $M_z$  sector by standard matrix manipulation,

$$H(M_z) = P^\dagger(M_z) H P(M_z). \quad (3.1.4)$$

Now the Hamiltonian is a sparse matrix with all non-zeros elements only lying in the Hilbert space of  $M_z$  sector. Thus, one may obtain the block matrix for the  $M_z$  sector by only saving the non-zeros elements and diagonalize them. One just needs to build the Hamiltonian matrix and projector matrix with Kronecker. However, much memory is needed to build the matrix (with dimension  $M = 2^L$ ) and the projector.

We show at this point how to implement magnetization conservation efficiently. The idea is to find the block Hamiltonian without saving the full Hilbert space.

Since there is just two states for a single spin (spin up and spin down), we may use bits of integers ("1" refer to spin down  $\uparrow$  and "0" refer to spin up  $\downarrow$ ) as the complete basis of physical states. We can save the states very easily by changing from binary to decimal base. For a  $L$  sites base "2" state with coefficients  $(c_L, c_{L-1}, \dots, c_2, c_1)$ , one may convert very quickly to base "10" number  $N$  (and vice versa)

$$N = c_L \cdot 2^{L-1} + c_{L-1} \cdot 2^{L-2} + \dots + c_2 \cdot 2^1 + c_1 \cdot 2^0 \quad (3.1.5)$$

For example, given a 4-sites state  $|\downarrow\uparrow\uparrow\downarrow\rangle = |0110\rangle = 0 \cdot 2^3 + 1 \cdot 2^2 + 1 \cdot 2^1 + 0 \cdot 2^0 = 6$ . The diagonal part  $S_i^z S_{i+1}^z$  does not change the state. The non-diagonal part  $\frac{1}{2}(S_i^+ S_{i+1}^- + S_i^- S_{i+1}^+)$  flips spins, changing the state. For example,  $(S_3^+ S_4^- + S_3^- S_4^+) |\downarrow\uparrow\uparrow\downarrow\rangle = |\uparrow\downarrow\uparrow\downarrow\rangle = |1010\rangle = 10$ . Then one can build the Hamiltonian in the following steps to perform the exact diagonalization algorithm:

(1). Do a loop in the full Hilbert space  $M = 2^L$  to search all the bit states with a given magnetization, storing the corresponding numbers in base "10". The sector will have in total  $N_s$  states.

(2). Find the non-zero elements of block matrix with matrix dimension  $M = N_s^2$ . From the  $S_i^z S_{i+1}^z$  terms, the element of the block Hamiltonian are either  $H(n, n) = 1/4$  if the nearest neighbouring spins are the same or  $H(n, n) = -1/4$  if the nearest neighbouring spins are opposite, with  $n = 1, \dots, N_s$ . For the non-diagonal part  $\frac{1}{2}(S_i^+ S_{i+1}^- + S_i^- S_{i+1}^+)$ , one should firstly find the base "10" integer number  $m$  of the new bit state after the manipulation of the non-diagonal Hamiltonian term. Then the elements of the block Hamiltonian is  $H(n, m) = 1/2$ .

(3). Use a numerical library like Lapack/Arpack [44] to find the eigenstates and eigenvalues, where the cost is proportional to  $N_s^3$ , and then compute the corresponding order parameters we are interested in.

### (b) Lanczos algorithm

However, if one is just interested in the ground state or few excited states, one may use the Lanczos algorithm, which is an iterative method to find the ground and excited states. By it, one now may reach up to  $L = 42$  sites for spin 1/2 Heisenberg model with one symmetry or combination of many symmetries. Lanczos algorithm is an advanced powerful method for finding the eigenstates and eigenvalues. One just

needs to repeat the manipulation  $|\phi_N\rangle = H^N|\phi_0\rangle$  (main cost in Lanczos algorithm) where  $|\phi_0\rangle$  is any random initial state. In principle, when  $N = N_s$ , the result becomes exact. However, when  $N$  becomes very large but still much smaller than  $N_s$ , one may get a very good approximation of eigenstates.

In Lanczos algorithm, the speed is improved because the cost for matrix vector computation is just proportional to  $N_s^2$ . Indeed, one does not need to save all the elements of the block Hamiltonian matrix with matrix memory  $M = N_s^2$ . Since the matrix is sparse, we just need to save the non-zero elements, by which the memory is only proportional to  $LN_s$ . Here we do not show how to write the Lanczos algorithm itself as a tridiagonal matrix manually. One simply implements the operation  $|\phi_{m+1}\rangle = H|\phi_m\rangle$ , and use Lanczos algorithm based on the Lapack/Arpack library. From the properties of a complete orthogonal basis, we have,

$$|\phi_{m+1}\rangle = H|\phi_m\rangle = \sum_{\alpha=1}^{N_s} \sum_{\beta=1}^{N_s} \langle\beta|H|\alpha\rangle \phi_m(\alpha)|\beta\rangle \quad (3.1.6)$$

$$= \sum_{\alpha=1}^{N_s} \sum_{\beta=1}^{N_s} \sum_{j=1}^L \langle\beta|\mathbf{S}_j\mathbf{S}_{j+1}|\alpha\rangle \phi_m(\alpha)|\beta\rangle \quad (3.1.7)$$

If  $\mathbf{S}_j\mathbf{S}_{j+1}|\alpha\rangle = h_\alpha^j|\gamma\rangle$ , the only non-zeros Hamiltonian elements are  $|\beta\rangle = |\gamma\rangle$  due to the orthogonal property of the basis  $\langle\beta|\gamma\rangle = \delta_{\beta,\gamma}$ . Then one may reduce the computing cost and the memory by only dealing with the non-zero elements of the block Hamiltonian, which is proportional to  $LN_s$  by the following formula,

$$|\phi_{m+1}\rangle = \sum_{\alpha=1}^{N_s} \sum_{j=1}^L h_\alpha^j \phi_m(\alpha)|\gamma\rangle \quad (3.1.8)$$

Now we can write the Lanczos algorithm in a similar three steps as full exact diagonalization does and just modify the step (2). Instead of saving all the elements of the block Hamiltonian, we just repeat the operation

$$\phi_{m+1}(\gamma) = \sum_{\alpha=1}^{N_s} \sum_{j=1}^L h_\alpha^j \phi_m(\alpha) \quad (3.1.9)$$

Note that now the cost and memory is just proportional to  $LN_s$ .

## 3.2 Matrix product states

Density matrix renormalization group is a very powerful numerical method for low dimensional strongly correlated systems [7,8]. The key idea is to truncate the Hilbert space according to the eigenvalues of the density matrix during the renormalization step instead of using the lowest-lying eigenstates in Wilson's renormalization group for Kondo problem [6]. Matrix product states (MPS) ansatz is particularly useful when dealing with the dynamics of many-body systems [46–49]. Now it is very convenient to study the time evolution of the many body systems thanks to the ansatz of matrix product states [50–54]. In the following, we show how to implement the DMRG and the time evolution based on MPS.

### 3.2.1 Density matrix renormalization group

#### (a) Conventional DMRG

The conventional DMRG was written in terms of superblock  $B^S \bullet \bullet B^R$  (including the system block  $B^S$ , the environment block  $B^R$ , and two sites  $\bullet \bullet$  in between these two blocks) based on real space renormalization group language [7,8,45]. The infinite (and finite) density matrix renormalization group algorithm are explained in Fig.3.2. One could start from two-sites (or four sites) to form superblocks  $B_1^S \bullet \bullet B_1^R$  for the Hamiltonian and then use Lanczos algorithm or Davidson algorithm to diagonalize superblock to find the ground state  $E_0^1$  and the corresponding eigenstate  $|\psi\rangle = \sum_{ij} \psi_{ij} |i\rangle |j\rangle$ . Now one may build the reduced density operator  $\rho_S = \text{Tr}_B(|\psi\rangle\langle\psi|)$ , with reduced density matrix  $\rho_{ij} = \sum_j \psi_{ij} \psi_{i'j}^*$  to project on the system block together with one site  $B_1^S \bullet$  to obtain the new truncated (if needed) blocks  $B_2^S$  and  $B_2^R$ . Next add two sites in the center of the two blocks to form new superblocks  $B_2^S \bullet \bullet B_2^R$ . One may repeat the above steps until the ground state converges. This is the algorithm for infinite-site DMRG. For finite-site DMRG algorithm with size  $L$ , one just needs to do infinite DMRG algorithm up to size  $L$ , then do sweeps from left to right and from right to left until the ground state converges.

#### (b) DMRG in terms of the MPS

It is very convenient to write the DMRG algorithm in terms of MPS. Before

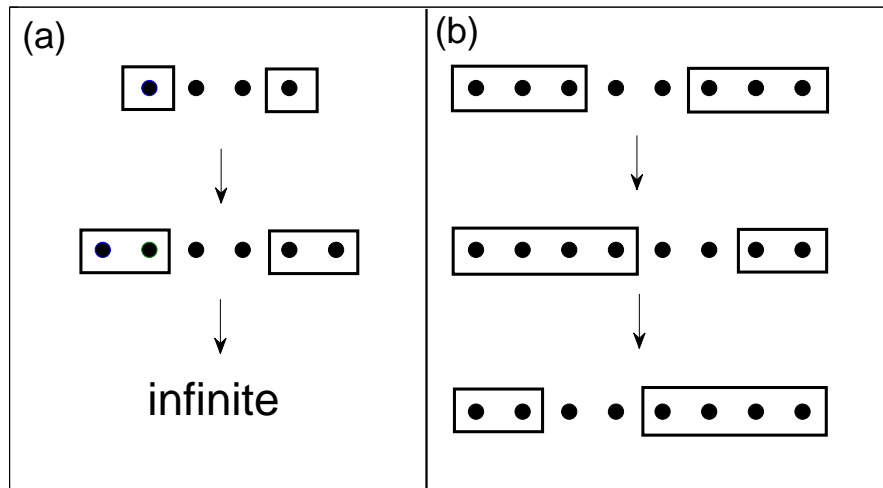


Figure 3.2: (a).The infinite site DMRG algorithm: starting from 4 sites, then repeat the DMRG algorithm mentioned in the main text until the ground state converges. (b).The finite site DMRG algorithm: when using infinite DMRG up to size  $L$ , sweep from left to right to the last site, then sweep from right to left to the first site. Repeat left-right sweeps until the ground state converges.

introducing the DMRG algorithm based on MPS, we introduce the graphical representation shown in Fig.3.3 of vectors, matrices and the contraction rules between them. We denote a vector by a vertex with one leg at the right side, a matrix by a vertex with legs at both sides, and a tensor by a vertex with more than two legs. A connected leg means the product contraction of two matrices or the summation in that connected index between two tensors. Now let us consider a system with  $L$  sites with full Hilbert space  $d^L$ , where  $d$  is the dimension of the local space  $\{\sigma_i\}$ , and  $i = 1, \dots, L$ . Any state  $|\psi\rangle$  could be written in this complete local basis as

$$|\psi\rangle = \sum_{\sigma_1, \sigma_2, \dots, \sigma_L} c_{\sigma_1 \sigma_2 \dots \sigma_L} |\sigma_1\rangle \otimes |\sigma_2\rangle \otimes \dots \otimes |\sigma_L\rangle \quad (3.2.1)$$

It is impossible to diagonalize the huge number of coefficients  $c_{\sigma_1 \sigma_2 \dots \sigma_L}$  with dimension  $d^L$ . Therefore one needs to find an effective reduced Hilbert space of the system. The simplest state, called MPS, can be constructed by using the singular

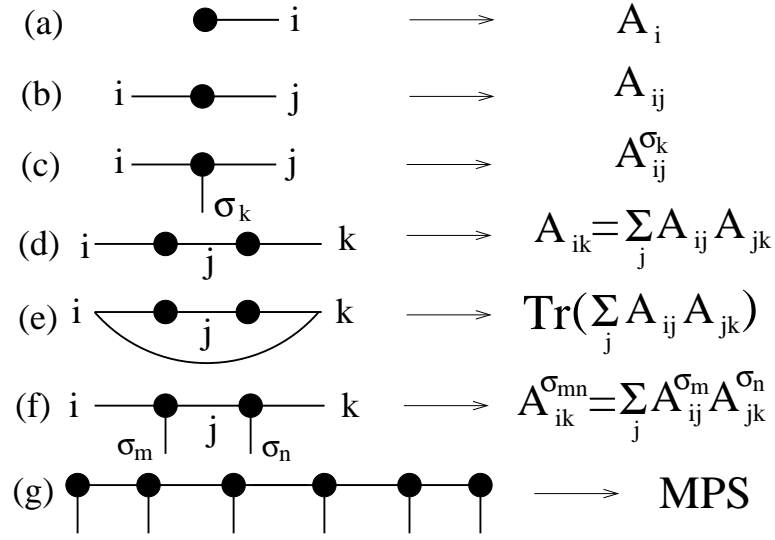


Figure 3.3: Graphical representation of the vectors, matrices and the contraction rules between them. (a). Vector  $A_i$ , (b). Matrix  $A_{ij}$ , (c). Matrix  $A_{ij}^{\sigma_k}$  (trial tensor) with additional local physical dimension  $\sigma_k$ , (d). Contraction of two matrices  $A_{ij}$  and  $A_{jk}$ , the result is a matrix  $A_{ik}$ , (e). Trace of the matrix  $A_{ik}$ , (f). Contraction of two matrices  $A_{ij}^{\sigma_m}, A_{jk}^{\sigma_n}$ , (g). MPS with system size  $L = 6$ .

value decomposition (SVD) of the general coefficients  $c_{\sigma_1 \sigma_2 \dots \sigma_L}$ , which is,

$$|\psi\rangle = \sum_{\sigma_1, \sigma_2, \dots, \sigma_L} \sum_{i_1 i_2, \dots, i_{L-1}} A_{i_1}^{\sigma_1} A_{i_1 i_2}^{\sigma_2} \dots A_{i_{L-2} i_{L-1}}^{\sigma_{L-1}} A_{i_{L-1}}^{\sigma_L} |\sigma_1\rangle \otimes |\sigma_2\rangle \otimes \dots \otimes |\sigma_L\rangle \quad (3.2.2)$$

$$= \sum_{\sigma_1, \sigma_2, \dots, \sigma_L} A^{\sigma_1} A^{\sigma_2} \dots A^{\sigma_{L-1}} A^{\sigma_L} |\sigma_1\rangle \otimes |\sigma_2\rangle \otimes \dots \otimes |\sigma_L\rangle \quad (3.2.3)$$

The second term in Eq.(3.2.3) is the compact form of Eq.(3.2.2). Now the coefficients are the MPS, which can be represented in the Fig.3.3(g) in the graphical notation.

The energy for this arbitrary state is

$$E = \frac{\langle \psi | H | \psi \rangle}{\langle \psi | \psi \rangle} \quad (3.2.4)$$

By using the derivation  $\frac{\partial E}{\partial \langle \psi |} = 0$  for the global minimization, it is easy to find the eigenvalue equation  $H|\psi\rangle = E|\psi\rangle$  of the system. However it is difficult to solve this general eigenvalue equation due to the exponential parameters in the number of full Hilbert space. Therefore, we need to minimize locally few matrices (i.e one or two matrices) each time. Two sites  $k$  and  $k + 1$  with coefficients  $A^{\sigma_k}, A^{\sigma_{k+1}}$  are

optimized at each time. By using the minimization principle

$$\frac{\partial E}{\partial(A^{\sigma_k^*} A^{\sigma_{k+1}^*})} = 0 \quad (3.2.5)$$

we may arrive at a generalized eigenvalue equation in terms of the effective Hamiltonian and the effective norm

$$H_{eff}^k A^{\sigma_k} A^{\sigma_{k+1}} = E N_{eff}^k A^{\sigma_k} A^{\sigma_{k+1}} \quad (3.2.6)$$

where the  $H_{eff}^k$  and  $N_{eff}^k$  are the effective Hamiltonian and the effective norm of the wave function of the superblock. The effective superblock Hamiltonian  $H_{eff}^k$  should include the left block  $H_L^k$ , the right block  $H_R^k$ , two single sites  $H_{\bullet}^k$ ,  $H_{\bullet}^{k+1}$ , and the corresponding pairing terms  $H_{L\bullet}^k$ ,  $H_{\bullet R}^k$ ,  $H_{\bullet\bullet}^k$ . So the effective  $H_{eff}^k$  and  $N_{eff}^k$  can be written as,

$$\begin{aligned} H_{eff}^k &= (H_L^k)_{l,l} \otimes \mathbb{1}_{d,d} \otimes \mathbb{1}_{d,d} \otimes \mathbb{1}_{r,r} + \mathbb{1}_{l,l} \otimes \mathbb{1}_{d,d} \otimes \mathbb{1}_{d,d} \otimes (H_R^k)_{r,r} \\ &\quad + \mathbb{1}_{l,l} \otimes (H_{\bullet}^k)_{d,d} \otimes \mathbb{1}_{d,d} \otimes \mathbb{1}_{r,r} + \mathbb{1}_{l,l} \otimes \mathbb{1}_{d,d} \otimes (H_{\bullet}^{k+1})_{d,d} \otimes \mathbb{1}_{r,r} \\ &\quad + (H_{L\bullet}^k)_{l-d,l-d} \otimes \mathbb{1}_{d,d} \otimes \mathbb{1}_{r,r} + \mathbb{1}_{l,l} \otimes \mathbb{1}_{d,d} \otimes (H_{\bullet R}^k)_{d-r,d-r} \\ &\quad + \mathbb{1}_{l,l} \otimes (H_{\bullet\bullet}^k)_{d^2,d^2} \otimes \mathbb{1}_{r,r} \end{aligned} \quad (3.2.7)$$

$$N_{eff}^k = (N_L^k)_{l,l} \otimes \mathbb{1}_{d,d} \otimes \mathbb{1}_{d,d} \otimes \mathbb{1}_{r,r} + \mathbb{1}_{l,l} \otimes \mathbb{1}_{d,d} \otimes \mathbb{1}_{d,d} \otimes (N_R^k)_{r,r} \quad (3.2.8)$$

where  $\mathbb{1}$  is the identity matrix and  $l, d, r$  are the dimensions of the matrices.  $N_L^k$  and  $N_R^k$  are the norms of the left block and the right block, respectively. If the MPS are both left-normalized

$$N_L^k = \sum_{\sigma_{i < k}} A^{\sigma_i \dagger} A^{\sigma_i} = 1 \quad (3.2.9)$$

and right-normalized

$$N_R^k = \sum_{\sigma_{i > k+1}} A^{\sigma_i} A^{\sigma_i \dagger} = 1 \quad (3.2.10)$$

the generalized eigenvalue equation Eq.(3.2.6) becomes the standard eigenvalue equation,

$$H_{eff}^k A^{\sigma_k} A^{\sigma_{k+1}} = E A^{\sigma_k} A^{\sigma_{k+1}} \quad (3.2.11)$$

Now the effective Hamiltonian  $H_L^k, H_{L\bullet}^k, H_R^k, H_{\bullet R}^k$  and the density matrices  $\rho_L$  and  $\rho_R$  for left and right part in the site  $k$  and site  $k + 1$  become very simple,

$$H_L^k = \sum_{i=1}^{k-2} (A^{\sigma_i} A^{\sigma_{i+1}})^\dagger h_i^{lr} A^{\sigma_i} A^{\sigma_{i+1}} + \sum_{i=1}^{k-1} A^{\sigma_i \dagger} h_i^s A^{\sigma_i} \quad (3.2.12)$$

$$H_{L\bullet}^k = A^{\sigma_{k-1} \dagger} h_{k-1}^l A^{\sigma_{k-1}} \quad (3.2.13)$$

$$H_R^k = \sum_{i=k+2}^{L-1} (A^{\sigma_i} A^{\sigma_{i+1}})^\dagger h_i^{lr} A^{\sigma_i} A^{\sigma_{i+1}} + \sum_{i=k+2}^L A^{\sigma_i \dagger} h_i^s A^{\sigma_i} \quad (3.2.14)$$

$$H_{\bullet R}^k = A^{\sigma_{k+2}} h_{k+1}^r A^{\sigma_{k+2} \dagger} \quad (3.2.15)$$

$$\rho_L = (A^{\sigma_k} A^{\sigma_{k+1}})^\dagger A^{\sigma_k} A^{\sigma_{k+1}} \quad (3.2.16)$$

$$\rho_R = A^{\sigma_k} A^{\sigma_{k+1}} (A^{\sigma_k} A^{\sigma_{k+1}})^\dagger \quad (3.2.17)$$

where the general Hamiltonian  $H = \sum_i h_{i,i+1} = \sum_i (h_i^l \otimes h_i^r + h_i^s) = \sum_i (h_i^{lr} + h_i^s)$  is used. The other terms  $H_{\bullet}^k = h_k^s$ ,  $H_{\bullet}^{k+1} = h_{k+1}^s$  and  $H_{\bullet\bullet}^k = h_i^{lr}$  are the original terms.

Obviously, there are no  $H_L^1, H_{L\bullet}^1, H_R^{L-1}, H_{\bullet R}^{L-1}$  terms, which can be set to zero. One could solve the eigenvalue problem Eq.(3.2.11) with Lanczos or Davidson algorithm to obtain the eigenvalues and the eigenstates. However, it would cost too much if we build the effective Hamiltonian directly. If we keep the maximal  $M$  states in the block Hamiltonian, both the dimension of the effective Hamiltonian and the cost for the manipulation of  $H_{eff}^k$  and  $A^{\sigma_k} A^{\sigma_{k+1}}$  are  $(Md)^4$ , which is too large for the calculation. In practice, one may perform the manipulation between the seven terms of the effective Hamiltonian  $H_{eff}^k$  in Eq.(3.2.7) and  $A^{\sigma_k} A^{\sigma_{k+1}}$  separately. The cost will be proportional to  $M^3$  instead of  $M^4$ . See Fig.3.4 for the graphical representation of the manipulation of  $H_{eff}^k$  and  $A^{\sigma_k} A^{\sigma_{k+1}}$ . After finding the eigenvalues  $E$  and the eigenstates  $A^k A^{k+1}$ , we need to move one site for the next local minimization, for instance, moving from sites  $k, k + 1$  to  $k + 1, k + 2$ . We need to truncate the Hilbert space if needed and update the block Hamiltonian  $H_L^k$  and  $H_R^k$  for the next minimization step. To truncate the Hilbert space, we may use the eigenvalue decomposition of the density matrix  $\rho_L$  ( $\rho_R$ ) or the SVD of the wave function  $A^k A^{k+1}$  for moving one site from left to the right side (right moving) or from right to the left side (left moving). For instance, if the SVD of  $A^k A^{k+1}$  is

$$A^k A^{k+1} = USV^\dagger \quad (3.2.18)$$



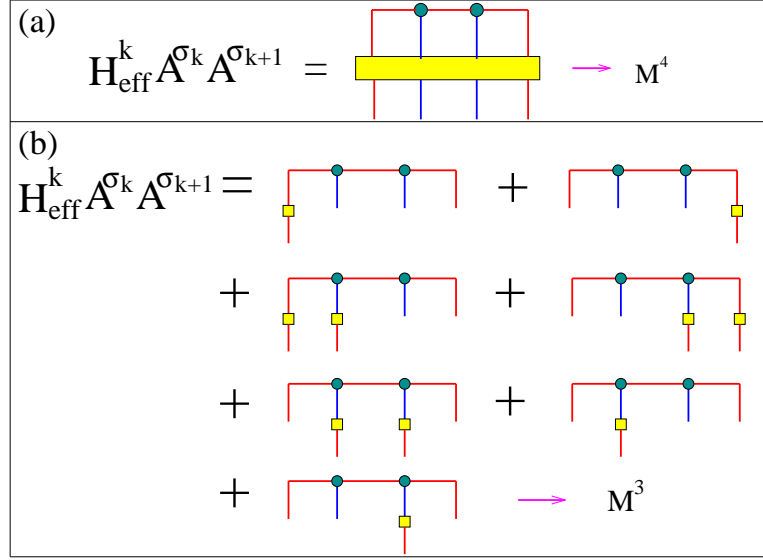


Figure 3.4: Graphical representation of the manipulation of  $H_{\text{eff}}^k$  and  $A^{\sigma_k} A^{\sigma_{k+1}}$ . (a). the direct manipulation of  $H_{\text{eff}}^k$  and  $A^{\sigma_k} A^{\sigma_{k+1}}$ , the cost is  $\propto M^4$  (b). Multiply the  $H_{\text{eff}}^k$  and  $A^{\sigma_k} A^{\sigma_{k+1}}$  term by term separately, the cost is  $\propto M^3$ . The circle vertex with legs are the  $A^{\sigma_k}, A^{\sigma_{k+1}}$ , the square symbols with legs are the Hamiltonian. The dimension for truncation (red legs) and local degree (blue legs) are  $M$  and  $d$ .

the updated matrix for right moving is

$$A^k = U \quad (3.2.19)$$

the updated matrix for left moving is

$$A^{k+1} = V^\dagger \quad (3.2.20)$$

To optimize the matrix for the next two sites, the new block Hamiltonian  $H_L^k$  and  $H_R^k$  need to be updated using the new updated matrix  $A^{\sigma_k}$  or  $A^{\sigma_{k+1}}$ . The following iterations hold for  $H_L^{k+1}$  and  $H_{L\bullet}^k$  (for right moving  $k \rightarrow k+1$ ), or  $H_R^{k-1}$  and  $H_{\bullet R}^{k-1}$  (for left moving  $k \rightarrow k-1$ ) (see Fig.3.5 for the graphical representation of updating  $H_L^{k+1}$  and  $H_{\bullet R}^{k-1}$ ),

$$H_L^{k+1} = A^{\sigma_k \dagger} (H_L^k + H_{L\bullet}^k h_{k-1}^r + H_{\bullet}^k) A^{\sigma_k} \quad (3.2.21)$$

$$H_{L\bullet}^{k+1} = A^{\sigma_k \dagger} h_k^l A^{\sigma_k} \quad (3.2.22)$$

$$H_R^{k-1} = A^{\sigma_{k+1}} (H_R^k + h_{k+1}^l H_{\bullet R}^k + H_{\bullet}^{k+1}) A^{\sigma_{k+1} \dagger} \quad (3.2.23)$$

$$H_{\bullet R}^{k-1} = A^{\sigma_{k+1}} h_k^r A^{\sigma_{k+1} \dagger} \quad (3.2.24)$$

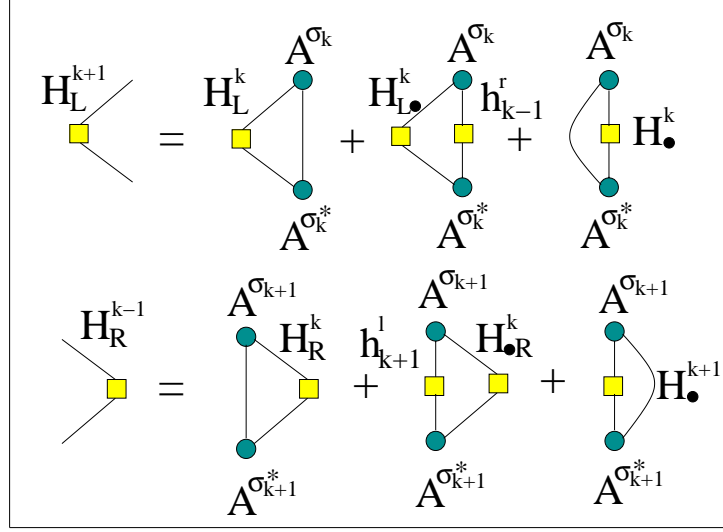


Figure 3.5: Graphical representation of updating the left block  $H_L^{k+1}$  and right block  $H_R^{k-1}$ . The circles denote the matrix  $A^{\sigma_k}$  and the conjugate  $A^{\sigma_k^*}$ , the yellow squares denote the Hamiltonian  $H_L^k$ ,  $H_{L\bullet}^k$ ,  $H_{\bullet}^k$ ,  $H_R^k$ ,  $H_{\bullet R}^k$ ,  $h_k^l$ ,  $h_k^r$ .

Then we can repeat the local minimization steps for several sweeps until the energy converges. Note that it is possible to guess the wave function when we shift one site, making the code faster and the algorithm more robust. From SVD of Eq.(3.2.18), we can find that if we update  $A^k = U$  for right moving or update  $A^{k+1} = V^\dagger$  for left moving, there should be  $SV^\dagger$  or  $US$  left. Hence, we can obtain the wave function prediction  $W_R$  for right moving,  $W_L$  for left moving in the following form

$$W_R = SV^\dagger A^{k+2} \quad (3.2.25)$$

$$W_L = A^{k-1}US \quad (3.2.26)$$

The DMRG algorithm may be summarized as follows:

(1). Initial states: Start from a random initial state or from the result of an infinite DMRG. Make the orthonormalization from site  $L$  to the first site by SVD. Set  $H_L^1 = H_{L\bullet}^1 = H_R^{L-1} = H_{\bullet R}^{L-1} = 0$ . Compute and save  $H_R^k$  and  $H_{\bullet R}^k$  for  $1 \leq k \leq L-2$  according to Eq.(3.2.14) and Eq.(3.2.15).

(2). Left to right sweep ( $1 \rightarrow L-2$ ): Optimize site 1 and site 2 according to Eq.(3.2.11). Do SVD (truncate the Hilbert space and keep maximal  $M$  states if the number of states is larger than  $M$ ). Update  $A^1$  according to Eq.(3.2.19). Update

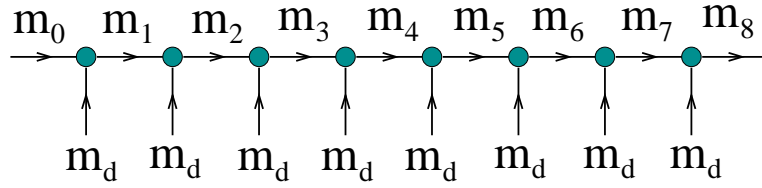


Figure 3.6: Graphical representation of implementing symmetries for 8 sites chain as an example. We set  $m_0 = 0$ ,  $m_8 = M_s$  for first link and last link, where  $M_s$  is the symmetric sector we want to compute and right arrows denote the increasing direction of quantum numbers. The quantum numbers for two neighbouring bonds hold the relation  $m_{i+1} = m_i + m_d$ , where  $m_d$  is the quantum numbers of local degrees, the  $m_i$  are the quantum number in the bonds.

$H_L^2$  according to Eq.(3.2.21) and  $H_{L\bullet}^2$  according to Eq.(3.2.22). Make wave function prediction using Eq.(3.2.25). Iterate all above steps until reaching the L-2 site by moving one site from left to right.

(3). Right to left sweep ( $L - 1 \rightarrow 2$ ): Optimize site  $L - 1$  and site  $L$  according to Eq.(3.2.11). Do SVD (truncate the Hilbert space and keep maximal  $M$  states if the number of states is larger than  $M$ ). Update  $A^L$  according to Eq.(3.2.20). Update  $H_R^{L-2}$  according to Eq.(3.2.23) and  $H_{R\bullet}^{L-2}$  according to Eq.(3.2.24). Make wave function prediction using Eq.(3.2.26). Iterate all above steps until the site 2 is reached by moving one site from right to left.

(4). Repeat (2) and (3) for several sweeps until the energy or other quantities converge. Stop the code and calculate the observables using MPS.

### (c) DMRG with symmetries

Symmetries play a crucial role in a DMRG implementation. In absence of symmetries, one can keep just several hundred states, however, with symmetries it is possible to reach several thousand states by saving only non-zero blocks as we did for exact diagonalization, and thus reduce the memory and speed up the code. It is easy to implement U(1) symmetries like particle number conservation and magnetization conservation. For a chain of  $L$  sites, there are  $L + 1$  directed auxiliary bonds with all possible quantum numbers  $m_i$  and  $L$  directed physical bonds with all possible quantum numbers  $m_d$  characterizing the local degree of freedom (see

Fig.3.6). The rule is that the quantum numbers of the ingoing lines must equal the quantum numbers of the outgoing lines for each site, thus the quantum numbers for two neighbouring bonds hold the relation [49, 55, 56]

$$m_{i+1} = m_i + m_d \quad (3.2.27)$$

Since there is only one element for the first and the last auxiliary bonds, and the quantum numbers increase from left to right, we may set the quantum number  $m_0 = \{0\}$  and  $m_L = \{M_s\}$  for the first and the last bond, where  $M_s$  denotes the maximal quantum number. For example,  $m_d = \{0, 1\}$  for spin-1/2 Heisenberg model, and hence  $m_1 = \{0, 1\}$ ,  $m_2 = \{0, 1, 2\}$ ,  $m_3 = \{0, 1, 2, 3\}$ , and so on. If the sector  $(S^z)^T = 0$  is calculated,  $M_s = L/2$ . For any matrix  $A^i$  with 3 links  $m_i, m_{i+1}, m_d$ , the non-zero elements must satisfy Eq.(3.2.27), hence the  $A^i$  is block diagonal. Let us use double numbers to denote the possible quantum numbers and the corresponding non-zero numbers. For instance,  $m_d = \{0^1, 1^1\}$  denotes that the possible quantum numbers are 0 and 1 and the corresponding non-zero numbers are 1 for both of them. Then the quantum numbers for auxiliary links are  $m_0 = \{0^1\}$ ,  $m_1 = \{0^1, 1^1\}$ ,  $m_2 = \{0^1, 1^2, 2^1\}$ ,  $m_3 = \{0^1, 1^3, 2^3, 3^1\}$ , and so on. Note that when the Hamiltonian operates on the matrix, the quantum number may change. Let us consider the general conservation operator  $Q = \sum_i Q_i$  commuting with Hamiltonian  $[Q, H] = 0$ . If the operator  $Q$  fulfills

$$[Q, B_i] = \Delta q B_i \quad (3.2.28)$$

for a given operator  $B_i$ , the quantum numbers of the blocks with non-zero elements will shift  $\Delta q$  [57]. For instance, if we consider the particle number conservation  $N^T = \sum_i N_i$  or magnetization conservation  $(S^z)^T = \sum_i S_i^z$ , the quantum numbers of the blocks with non-zero matrix elements will increase one ( $\Delta q = 1$ ) (or decrease one ( $\Delta q = -1$ )) when the operator  $c_i^\dagger, S_i^+$  (or  $c_i, S_i^-$ ) acts on matrix  $A^i$ .

### 3.2.2 Time evolution

#### (a) Time-Evolving Block Decimation Algorithm

Time-evolving block decimation (TEBD) algorithm is a powerful method to simulate both the ground state and the time evolution, based on the  $\Gamma\lambda$  notation (see

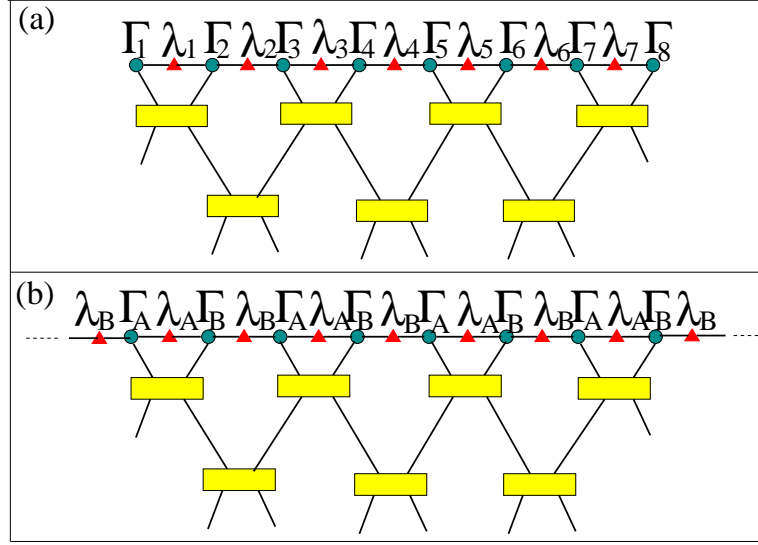


Figure 3.7: Graphical representation of TEBD and iTEBD in  $\Gamma\lambda$  notation. (a). TEBD for 8-sites, (b) iTEBD with AB translation invariance. Circles and triangles denote  $\Gamma$  and  $\lambda$ , the yellow gates denote the evolution operator  $U_{i,i+1} = e^{-ih_{i,i+1}\delta t}$  for real time or  $U_{i,i+1} = e^{-h_{i,i+1}\delta\tau}$  for imaginary time.

below) of the MPS [50–52]. A similar idea as TEBD was developed for DMRG based on MPS [53,54]. It is easy to obtain the  $\Gamma\lambda$  form of the MPS from Eq.(3.2.3) directly. First we normalize the MPS form right to the left (right normalization). Then we do the SVD with Eq.(3.2.18) for matrix  $A^{\sigma_1} = U_1 S_1 V_1^\dagger$  and denote  $\Gamma_1 = U_1$  and  $\lambda_1 = S_1$ . Then we move the  $S_1 V_1^\dagger$  to the right and do the SVD for  $S_1 V_1^\dagger A^{\sigma_2} = U_2 S_2 V_2^\dagger$ , and denote  $\Gamma_2 = (S_1)^{-1} U_2$  and  $\lambda_2 = S_2$ . Repeating these steps till the end, one gets the  $\Gamma\lambda$  form of the MPS (see Fig.3.7 for graphical representation of the TEBD and infinite TEBD).

$$|\psi\rangle = \sum_{\sigma_1, \sigma_2, \dots, \sigma_L} \Gamma_1^{\sigma_1} \lambda_1 \Gamma_2^{\sigma_2} \lambda_2 \cdots \Gamma_{L-1}^{\sigma_{L-1}} \lambda_{L-1} \Gamma_L^{\sigma_L} |\sigma_1\rangle \otimes |\sigma_2\rangle \otimes \cdots \otimes |\sigma_L\rangle \quad (3.2.1)$$

It is easy to check that the MPS with the above  $\Gamma\lambda$  notation are both left-normalized and right-normalized (that is called canonical) for any  $\lambda_i$  because we derive it using the SVD. Given any state  $|\Psi_0\rangle$ , we can do the imaginary time evolution

$$|\Psi_{gr}\rangle = \lim_{\tau \rightarrow \infty} \frac{\exp(-H\tau)|\Psi_0\rangle}{\|\exp(-H\tau)|\Psi_0\rangle\|} \quad (3.2.2)$$

to find the ground state, or do the real evolution

$$|\Psi_t\rangle = \exp(-iHt)|\Psi_0\rangle \quad (3.2.3)$$

to study the dynamics. As shown before, it is impossible to simulate the time evolution with total  $H$  directly due to the huge Hilbert space. However, it is possible to perform a local evolution by means of Trotter decomposition. Trotter decomposition for the evolution operator  $U_t = e^{-iHt} = (e^{-iH\delta t})^{t/\delta t}$  up to the second order is

$$e^{-iH\delta t} = \prod_{\text{odd } i} e^{-ih_{i,i+1}\delta t/2} \prod_{\text{even } i} e^{-ih_{i,i+1}\delta t} \prod_{\text{odd } i} e^{-ih_{i,i+1}\delta t/2} + O(\delta t^3) \quad (3.2.4)$$

Because the MPS in  $\Gamma\lambda$  notation is canonical, one can locally update the matrix product states by the local evolution operator  $U_{i,i+1} = e^{-ih_{i,i+1}\delta t}$ . (see Fig.(3.7) for the graphical representation of updating the matrix product states by the local operator  $U_{i,i+1}$ ).

The local matrix  $\Gamma_i, \lambda_i, \Gamma_{i+1}$  are updated in the following steps:

- (1). Apply the local evolution operator  $U_{i,i+1}$  to the matrices  $\lambda_{i-1}, \Gamma_i, \lambda_i, \Gamma_{i+1}, \lambda_{i+1}$  in sites  $i, i+1$ , to obtain the single tensor  $\Theta = \lambda_{i-1}\Gamma_i\lambda_iU_{i,i+1}\Gamma_{i+1}\lambda_{i+1}$ .
- (2). Do singular value decomposition for  $\Theta = USV^\dagger$
- (3). Update  $\Gamma_i, \lambda_i, \Gamma_{i+1}$  by putting  $\Gamma_i = (\lambda_{i-1})^{-1}U, \lambda_i = S, \Gamma_{i+1} = V^{-1}(\lambda_{i+1})^{-1}$ .

To do the real time evolution by TEBD, one just needs to repeat above locally updated steps for the whole chain for  $t/\delta t$  times. To find the ground state using the real imaginary evolution by TEBD, one needs to make sure that the energy converges and one can also decrease  $\delta\tau$  to reduce the Trotter errors. Note that for infinite-site TEBD, one just needs to do the local update for the bulk of the system for some periodicity (i.e. periodic two AB sub-lattice in Fig.3.7(b)). The rest is the same as for finite TEBD.

### (b) Time-dependent DMRG

Time evolution may be simulated using DMRG based on MPS. As we discussed before, for both DMRG and TEBD, for the local matrix update we may start from the right-normalized or from the left-normalized MPS. Choosing the right-normalized ones, the time-dependent DMRG may be performed as follows:

(1). Odd-sites evolution: First, we apply the local evolution operator  $U_{1,2}$  to the sites 1 and 2, do SVD as in TEBD, and update  $A^{\sigma_1} = U$ . Now we need to note that the next local update is still for the odd sites, which is site 3 and site 4. Therefore we need to make sure the left part of site 3 and site 4 is left-normalized in order to perform the correct simulation. In the TEBD algorithm, the  $\Gamma\lambda$  notation is canonical. The left-normalized and right-normalized condition are satisfied automatically. However, in time-dependent DMRG, there are not. Hence, we need to do left-normalization using SVD to shift one site from site 2 to site 3. Then we can do the local update for site 3 and 4 as we did before. Then we repeat these to the end of chain.

(2). Even-sites evolution: Update the matrix similarly as we did for odd sites and perform the right-normalization.

Note that there is a simple way to implement the time evolution with the DMRG algorithm. Instead of using Trotter decomposition to divide the system into odd-sites and even-sites, one may perform the local evolution by usual left to right sweeps and reverse all the local evolution from right to left

$$e^{-iH\delta t} = e^{-ih_{1,2}\delta t} e^{-ih_{2,3}\delta t} \dots e^{-ih_{2,3}\delta t} e^{-ih_{1,2}\delta t} + O(\delta t^3) \quad (3.2.5)$$

The errors of decomposition is the same order  $O(\delta t^3)$  too. Now we just need to replace the effective Hamiltonian  $H_{eff}^i$  in the Lanczos step Eq.(3.2.11) by the time evolution operator  $U_{i,i+1}$  to update the new wave function and keep others the same. Therefore, it is particularly simple to implement a time-dependent DMRG if one already has developed a DMRG code.





# Chapter 4

## Spin-orbital models of dipolar fermions in zig-zag optical lattices

### 4.1 Introduction

Orbital degrees of freedom of electrons play an important role in novel phases observed in transition-metal oxides with partially filled  $d$  levels [58, 59]. In Mott insulators, they may enhance thermal as well as quantum fluctuations [38] and lead to spin-orbital liquid states [60–63], and to spontaneously dimerized states without any long-range magnetic order [64, 65]. In many solid-state systems, the orbital dynamics is often quenched due to the coupling of the orbitals to Jahn-Teller phonons, and the study of the quantum nature of orbitals demands systems with strong superexchange coupling between spins and orbitals. However, in real materials, the coupling strengths are fixed by nature, being very difficult to modify, thus limiting the experimental access to a potentially vast phase diagram.

Ultracold spinor gases in optical lattices open fascinating perspectives for the analysis of the quantum nature of orbitals [66–68]. The coupling constants in these systems can be easily controlled by modifying the lattice parameters and/or by means of Feshbach resonances [69]. As shown in chapter 2, various lattice geometries, including frustrated ones, like triangular [70] and Kagomé [71], may be created by combining different counter-propagating laser beams and superlattice techniques. In addition, not only the physics in the lowest band but also that in higher bands

may be controllably studied [19]. Moreover, recent experiments on chromium [72], dysprosium [73], atomic gases, and polar molecules [74] are unveiling the exciting physics of ultracold dipolar gases, for which the dipole-dipole interactions may lead to exotic phases [75, 76].

In this chapter, we show that dipolar spinor Fermi gases in appropriate zig-zag lattice geometries allow for the quantum simulation of spin-orbital models for a family of Mott insulating compounds, including systems with weak [64, 77, 78] as well as pronounced [79] relativistic spin-orbit couplings. Moreover, these models, which are relevant for real materials, as pyroxene titanium and layered vanadium oxides, may be explored with dipolar Fermi gases in parameter regimes which are hardly accessible for solid-state compounds, allowing for the observation of novel quantum phases.

In this chapter, we show as well that the ground-state diagram contains a spin-orbital liquid phase with a finite magnetization. This phase has a spontaneously broken  $SU(2)$  spin symmetry and algebraically decaying longitudinal spin correlations, while the orbital correlations decay exponentially. This behavior is interesting, since in one dimension (1D) spontaneous breaking of continuous symmetry is usually forbidden, with the only known exception being ferromagnets and ferrimagnets, where the magnetization of the ground state is locked at a certain value fixed by the Lieb-Schulz-Mattis theorem [80]. The mechanism driving the transition into this phase is given by the softening of composite excitations formed by bound states of spin waves and orbital domain walls. In addition, for open boundary conditions we observe peculiar boundary phase transitions that involve the formation of edge spins that decouple from the bulk and become nonlocally entangled. We support our analytical arguments by numerical results obtained by means of the DMRG technique introduced in chapter 3.

## 4.2 Spin-orbital model for fermions

We consider two-component (pseudo-spin-1/2) dipolar fermions loaded in doubly degenerate  $p$ -bands of a quasi-1D zig-zag lattice (see Fig.4.1). The system is

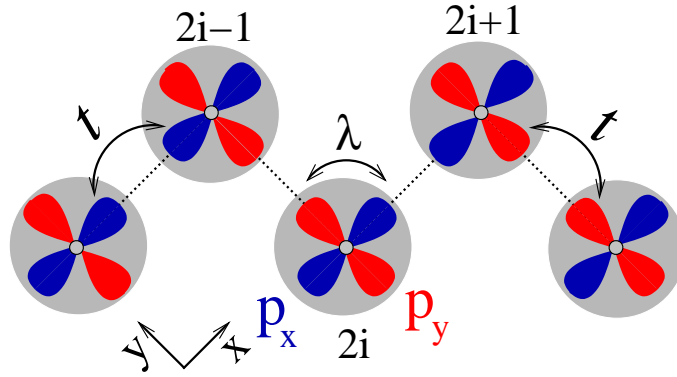


Figure 4.1: Geometry of the orbitally degenerate zig-zag lattice with nearest neighbour intersite hopping  $t$  (between similar orbitals) and onsite hopping between the orthogonal orbitals  $\lambda$ .

described by the Hubbard-type Hamiltonian Eq.(2.5.13) shown in chapter 2 with twofold orbital degeneracy. The energy scales that determine the system are the nearest neighbor (NN) hoppings  $t$  and the on-site repulsion energies  $U$  ( $V$ ) between the same (different) orbitals, the Hund coupling  $J_H$ , and an in-plane deformation of the optical lattice, distorting the XY rotational symmetry of a single-site potential that mixes the orbitals within the same site with an amplitude  $\lambda$ .

We derive in the following the effective spin-orbital model for models Eq.(2.5.13). For a two-orbital degenerate system, one may define the pseudo-orbital quantum number  $\sigma_i^z = +(-)1$ , with  $+1$  for the  $p_x$  orbital,  $-1$  for the  $p_y$  orbital. The corresponding quantum operators are given by the Pauli matrices,

$$\sigma_i^z = \sum_{\sigma} (c_{p_x,i,\sigma}^{\dagger} c_{p_x,i,\sigma} - c_{p_y,i,\sigma}^{\dagger} c_{p_y,i,\sigma}) \quad (4.2.1)$$

$$\sigma_i^x = \sum_{\sigma} (c_{p_x,i,\sigma}^{\dagger} c_{p_y,i,\sigma} + c_{p_y,i,\sigma}^{\dagger} c_{p_x,i,\sigma}) \quad (4.2.2)$$

We impose the condition of only one particle per site. Two possible processes will contribute to the effective Hamiltonian. Let us first consider two fermions at neighboring sites, and in the same orbital, i.e.  $|p_x\rangle_i \otimes |p_x\rangle_j$  or  $|p_y\rangle_i \otimes |p_y\rangle_j$ . If the fermions have opposite spin, the fermion in site  $j$  may hop into site  $i$ , forming doubly occupied states  $|p_x, p_x\rangle_i$  or  $|p_y, p_y\rangle_i$ . These two states are however not 2-particle eigenstates. Due to pair hopping these eigenstates are  $|p_x, p_x\rangle_i \pm |p_y, p_y\rangle_i$  with eigenen-

ergies  $U \pm J_H$ . Since the orbital part is symmetric, the spin part must be a singlet ( $S^T = 0$ ). Furthermore, because single particle in different sites can tunnel only from  $|p_x\rangle_j$  to  $|p_x\rangle_i$  or from  $|p_y\rangle_j$  to  $|p_y\rangle_i$  in neighbouring sites, the orbital parts of the effective model always select one orbital for each site as  $[1 + (-1)^i \sigma_i^z] [1 + (-1)^i \sigma_i^z]$ . Putting everything together, the effective Hamiltonian due to this first process is

$$H_{i,j}^{f1} = - \left[ \left( \frac{t^2}{U + J_H} + \frac{t^2}{U - J_H} \right) P_{i,j}(S^T = 0) \right] [1 + (-1)^i \sigma_i^z] [1 + (-1)^i \sigma_i^z] \quad (4.2.3)$$

Let us consider now a second process, in which particles at neighboring sites are located at different orbitals, i.e.  $|p_x\rangle_i \otimes |p_y\rangle_j$  or  $|p_y\rangle_i \otimes |p_x\rangle_j$ . When one particle hops from  $j$  to site  $i$ , the states  $|p_x, p_y\rangle_i$  or  $|p_y, p_x\rangle_i$  are formed. These states are again not eigenstates of two particles in a site, because of Hund-exchange interaction. The proper eigenstates are the symmetric and antisymmetric combinations,  $|p_x, p_y\rangle_i \pm |p_y, p_x\rangle_i$ . For the symmetric state, fermions should occupy a singlet spin state ( $S^T = 0$ ), with energy  $V + J_H$ , whereas for the antisymmetric orbital state, the fermions should be in a triplet spin state, with energy  $V - J_H$ . Since the two different orbitals are occupied respectively, the effective Hamiltonian for the orbital parts is  $\frac{1}{2}(1 - \sigma_i^z \sigma_{i+1}^z)$ . Putting all together, we derive the effective Hamiltonian for fermions in the second process,

$$H_{i,j}^{f2} = - \left[ \frac{t^2}{2(V + J_H)} P_{i,j}(S^T = 0) + \frac{t^2}{2(V - J_H)} P_{i,j}(S^T = 1) \right] (1 - \sigma_i^z) \quad (4.2.4)$$

Finally, a transfer between the orbitals at a given site is characterized by an effective transversal term:

$$H_{i,j}^\lambda = \lambda \sigma_i^x \quad (4.2.5)$$

Putting all contributions together, we obtain the effective spin-orbital models for fermions:

$$\begin{aligned} H_{eff}^f = & \sum_i \left[ 2\mathbf{S}_i \mathbf{S}_{i+1} + \alpha - \frac{1}{2} \right] [1 + (-1)^i \sigma_i^z] [1 + (-1)^i \sigma_{i+1}^z] \\ & - \Delta \sum_i 2\mathbf{S}_i \mathbf{S}_{i+1} [1 - \sigma_i^z \sigma_{i+1}^z] - \lambda \sum_i \sigma_i^x \end{aligned} \quad (4.2.6)$$

we use  $t^2/(2\tilde{U}) = 1$ , where  $\tilde{U} = (U^2 - J_H^2)/U$ ,  $\alpha = \tilde{U}(V + J_H/2)/(V^2 - J_H^2)$ , and  $\Delta = J_H\tilde{U}/(V^2 - J_H^2)$ .

In absence of Hund effect ( $J_H = 0$ ),  $\Delta = 0$  and  $\alpha = U/V$ . Even when  $J_H \neq 0$ ,  $\alpha \approx U/V$  since  $J_H \ll U(V)$ . The model at  $\alpha \simeq 1$ , describes the spin-orbital interplay in Mott insulating transition-metal compounds. At  $\lambda = 0$ , it describes a zig-zag chain of spin 1/2  $\text{Ti}^{3+}$  ions, with active  $d_{xy}$  and  $d_{yz}$  orbitals, in pyroxene titanium oxides  $\text{ATiSi}_2\text{O}_6$  ( $A = \text{Na, Li}$ ) [77, 78]. On the other hand, for  $\Delta = 0$  the Hamiltonian represents the one-dimensional (1D) counterpart of the two-dimensional (2D) model for  $\text{Sr}_2\text{VO}_4$  [79]. In the latter, the role of spins in Eq.(4.2.6) is played by an isospin variable discerning the Kramers partners, while the pseudo-orbital variables distinguish two lowest Kramers doublets of  $\text{V}^{4+}$  ion, and  $\lambda$  term in Eq.(4.2.6) represents relativistic spin-orbit coupling. Therefore we may consider the system in three regimes, no Hund effect regime ( $\Delta = 0$ ), relevant regime in solid state systems ( $\alpha \approx 1$ ), and the regime beyond solid state systems ( $\alpha \neq 1$ ). We analyze these regimes in detail in the following sections.

### 4.3 No Hund effect regime

We consider first the case without Hund effect,  $\Delta = 0$ . At  $\lambda = 0$  the orbitals are classical and the ground state may be easily obtained. For  $\alpha > 2$ , the orbital part presents antiferromagnetic (AF) order ( $\langle \sigma_i^z \rangle = \pm(1)^i$ ), whereas the spin part is completely degenerate (bold line in Fig.4.2). For  $\lambda \rightarrow 0$  a finite second-order spin exchange is generated,  $\sim \lambda^2 \sum_i \mathbf{S}_i \mathbf{S}_{i+1}$ . The spin sector behaves thus as an isotropic Heisenberg antiferromagnet (iH) and the infinite spin degeneracy is lifted. We denote this phase as (iH,AF), where the first term denotes iH spin phase and the second term AF orbital phase. We employ a similar notation for all phases below. A sketch of the (iH,AF) phases (and of other phases) may be found in Fig.4.2.

Higher order terms in  $\lambda/\alpha$  cannot break the  $\text{SU}(2)$  spin and translational symmetries, and thus for  $\lambda \rightarrow 0$  the iH phase in spin degrees is stable. As shown below, the iH is recovered for strong  $\lambda$  independently of the value of  $\alpha$ . Thus, we can expect that for  $\alpha > 2$  there is an unique iH phase in spin degrees of freedom for any  $\lambda \neq 0$ .

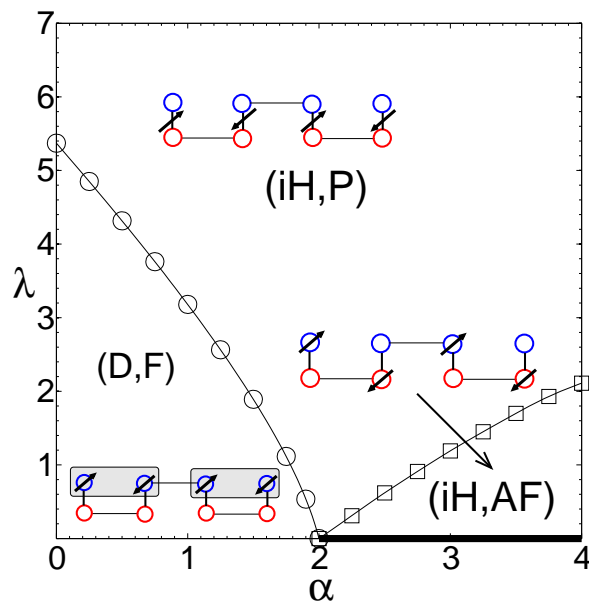


Figure 4.2: Ground-state phase diagram of the model for  $\Delta = 0$ . The first and second phases in brackets refer to spin and orbital sectors, respectively.

On the contrary, with increasing  $\lambda$  the orbital degrees of freedom experience an Ising transition from AF to paramagnetic (P) phase with  $\langle \sigma_i^z \rangle = 0$ . We have numerically confirmed this picture by means of DMRG in terms of MPS (with periodic boundary conditions up to  $N = 32$  rungs/wells). The Ising transition line in Fig.4.2 was obtained by locating the peak in the fidelity susceptibility (see chapter 7).

For  $\lambda = 0$  and  $0 < \alpha < 2$ , the exact ground state is two-fold degenerate and represents a direct product of ferro (F) orbital order,  $\langle \sigma_i^z \rangle = +1$  ( $-1$ ), and spontaneously dimerized Majumdar-Ghosh (MG) state [81] in spins, characterized by the formation of spin singlets on odd (even) bonds. We call this phase a dimer-ferro (D,F). An infinitesimal  $\lambda$  generates an exchange between the disconnected nearest-neighbour dimers,  $\sim \lambda^4 \sum \mathbf{S}_{2i+1} \mathbf{S}_{2i+2}$ . With increasing  $\lambda$ , the dimerization order in spins,  $D = \frac{1}{N} \sum_i (-1)^i \langle \mathbf{S}_i \mathbf{S}_{i+1} - \mathbf{S}_i \mathbf{S}_{i-1} \rangle$ , disappears together with the orbital ferro order via the quantum phase transition (open circles in Fig.4.2) that is identical to the one in a spin 1/2, SU(2) symmetric chain for  $j_2 \approx 0.241j_1$  [82, 83]. The quantum phase transition line has been obtained by using Lanczos diagonalization (for up to  $N = 12$  rungs/wells) and extrapolating the level crossing between the first excited singlet of the (D,F) phase and the first excited triplet of the (iH,P)

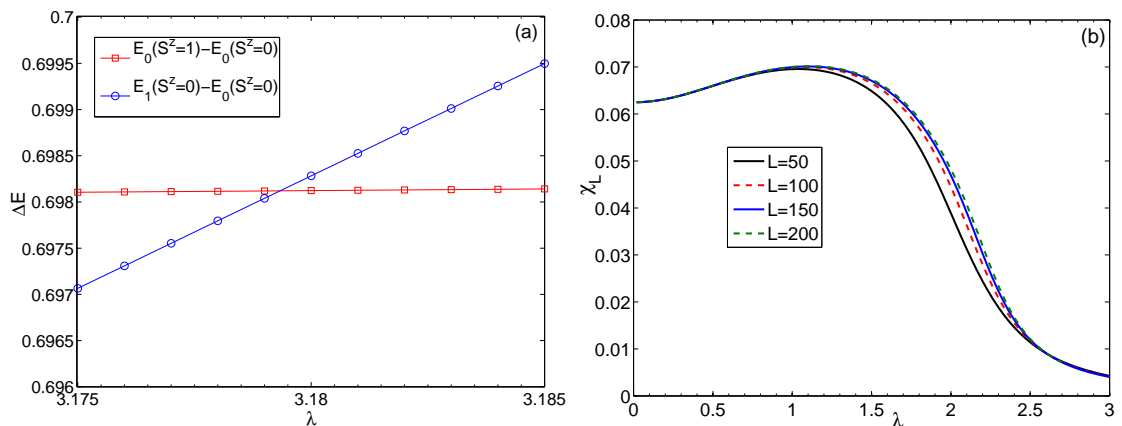


Figure 4.3: (a). Level crossing between the first excited singlet (blue circle) of the (D,F) phase and the first excited triplet (red square) of the (iH,P) phase for  $\Delta = 0$  and  $\alpha = 1$ . (b). Fidelity susceptibility between (D,F) and (iH,P) phase to up  $L = 200$  rungs with the same  $\Delta, \alpha$ .

phase [82], (see Fig.4.3(a)). Note that, there is a peak for fidelity susceptibility between (D,F) phase and (iH,P) phase (see Fig.4.3(b)). However, fidelity susceptibility in the vicinity of Berezinskii-Kosterlitz-Thouless (BKT) transition does not diverge but logarithmically converges (see chapter 7 for details of fidelity susceptibility at BKT transitions). So we use the level crossing instead of fidelity susceptibility to denote the BKT phase transition.

## 4.4 Relevant regime in solid-state systems

### (a) Analytical estimates

We now turn to the case of finite  $\Delta$ . We focus on the regime  $\alpha = 1$  relevant to realistic condensed-matter systems [64,77–79]. For  $\lambda = 0$ , a mean-field comparison of the energies of different product states shows that the ground state for  $\Delta > 2(2 - \alpha)$  is a direct product of a fully polarized spin state and an AF ordered orbital state (F,AF). For  $\Delta < 2(2 - \alpha)$  a (D,F) is found, in which once the spin dimerization pattern is spontaneously chosen, the direction of orbitals becomes unambiguously selected.

For weak  $\lambda$ , the leading spin exchange in the (D,F) phase along the weaker

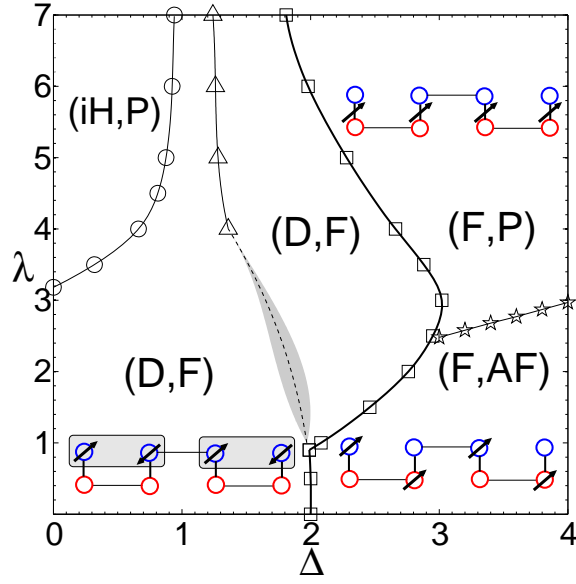


Figure 4.4: Ground-state phase diagram of the model for  $\alpha = 1$ . The first and second phases in brackets refer to spin and orbital sectors, respectively. The para state of orbitals, characterized with equal occupancy of both sites of each rung, is indicated by spins located on rungs.

(interdimer) bonds is ferromagnetic  $\sim -\lambda^2\Delta \sum \mathbf{S}_{2i+1}\mathbf{S}_{2i+2}$  for  $\Delta > 0$ , contrary to the AF spin exchange  $\propto \lambda^4$  for  $\Delta = 0$ . There is hence a competition between  $\Delta$  the and  $\lambda$  terms, and thus the character of spin correlations on weak bonds,  $\langle \mathbf{S}_{2i+1}\mathbf{S}_{2i+2} \rangle$ , changes at  $\Delta_{MG} = \lambda^2/4 + O(\lambda^4)$  from AF ( $\Delta < \Delta_{MG}$ ) to F ( $\Delta > \Delta_{MG}$ ) resembling the behavior of the spin  $1/2$   $j_1 - j_2$  model across the MG point [83].

For  $\lambda \rightarrow \infty$ , the orbital degrees of freedom are quenched. We may then write  $H = H_0 + H'$ , where  $H_0 = -\lambda \sum_i \sigma_i^x + 2(1 - \Delta) \sum_i \mathbf{S}_i \mathbf{S}_{i+1}$ , and  $H'$  may be treated as a perturbation. At first order in  $1/\lambda$  the system becomes equivalent to a spin  $1/2$   $j_1 - j_2$  chain,  $H_S = \sum_i [j_1 \mathbf{S}_i \mathbf{S}_{i+1} + j_2 \mathbf{S}_i \mathbf{S}_{i+2}]$  with  $j_1 = 2(1 - \Delta) + (4 + \Delta + \Delta^2)/2\lambda$  and  $j_2 = \lambda^{-1}$ . Contrary to the naively expected direct (iH,P) to (F,P) transition for large  $\lambda$ , the system starting from the (iH,P) state necessarily enters, for growing  $\Delta$ , first into a spin-dimerized state at  $j_2 \simeq 0.241j_1$ , corresponding to  $\Delta_c \simeq 1 - 1/2\lambda$ . Once the spins dimerize, the orbitals show a finite ferro response,  $\langle \sigma_i^z \rangle \sim -D/\lambda$ . This may be easily understood, since the orbitals experience a uniform magnetic field along  $z$ , proportional to the dimerization  $D$  due to the linear coupling between spin dimerization and orbitals,  $\sum_i (-1)^i (\mathbf{S}_i \mathbf{S}_{i+1} - \mathbf{S}_i \mathbf{S}_{i-1}) \sigma_i^z$  present in Hamiltonian



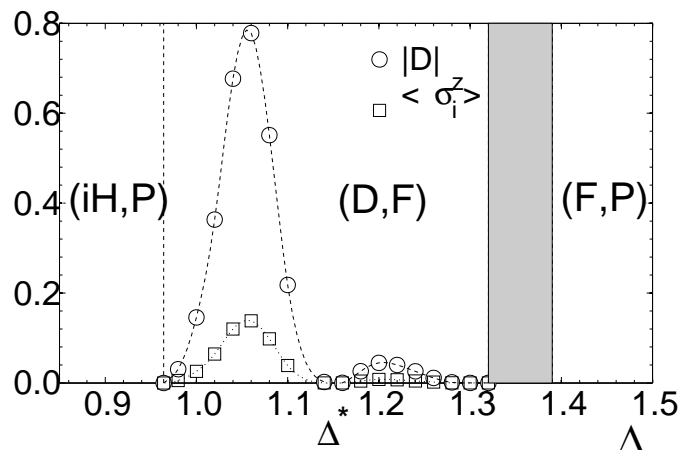


Figure 4.5: Spin dimerization amplitude  $|D|$  and  $\sigma_j^z$  for  $\lambda = 12$  and  $\alpha = 1$ . Within the shaded area, dimerization and orbital ferro orders cannot be resolved numerically.

Eq.(4.2.6).

At  $j_1 = 2j_2(\Delta_{MG} \simeq 1 + 1/2\lambda)$ , the ground state of the effective spin model is an MG state with dimerization  $D \simeq 3/4$ . Increasing further  $\Delta$ , at  $\Delta^* \simeq 1 + 3/2\lambda$  the nearest-neighbor coupling vanishes,  $j_1(\Delta^*) = 0$ , and the system decouples into two subchains. Hence, at the  $\Delta = \Delta^*$  line  $j_1$  changes its sign from antiferro ( $\Delta < \Delta^*$ ) to ferro ( $\Delta > \Delta^*$ ), whereas  $j_2$  remains positive. Bosonization results, supported by recent numerical studies, predict that the ground state of two weakly coupled spin 1/2 chains is dimerized irrespective of the sign of  $j_1$  [84–86]. Hence, in our case there is a special fine-tuning line bisecting the dimerized phase,  $\Delta = \Delta^*$  line, described by a double BKT [88] phase transition where spin dimerization and ferro-orbital order both vanish.

### (b) Numerical results

Our numerical calculations confirm the phases and phase transitions discussed above. For  $\lambda \gtrsim 4$ , the double-BKT phase transition line bisecting the (D,F) phase (see Fig.4.4) was determined from vanishing dimer order using iTEBD. Figure.4.5 shows the results for the dimerization  $D$  and for  $\langle \sigma_j^z \rangle$ , showing that both order parameters vanish simultaneously at  $\Delta = \Delta^*$  and then reopen again. At  $j_1 = -4j_2$ ,

there is a first-order phase transition line separating (D,F) and (F,P) states at  $\Delta_F \simeq 1 + 7/2\lambda$ . The first-order phase transition from (D,F) into (F,AF) or (F,P) (bold line in Fig.4.4) was obtained using DMRG from the jump of the total spin of the ground state from 0 to  $N/2$ .

Similar to the  $\Delta = 0$  case, we monitor the peak in the fidelity susceptibility obtained in DMRG simulations to determine the Ising transition between (F,AF) and (F,P), which accurately follows the analytical line  $\lambda = \Delta/2 + \alpha$ . Finally, for smaller values of  $\lambda$ ,  $1 < \lambda \lesssim 4$  (narrow shaded region in Fig.4.4), we observe by means of iTEBD simulations an intermediate fourfold degenerate phase.

## 4.5 Regime beyond solid-state systems

In this section we go beyond the usual case in solid-state systems ( $\alpha = 1$ ). We show that for  $U/V > 2$  the ground-state diagram contains a spin-orbital liquid phase with a finite magnetization.

### (a) Analytical estimates

For the case  $\lambda = 0$ , i.e., when the orbitals are classical, the phase diagram of the Eq.(4.2.6) can be easily established and is shown in Fig.4.6(a). The  $\alpha > 2$  region is dominated by a phase with FM spin order and AF orbital order, which we label (F,AF)  $|\uparrow\uparrow\uparrow\uparrow \cdots\rangle_S \otimes |\uparrow\downarrow\uparrow\downarrow \cdots\rangle_\sigma$ , as we did before. A smaller  $\alpha$  favors the spontaneously dimerized (D,F) state, with the spin sector described by a product of singlets on even (odd) NN bonds and ferromagnetic orbitals. On the line  $\Delta = 0$ ,  $\lambda = 0$ ,  $\alpha > 2$  the spins are fully decoupled, whereas adding infinitesimally small  $\Delta(\lambda)$  favors FM (AF) spin exchange. This competition between  $\lambda$  and  $\Delta$  leads to a first-order transition from the (F,AF) phase to the (iH,AF) phase where the spin sector behaves as an isotropic Heisenberg antiferromagnet, and the orbitals retain AF order  $|\uparrow\downarrow\uparrow\downarrow \cdots\rangle_S \otimes |\uparrow\downarrow\uparrow\downarrow \cdots\rangle_\sigma$ . For  $\lambda, \Delta \rightarrow 0$  this transition line can be easily estimated by computing the leading order correction in  $\lambda$  to the energy  $E_m(k)$  of a magnon in the (F,AF) state. For small momenta  $k$ , one obtains  $E_m(k) \rightarrow (2\Delta - \frac{\lambda^2}{8(\alpha-2)})k^2$ , collapsing at  $\lambda = \lambda_F = 4\sqrt{(\alpha-2)\Delta} + O(\Delta^{3/2})$ . A further increase of  $\lambda$  at fixed small  $\Delta$  eventually leads to an Ising transition in the orbital sector, bringing the system

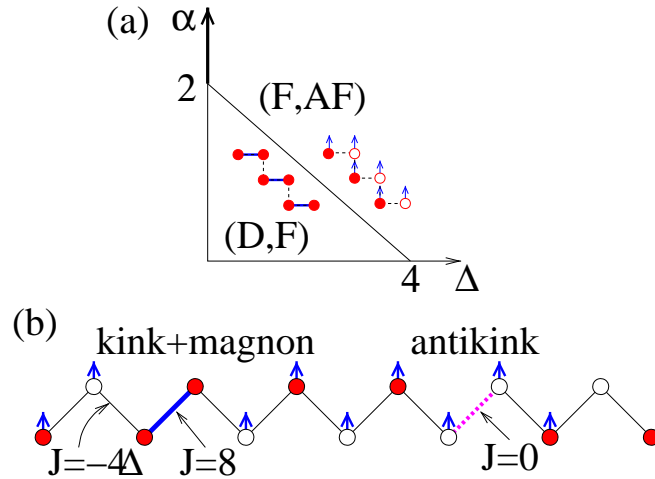


Figure 4.6: (a) Phase diagram of the model for  $\lambda = 0$ . (b) A sketch of the kink-magnon bound state in the (F,AF) phase, where  $J$  denotes the effective spin exchange on the corresponding link. A magnon binds only to the orbital kink, but not to the antikink. Open and solid circles show the occupied orbital states  $\sigma^z = \pm 1$

into the (iH,P) phase with paramagnetic orbitals  $|\uparrow\downarrow\uparrow\downarrow \cdots\rangle_S \otimes |\rightarrow\rightarrow\rightarrow\rightarrow \cdots\rangle_\sigma$ .

The (F,AF) ground state factorizes into a product of spin and orbital wave functions, so there is a purely orbital Ising-type transition from the (F,AF) phase to the (F,P) phase where orbitals are paramagnetic (disordered) and spins fully polarized,  $|\uparrow\uparrow\uparrow\uparrow \cdots\rangle_S \otimes |\rightarrow\rightarrow\rightarrow\rightarrow \cdots\rangle_\sigma$ ; the transition line thus can be obtained exactly as  $\lambda = \lambda_{Ising} = \alpha + \Delta/2$ .

However, there is another instability of the (F,AF) phase which is of crucial interest here. This instability can be traced down to the fact that in the (F,AF) phase magnons tend to bind to kinks in the orbital order (Fig.4.6(b)). If a kink-antikink pair is excited on top of the (F,AF) state, on the link at the kink position the effective exchange  $J$  changes from ferromagnetic ( $J \approx -4\Delta$  in zeroth order in  $\lambda$ ) to antiferromagnetic ( $J \approx 8$ ), acting as an impurity which can bind a magnon. There is another impurity link with  $J \approx 0$  at the antikink position, but it does not support bound states. To the leading order in  $\lambda$ , the energy of the kink-antikink pair with a magnon bound to the kink is

$$E_{bs}(p, k) = 4\alpha + 2\Delta - 8 + 8\Delta/(\Delta + 4) + 2\lambda\{[(8 - \Delta^2)/(4 + \Delta^2)] \cos(p) - \cos(k)\} \quad (4.5.1)$$

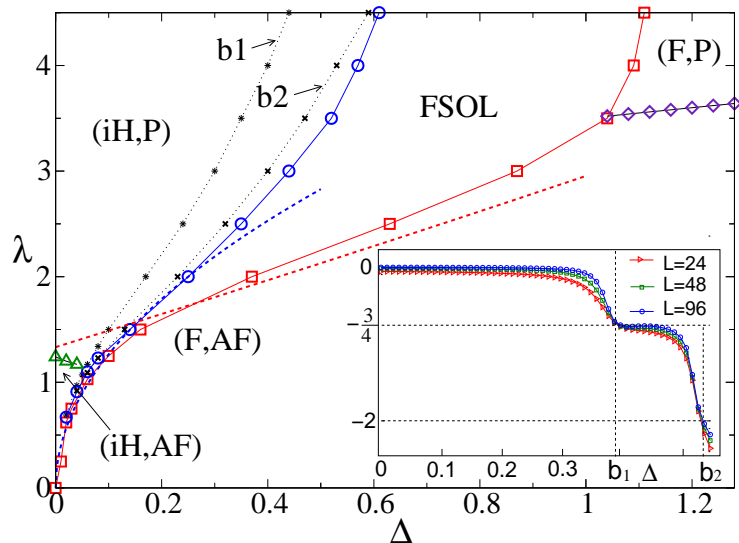


Figure 4.7: Phase diagram for  $\alpha = 3$ . Symbols denote numerical results, whereas dashed lines correspond to the analytical estimates  $\lambda_F$  and  $\lambda_c$ . Curves  $b_1$  and  $b_2$  mark the boundary phase transitions that involve nonlocal entanglement between edge spins  $\tau_1 = \mathbf{S}_1 + \mathbf{S}_2 + \mathbf{S}_3$  and  $\tau_N = \mathbf{S}_N + \mathbf{S}_{N-1} + \mathbf{S}_{N-2}$ . The inset shows the ground-state correlation between edge spins  $\langle \tau_1 \cdot \tau_N \rangle$  as a function of for  $\lambda = 4$ .

where  $p$  and  $k$  are the kink and antikink momenta, respectively. The lower edge of this continuum is achieved at  $p = \pi$ ,  $k = 0$ , i.e., when the magnon is essentially a propagating singlet dimer. This excitation softens at  $\lambda = \lambda_c = \frac{4}{3}(\alpha - 2) + \frac{2}{9}(\alpha + 4)\Delta + O(\Delta^2)$ . Hence, for  $\alpha > \alpha_c$  a different phase is expected with a finite density of composite kink-dimer particles floating in the ferromagnetic background. An infinitesimal density of moving kinks and antikinks immediately suppresses the orbital order, so the orbital AF order parameter experiences a jump at the transition. Indeed, the (F,AF) product wave function remains an exact eigenstate all the way up to  $\lambda = \lambda_c$ , and  $\lambda_c$  remains smaller than the Ising transition value  $\lambda_{Ising}$  in a finite range of  $\Delta$ . The ferromagnetic order in spins is retained, but the magnetization is no more fully saturated.

In the phase mentioned above, the  $SU(2)$  symmetry in the spin sector remains spontaneously broken, exactly as in the (F,AF) phase, but the ground state belongs to a degenerate multiplet with some spin  $S_{tot} < N/2$ , where  $N$  is the number of particles ( $N = L$  at unit filling considered here). This phase is expected to have

two branches of gapless excitations, one with a quadratic dispersion at small momenta ("spin" mode, ferromagnetic magnons), and the other with a linear dispersion ("charge" mode, sound waves in the Luttinger liquid of kink dimer particles). This resembles the situation found in spin 1/2 Bose gas, where such a spin-charge separation has been found both in the 1D [89–92] and two-dimensional (2D) [93] cases. Since the longitudinal spin correlator is related to the kink dimer density fluctuations, it must decay algebraically on top of the long-range order. This highly unusual phase can be called a ferromagnetic spin-orbital liquid (FSOL) [94].

### (b) Numerical results

Our DMRG results confirm the analytical arguments given above. Figure 4.7 shows our numerical results for the  $(\lambda, \Delta)$  phase diagram of the 1D version of the Eq.(4.2.6) at  $\alpha = 3$ . We considered open systems consisting of up to  $L = 96$  sites, monitoring different correlation functions, total spin of the ground state, and fidelity susceptibility to detect phase boundaries. In addition, we have checked our data on systems of up to  $L = 48$  sites with periodic boundary conditions. We have typically kept up to 800 states (within a subspace with fixed  $S^z$ ) in our DMRG calculations.

We indeed observe the FSOL phase in a wide region of  $\Delta$  and  $\lambda$ . As shown in Fig.4.8(a), spontaneous magnetization in the FSOL phase changes smoothly, confirming that there is no gap for single-particle excitations. In accordance with the composite-particle transition mechanism outlined above, there is a clear correlation between the peaks in the densities of orbital domain walls and magnons (Fig.4.8(b)). We have checked that such a correlation persists at all magnetization values, and that the number of peaks in the domain wall density is always equal to the number of magnons in the ground state.

Moreover, the energy of the lowest excitation in the same  $S^z$  sector as the ground state (the particle-hole gap) scales as  $L^{-1}$  with the system size  $L$ , while that in the sector corresponding to adding a magnon scales as  $L^{-2}$ , as shown in Fig.4.8(c) and Fig.4.8(d). Thus these are two gapless excitation branches with linear and quadratic dispersion, respectively.

The phase transition from (iH,P) into (F,P) is first order, as the total spin jumps

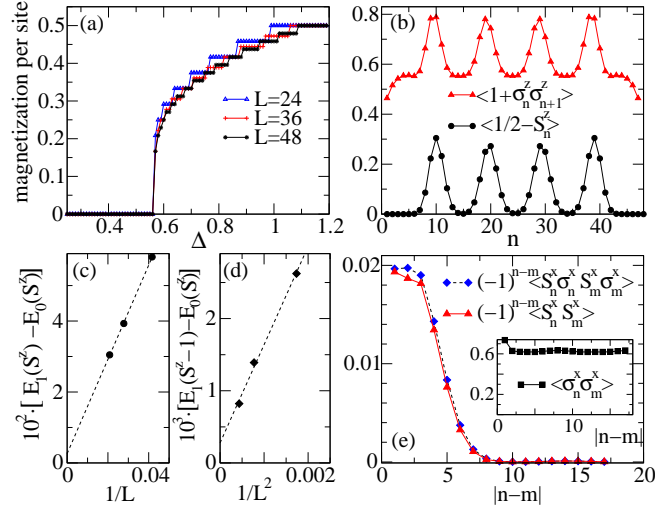


Figure 4.8: Properties of the FSOL phase for  $\alpha = 3$  and  $\lambda = 4$ : (a) Magnetization curve for different system sizes  $L$ ,  $\sum_i \langle S_i^z \rangle / L$ ; (b) Magnon density (circles) and orbital domain wall density (triangles) in the ground state at  $\Delta = 1.02$ ,  $S^z = 44$ ; Finite-size scaling of the particle-hole (c) and magnon (d) excitation gaps at  $S^z = N/3$ ; (e) ground-state correlators for  $\Delta = 0.86$ ,  $L = 48$ .

abruptly from 0 to  $L/6$ . Similarly, the transition from (F,AF) into FSOL is first order since the AF orbital order in  $\sigma_z$  changes discontinuously. In contrast to that, the transition from (F,P) into FSOL seems second order of the commensurate-incommensurate type (even though the system sizes studied are not enough to observe a square root behavior of the kink-magnon density close to the fully polarized state), since all quantities observed change in a continuous manner. The minimal model capturing this transition is a system of two-component repulsive  $SU(2)$ -symmetric bosons undergoing a transition from vacuum into a finite density state driven by a chemical potential. Note that this finite density state is not a two-component Luttinger liquid, since the continuous  $SU(2)$  symmetry is spontaneously broken.

In the FSOL phase the correlators  $\langle S_i^x S_{i'}^x \rangle$  and  $\langle S_i^x \sigma_i^x S_{i'}^x \sigma_{i'}^x \rangle$  are very close to each other, despite the fact that  $\langle \sigma_i^x \sigma_{i'}^x \rangle$  can be significantly lower than one (Fig.4.8(e)). In fact, for the parameters presented in Fig.4.8(e),  $\langle S_i^x \sigma_i^x S_{i'}^x \sigma_{i'}^x \rangle$  is larger in absolute value than  $\langle S_i^x S_{i'}^x \rangle$  even though  $|\langle \sigma_i^x \sigma_{i'}^x \rangle| \sim \langle \sigma_i^x \rangle^2 \simeq 0.6$ , where the finite value of

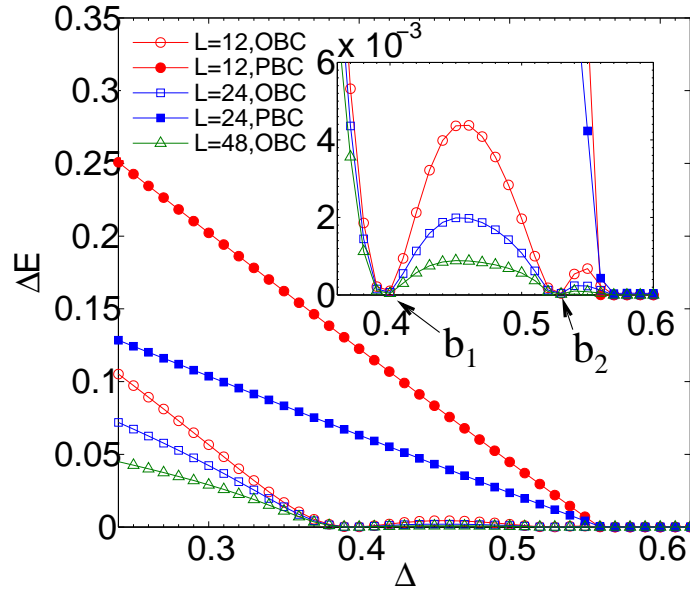


Figure 4.9: Excitation gap for open (empty symbols) and periodic (full symbols) boundary conditions as a function of  $\Delta$  and  $L$ . The inset zooms in the region  $0.36 < \Delta < 0.6$ , revealing the existence of the two boundary transitions at  $b_1$  and  $b_2$ .

$\langle \sigma_l^x \rangle$  is induced by the coupling  $\lambda$  in Eq.(4.2.6). One can straightforwardly check that this follows from the fact that the wave function of the bound state is very close to a singlet bond across the orbital domain wall, so that the operator  $S_l^+(1 - \sigma_l^x)$  nearly annihilates the ground state.

### (c) Boundary Phase Transitions

In addition to the existence of the FSOL phase, the spin-orbital model with  $\alpha > 2$  is characterized by the appearance of peculiar boundary phase transitions within the (iH,P) phase (curves  $b_1$  and  $b_2$  in Fig.4.7 at which the behavior of the edge spins in open chains changes drastically. When increasing  $\Delta$  at fixed  $\lambda$ , localized and strongly correlated  $S = 1/2$  edge spins emerge when crossing the  $b_1$  curve. Further increasing  $\Delta$  leads to a second transition at the  $b_2$  line, where the value of the boundary spin changes from  $S = 1/2$  to  $S = 1$ . This effect is illustrated in the inset of Fig.4.7, where the correlation between edge spins is depicted as a function of  $\Delta$  for  $\lambda = 4$  [31].

The boundary transitions inside the (iH,P) phase are peculiar in 1D, since edge spins are separated by a macroscopic distance, and the only way to communicate

between them is through the bulk from which they effectively decouple. To prove that we are dealing with a boundary phenomenon we compare the excitation gaps for open and periodic boundary conditions. One can clearly see from Fig.4.9 that low-lying states below the bulk modes develop for open boundary conditions. Another illustration of this boundary transition is provided by Fig.4.10, which shows the behavior of the first excited states in the  $S^z = 1$  and  $S^z = 2$  sector and the bulk excitation.

To describe the physics of this transition at the qualitative level, it is instructive to consider the limit of large  $\lambda$ . In the strong  $\lambda$  limit one can integrate out orbital degrees of freedom to obtain an effective spin-1/2 model. In the leading order in  $1/\lambda$ , its Hamiltonian has the form of a  $J_1 - J_2$  model with modified first and last nearest-neighbor links:

$$H_S = j_1 \sum_{n=2}^{N-2} \mathbf{S}_n \cdot \mathbf{S}_{n+1} + j_2 \sum_{n=2}^{N-1} \mathbf{S}_{n-1} \cdot \mathbf{S}_{n+1} + j'_1 (\mathbf{S}_1 \cdot \mathbf{S}_2 + \mathbf{S}_{N-1} \cdot \mathbf{S}_N) \quad (4.5.2)$$

where  $j_1 = 2(1-\Delta) + \frac{4+(1+\Delta)(\Delta+2-2\alpha)}{2\lambda}$ ,  $j_2 = 1/\lambda$ , and  $j'_1 = j_1 + \frac{1-2\alpha}{2\lambda}$ . One can see that with increasing  $\Delta$ , the boundary link strength  $j'_1$  goes through zero at some point and changes its sign to a ferromagnetic coupling. This effectively creates "impurity" spins attached ferromagnetically at the ends of the spin-1/2 chain. Interaction between the end spins is mediated by the bulk. For an even number of sites the effective interaction is antiferromagnetic, whereas for an odd number of sites the effective interaction between the end spins is ferromagnetic.

The second boundary transition, *b2*, is similar in nature to the first one, but now the last two spins decouple from the bulk, creating an effective spin-1 localized at each boundary that is ferromagnetically attached to the antiferromagnetic spin-1/2 chain. The interaction between the spin-1 edge impurities is antiferromagnetic for an even number of sites and ferromagnetic for an odd number of sites. The lowest excitations are boundary excitations: a boundary triplet with total spin  $S^T = 1$ , and a boundary quintet with  $S^T = 2$  with a slightly higher energy. The next excitation is the bulk excitation with  $S^T = 3$ , which is similar to the excitation of purely Heisenberg model (see (c) and (d) of Fig.4.10).



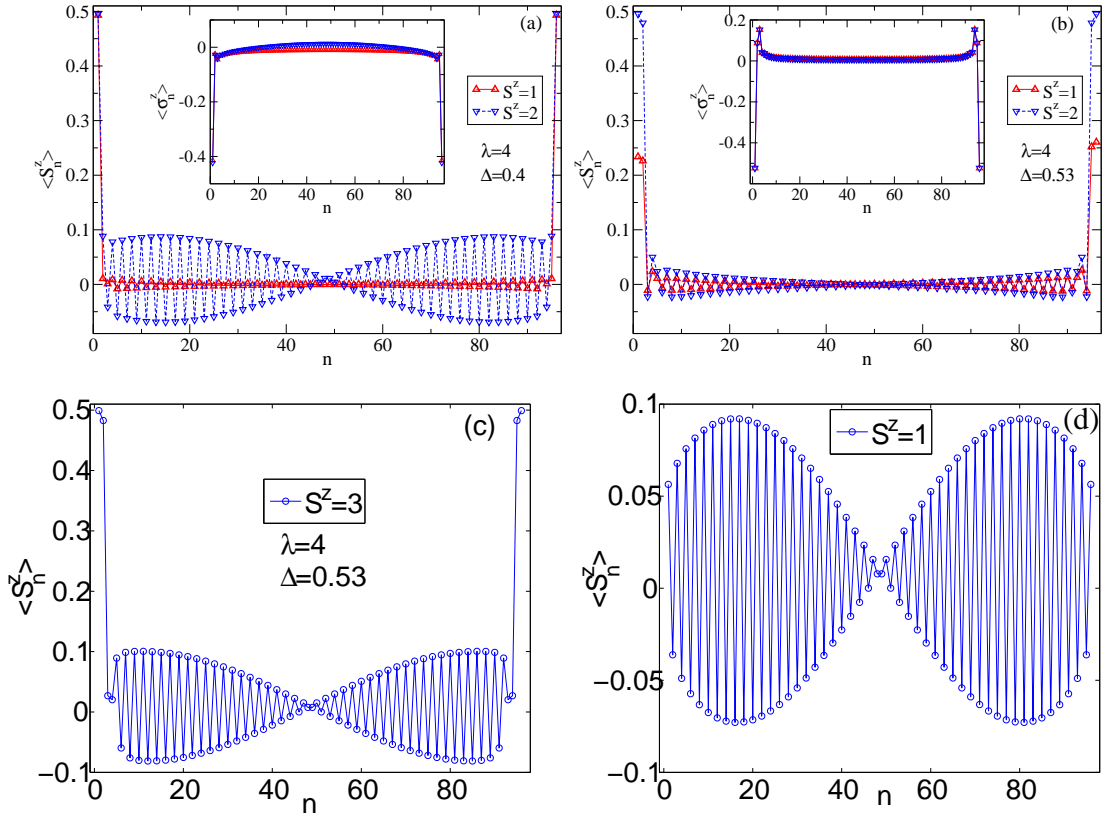


Figure 4.10: Distribution profiles in the ground states. (a) At a point between the b1 and b2 boundary transition lines, the  $S^z = 1$  excitation is localized at the system edges, while the  $S^z = 2$  excitation belongs to the bulk; (b) at another point between the b2 line and the boundary of the FSOL phase, both  $S^z = 1$  and  $S^z = 2$  excitations are localized at the edges, (c) the  $S^z = 3$  excitation belongs to the bulk; (d) bulk excitation  $S^z = 1$  for Heisenberg model

## 4.6 Experimental realization

The spin-1/2 system discussed in Eq.(4.2.6) may be realized with polar diatomic molecules using two hyperfine states related to the nuclear spin of the constituent atoms. The hyperfine structure of the molecules may be controlled to a large extent [95]. In particular, mixtures of two hyperfine states (with two different total nuclear spin projections  $m_I$ ) can be created. Polarization results from the admixture of rotational states due to the Stark effect induced by an external electric field. Note that for a rotational state  $N \neq 0$ , electric quadrupole interaction mixes different hyperfine states with the same  $m_N + m_I$ . Since the Stark effect couples states with

the same  $m_N$ , the resulting dressed states may be characterized by the  $m_I$  value of the bare state, without electric field. The spin 1/2 system may be hence encoded in chemically nonreactive polar molecules in two different  $m_I$  values.

Here we have assumed that the short-range collisional physics is spin independent and hence that the intermolecular short-range interactions are insensitive to the nuclear spin projection. This assumption is in agreement with the experimental results obtained in Ref. [95], where within the time scale of the experiments no significant spin-changing collisions were observed in mixtures of hyperfine states, indicating that the interactions are, if at all, only very weakly dependent on the nuclear spin projection.

The interactions may present some very small residual dependence on the nuclear spin, but following the results of Ref. [95], we assume this residual spin dependence to be much smaller than other energy scales discussed in the problem. The only concern would be the long-term stability of the system against spin-changing collisions, which although rare may still be possible due to any residual spin dependence. This may be suppressed, however, by placing the molecules in the two lowest states of the hyperfine manifold.

Dipolar spinor fermions may also be realized using employing atoms with large magnetic dipole moments, such as chromium [72], dysprosium [73], or erbium [96]. For the particular case of  $^{53}\text{Cr}$ , in a strong magnetic field, any two of the four lowest energy states  $|F, m_F\rangle = |\frac{9}{2}, -\frac{9}{2}\rangle, |\frac{9}{2}, -\frac{7}{2}\rangle, |\frac{9}{2}, -\frac{5}{2}\rangle,$  and  $|\frac{9}{2}, -\frac{3}{2}\rangle,$  can be chosen to simulate the  $\uparrow$  and  $\downarrow$  pseudospin- $\frac{1}{2}$  states. Those states have approximately the same large magnetic moments, given by the electronic spin projection  $m_s = -3,$  differing only by their nuclear moment. The total interparticle potential is of the form in Eq.(2.3.3)

## 4.7 Conclusion

Dipolar fermions on zig-zag lattices can capture relevant spin-orbital models of realistic d-electron systems and allow exploration of parameter regimes which are hardly accessible for solid-state compounds. Moreover, the quantum nature of or-

bital fluctuations can be revived, which combined with geometric frustration and spin dynamics, produces an intriguing, rich, ground-state phase diagram, including a spin-orbital liquid phase characterized by a finite but unsaturated magnetization. This phase, as a ferromagnet, has spontaneously broken  $SU(2)$  symmetry, but, unlike a ferromagnet, it has algebraically decaying longitudinal spin correlations. Remarkably, its magnetization changes continuously from saturation value with a change of the model parameters, in the absence of any magnetic field. This phase can be viewed as a Luttinger liquid of bound composites of singlet spin dimers and orbital domain walls on top of a fully polarized ferromagnetic phase.

We have assumed above unit occupation per rung/well for which dipolar interactions were necessary for realizing a Mott insulating state. As a remark, we would like to point out that the case of two fermions per rung/well does not require dipolar interactions. Placing two fermions per well, both in  $p$  orbitals, in the zig-zag geometry, due to Hund's coupling a total  $S = 1$  state is formed in each well for  $\lambda \ll J_H$ , hence realizing the Haldane phase of a spin-1 chain.

Finally, we remark that observation of this magnetized spin-orbital liquid demands to cool down the system to the temperatures of the order of the spin-coherence scale  $4t^2/U$ , which constitutes a major experimental challenge presently [97].



# Chapter 5

## Spin-orbital models of dipolar bosons in zig-zag optical lattices

### 5.1 Introduction

With the realization of the Mott-insulator state of ultracold Bose gas loaded in an optical lattice [15] the groundwork for experimental simulation of magnetism of many-body systems with bosons [12, 13, 98] was laid. Since then, with the help of shaking techniques, classical frustrated magnetism has been implemented successfully on triangular lattices [70]. The next target is to simulate quantum magnetism and in particular frustrated quantum spin systems to compensate for the nonexistence of unbiased analytical or numerical methods and observe plausible unconventional ground states á la spin liquids [99, 100]. Short-range quantum spin correlations for two-component alkali (contact interacting) Bose gases was exhibited in optical lattices [101]. Using bosonic dipolar atoms ( $^{52}\text{Cr}$  with strong magnetic dipole moment) nonequilibrium quantum magnetism with long-range exchange physics has been reported in recent experiments [102]. However, a technological breakthrough is needed in reducing temperatures below the spin coherence scales to simulate ground-state equilibrium quantum magnetism in experiments on ultracold gases [97]. Interestingly, as we show in this chapter, lattice bosons can serve as well as excellent simulators of a novel macroscopic quantum effect such as topological order-by-disorder that it is possible to study by simple and at the same time solid

arguments.

## 5.2 Spin-orbital model for bosons

As for the case of fermionic dipoles discussed in the previous chapter, dipolar spinor bosons may be realized using diatomic polar molecules with an electric dipole moment (e.g., potassium-rubidium  $^{41}\text{K}$   $^{81}\text{Rb}$  [103]) where spin-1/2 degrees of freedom may be encoded in two different total nuclear spin projections of molecules (similar to fermionic case  $^{40}\text{K}$   $^{81}\text{Rb}$  [95]), resulting in the fact that both the long-range part as well as short-range interactions are largely spin independent.

We consider two-component (pseudo-spin-1/2) dipolar bosons loaded in doubly degenerate  $p$ -bands of a quasi-1D zig-zag lattice (see Fig.4.1). The system is described by the Hubbard-type Hamiltonian (Eq.(2.5.20)). We derive in the following the effective spin-orbital model for models Eq.(2.5.20). As shown in chapter 4, there are two possible processes contributing to the effective Hamiltonian. However, if the particles are bosons, the two particle states must be in a triplet spin state for the first process instead of singlet spin state for fermions, and as a consequence the effective Hamiltonian for this first process acquires the form:

$$H_{i,j}^{b1} = - \left[ \left( \frac{t^2}{U + J_H} + \frac{t^2}{U - J_H} \right) P_{i,j}(S^T = 1) \right] [1 + (-1)^i \sigma_i^z] [1 + (-1)^i \sigma_i^z] \quad (5.2.1)$$

For the second process, similar arguments for fermions in chapter 4 are valid for bosons (but with opposite spin symmetry), which allow us to obtain the following effective Hamiltonian for bosons due to this process:

$$H_{i,j}^{b2} = - \left[ \frac{t^2}{2(V - J_H)} P_{i,j}(S^T = 0) + \frac{t^2}{2(V + J_H)} P_{i,j}(S^T = 1) \right] (1 - \sigma_i^z) \quad (5.2.2)$$

Putting these two contributions and the effective transversal term Eq.(4.2.5) shown in chapter 4 together, we obtain the effective spin-orbital models for bosons:

$$H_{eff}^b = \sum_i \left[ -2\mathbf{S}_i \mathbf{S}_{i+1} + \alpha - \frac{3}{2} \right] [1 + (-1)^i \sigma_i^z] [1 + (-1)^i \sigma_{i+1}^z] + \Delta \sum_i 2\mathbf{S}_i \mathbf{S}_{i+1} [1 - \sigma_i^z \sigma_{i+1}^z] - \lambda \sum_i \sigma_i^x \quad (5.2.3)$$

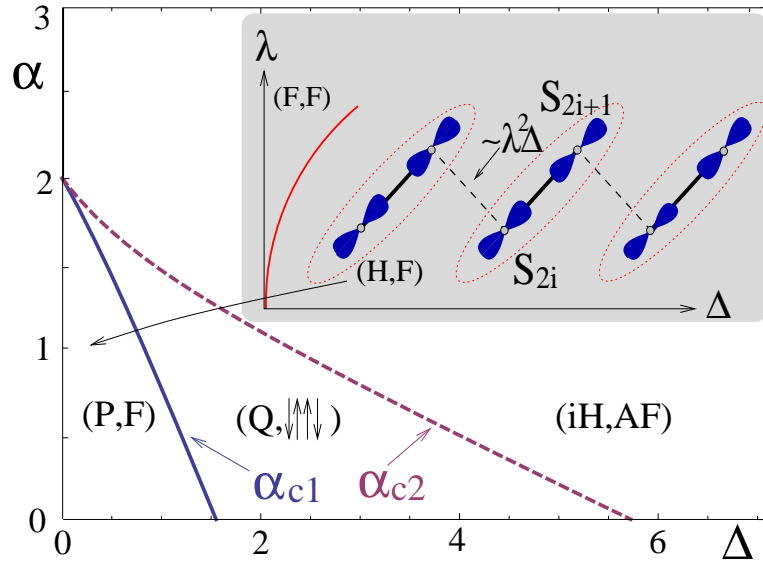


Figure 5.1: Exact analytical ground state phase diagram of the spin-orbital model with  $\lambda = 0$  obtained in thermodynamic limit. We employ (spin,orbital) notation for the different phases. The inset shows the ground-state orbital configuration of the (P,F) phase and the effect on this phase of infinitesimal quantum fluctuations in orbitals,  $\lambda$ . Dotted contours encircle 2 sites forming effective spins-1  $\mathbf{T}_i = \mathbf{S}_{2i} + \mathbf{S}_{2i+1}$ .

where we recall that we fix  $t^2/(2\tilde{U}) = 1$  and that  $\tilde{U} = (U^2 - J_H^2)/U$ ,  $\Delta = J_H \tilde{U}/(V^2 - J_H^2)$ , but now  $\alpha = \tilde{U}(V - J_H/2)/(V^2 - J_H^2)$ .

### 5.3 Ground state phases for classical orbitals

As for our discussion in the previous chapter, when  $\lambda = 0$  orbital variables in Eq.(5.2.3) are classical and it is easy to map out the ground-state phases in a product form of spin times orbital part. Depending on values of  $\alpha$  and  $\Delta$  only three different orbital configurations can be realized as ground states: a period-one ferromagnet (F) as indicated in the inset of Fig.5.1, a period-two antiferromagnet (AF) as depicted in Fig.5.2(b), and a period-four configuration  $\cdots p_y p_x p_x p_y \cdots$  ( $\downarrow \uparrow \uparrow \downarrow$ ) presented in Fig.5.2(a).

For  $\alpha > 2$  the first line in Eq.(5.2.3) selects the AF orbital configuration whereas the Hund coupling  $\Delta$  induces AF exchange between the spins located on orthogonal orbitals of neighboring sites. In the spin sector one recovers the isotropic Heisen-

berg antiferromagnet (iH) while in orbitals the doubly degenerate AF configuration remains. The ground-state energy per site in the (iH,AF) state is independent of  $\alpha$  and in the thermodynamic limit we can estimate it from the exact solution of the spin 1/2 AF Heisenberg chain,  $e_0^{iH} = \Delta(1 - 4 \ln 2)$ . There are no other phases for  $\alpha > 2$ .

The phase diagram is much more interesting for  $0 < \alpha < 2$  as presented in Fig.5.1. There, besides the (iH,AF) state we map out 2 additional ground states depending on  $\Delta$  coupling. For small values of  $\Delta$  the ground state is twofold degenerate and possesses F orbital order,  $\langle \sigma_i^z \rangle = +1(-1)$ . Choosing the  $\langle \sigma_i^z \rangle = +1$  orbital configuration (this particular orbital order is selected by open boundaries if the chain starts from even number sites.), two spins on the neighboring sites combine to form an effective spin-1  $\mathbf{T}_i = \mathbf{S}_{2i} + \mathbf{S}_{2i+1}$  in the ground state; however  $\mathbf{T}_i$  spins are completely decoupled from each other, thus resulting in an extensively degenerate paramagnetic ground state (P) of spin-1 chain for the spin part of the wave function, with the total degeneracy of the ground state  $2 \times 3^{L/2}$  where  $L$  is number of sites.

The energy per site for the (P,F) configuration is  $e_0^P = 2(\alpha - 2)$  and is independent of  $\Delta$ . Increasing  $\Delta$  induces a transition from a (P,F) state to a  $\downarrow\uparrow\uparrow\downarrow$  configuration of orbitals where bosons can hop only inside spontaneously selected 4-site clusters, as depicted in Fig.5.2. For the  $\downarrow\uparrow\uparrow\downarrow$  configuration of orbitals, coupling between the spins inside each decoupled cluster of 4 sites (see Fig.5.2) is given by  $4\Delta\mathbf{S}_1\mathbf{S}_2 - 8\mathbf{S}_2\mathbf{S}_3 + 4\Delta\mathbf{S}_3\mathbf{S}_4 + 4\alpha - 6$  and the ground state energy per site is  $e_0^Q = \alpha - 1 - \frac{\Delta}{2} - \sqrt{1 + \Delta + \Delta^2}$ . We denote this phase as  $(Q, \downarrow\uparrow\uparrow\downarrow)$  since spin exchanges have a quadrumerized pattern. Equating the two energies  $e_0^P = e_0^Q$  we obtain the phase transition line from the (P,F) to the  $(Q, \downarrow\uparrow\uparrow\downarrow)$  state,  $\alpha = \alpha_{c1} = 3 - \frac{\Delta}{2} - \sqrt{1 + \Delta + \Delta^2}$ , for any system size that is a multiple of 4.

Further increasing  $\Delta$  induces antiferromagnetism for bosons. The phase transition line from the  $(Q, \downarrow\uparrow\uparrow\downarrow)$  to the (iH,AF) state is obtained by setting  $e_0^Q = e_0^{iH}$  and is given in the thermodynamic limit as  $\alpha = \alpha_{c2} = 1 + (3 - 4 \ln 4)\Delta/2 + \sqrt{1 + \Delta + \Delta^2}$ . Different phases of bosons together with phase transition lines are presented in the analytical phase diagram in Fig.5.1.



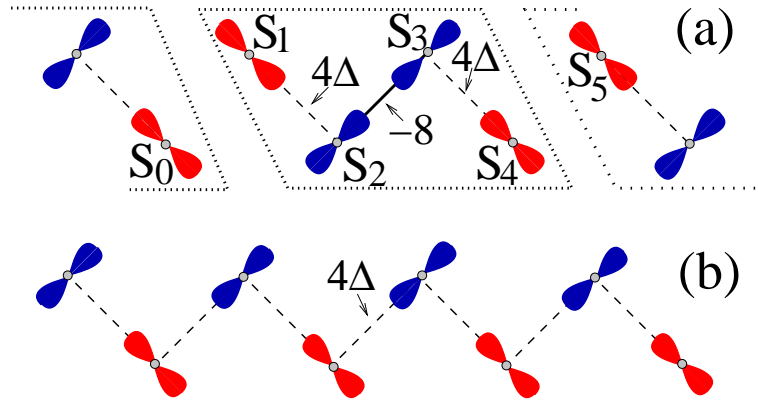


Figure 5.2: Ground-state orbital configurations in (a)  $(Q, \downarrow\uparrow\uparrow\downarrow)$  and (b)  $(iH, AF)$  phases. Only occupied orbitals are displayed per site. Dotted contour in (a) encircle clusters of 4 spins decoupled from the rest of the system. Continuous lines indicate ferromagnetic Heisenberg exchange between spins at neighboring sites  $-8\mathbf{S}_i\mathbf{S}_{i+1}$  and dashed lines indicate AF exchange  $4\Delta\mathbf{S}_i\mathbf{S}_{i+1}$ .

## 5.4 Topological order-by-disorder

### (a) Analytical estimates

In reality the zig-zag optical lattice is not strictly symmetric in the  $x - y$  plane; thus one has to consider the probability of mixing of orbitals  $\lambda \neq 0$ . First we will study analytically the limit  $\lambda \rightarrow 0$  where we will observe the topological order-by-disorder phenomenon. Later we address analytically  $\lambda \gg 1$  and show that topological order survives that limit.

An arbitrary weak quantum fluctuation  $\lambda$  on the (P,F) state of bosons acts as a transverse field in orbitals that tries to quantum-disorder orbital order in  $\sigma^z$  variables that is otherwise perfect for  $\lambda = 0$ . At the same time, most importantly, it introduces exchange interactions between the decoupled neighboring spins of the (P,F) state,

$$\lim_{\lambda \rightarrow 0} H_s = - \sum_i 8\mathbf{S}_{2i}\mathbf{S}_{2i+1} + \chi_\lambda \sum_i \mathbf{S}_{2i+1}\mathbf{S}_{2i+2} \quad (5.4.1)$$

Where  $\chi_\lambda \simeq \lambda^2\Delta/2(1 - \Delta)^2 - O(\lambda^4)$ . In particular, in the limit  $\lambda \rightarrow 0$  the two neighboring spins  $\mathbf{S}_{2i}$  and  $\mathbf{S}_{2i+1}$  are coupled ferromagnetically with each other with a strength that is infinitely stronger than the antiferromagnetic coupling between

$\mathbf{S}_{2i+1}$  and  $\mathbf{S}_{2i+2}$ . Hence for  $\lambda \rightarrow 0$  the ground-state wave function of the spin part of Eq.(5.4.1) coincides with the ground state of the spin-1 chain [104, 105] and a topological (H,F) state is established with nonlocal string order [106]. One can determine the boundary of the (H,F) state  $\Delta_F \sim \lambda^2$  for  $\Delta \rightarrow 0$ . For  $\Delta < \Delta_F$  the fully polarized (F,F) state is selected for the ground state, and for  $\Delta > \Delta_F$  the (H,F) state is stabilized. Thus, for  $\Delta > 0$  infinitesimal quantum fluctuations  $\lambda \rightarrow 0$  select from the extensively degenerate ground-state manifold (P,F) a doubly degenerate state for periodic boundary conditions (degeneracy is due to orbital F order) and a fourfold-degenerate state for open boundary conditions. As already mentioned open boundaries remove orbital degeneracy and hence the residual fourfold degeneracy is purely due to the edge spins of the topological state.

Extensive ground-state degeneracy at the classical level (similar to the (P,F) phase for  $\lambda = 0$ ) is a characteristic property of many frustrated spin systems [107]. If degeneracy can be lifted either by thermal [108, 109] or by quantum fluctuations [110, 111] and as a result magnetic order develops, such behavior is referred to as order-by-disorder. No unambiguous experimental confirmation of order-by-disorder has been reported in condensed matter magnetic systems, though there are suggestions to simulate it in experiments on ultracold spinor Bose gases [112, 113]. Order by quantum disorder in orbitally frustrated electron systems was predicted in two-dimensional square lattices [64]. Here we encounter the emergence of topological order by quantum disorder in orbitally frustrated one-dimensional dipolar spinor bosons.

Other phases depicted in Fig.5.1 are stable with respect to infinitesimal quantum fluctuations in orbitals  $\lambda$ . In particular in the  $(Q, \downarrow\uparrow\uparrow\downarrow)$  state the end spins of two adjacent decoupled (for  $\lambda = 0$ ) 4-spin clusters will get coupled due to  $\lambda$  by AF exchange; i.e., the cluster on Fig.5.2 will be coupled to its neighbors by terms  $\sim \Delta\lambda^2(\mathbf{S}_0\mathbf{S}_1 + \mathbf{S}_4\mathbf{S}_5)$ .

### (b) Numerical results

We support our analytical findings numerically by simulating directly the full microscopic spin-orbital model of Eq.(5.2.3). To address large systems we use the

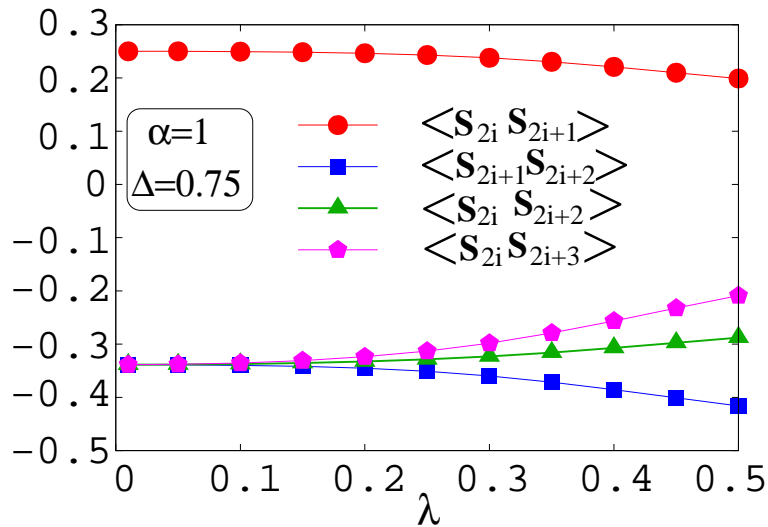


Figure 5.3: Bulk short-range spin correlation function's dependence on  $\lambda$  in (H,F) phase. Due to extensive degeneracy of ground states in (P,F) phase, numerically we cannot approach arbitrarily close to  $\lambda = 0$ , but the tendency is evident. Symmetry with respect to translations on 2 sites of (H,F) state imposes  $\langle \mathbf{S}_{2i} \mathbf{S}_{2i+1} \rangle = \langle \mathbf{S}_{2i+2} \mathbf{S}_{2i+3} \rangle$  and  $\langle \mathbf{S}_{2i} \mathbf{S}_{2i+2} \rangle = \langle \mathbf{S}_{2i+1} \mathbf{S}_{2i+3} \rangle$ .

DMRG method that is implemented best with open boundary conditions. The results of the numerical simulations of the spin-orbital model presented below are for open system with  $L = 96$  sites and we compare them with the analogous results for the Haldane chain on  $L = 48$  sites to show that for  $\lambda \rightarrow 0$  the ground-state configuration of the spin part of the spin-orbital model reproduces identically the topologically nontrivial ground state of the antiferromagnetic SU(2) symmetric spin-1 chain.

First we present numerical results of short-range ground state correlation functions between the neighboring spins as a function of  $\lambda$  in the (H,F) state in Fig.5.3 for  $\lambda \ll 1$ . As expected from analytical analyses one can observe in Fig.5.3 that in the limit  $\lambda \rightarrow 0$ ,  $\langle \mathbf{S}_{2i} \mathbf{S}_{2i+1} \rangle = \langle \mathbf{S}_{2i+2} \mathbf{S}_{2i+3} \rangle = 1/4$  and  $\langle \mathbf{S}_{2i+1} \mathbf{S}_{2i+2} \rangle = \langle \mathbf{S}_{2i} \mathbf{S}_{2i+2} \rangle = \langle \mathbf{S}_{2i+1} \mathbf{S}_{2i+3} \rangle = \langle \mathbf{S}_{2i} \mathbf{S}_{2i+3} \rangle \simeq -0.35$  so that  $\langle \mathbf{T}_i \mathbf{T}_{i+1} \rangle = \langle (\mathbf{S}_{2i} + \mathbf{S}_{2i+1})(\mathbf{S}_{2i+2} + \mathbf{S}_{2i+3}) \rangle \simeq -1.4 \simeq e_0(S = 1)$ , where  $e_0(S = 1)$  is the well known value of the ground-state energy per site of the spin-1 chain (in the units of exchange) that is equal to the ground-state correlation function of two neighboring spins of the Haldane chain.

The Néel correlation function  $(-1)^{j+i} \langle T_j^z T_{j+i}^z \rangle$  and string correlation function

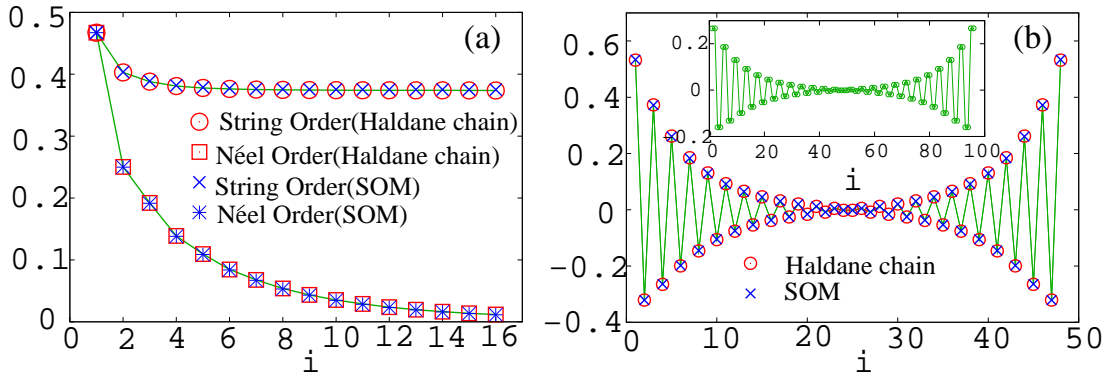


Figure 5.4: (a) Blue symbols: Bulk Néel order and string order of a spin-orbital model (SOM) in (H,F) phase for  $\lambda \rightarrow 0$  (here  $\lambda = 0.1$ ,  $\alpha = 1$ , and  $\Delta = 0.1$ ). Red symbols: Corresponding order parameters of spin-1 Haldane chain. (b) Magnetization profile in  $S^z = 1$  Kennedy-Tasaki ground state of a spin-1 Haldane chain on  $L = 48$  sites (red symbols) is nearly identical to magnetization profile of  $\langle T_i^z \rangle = \langle S_{2i}^z + S_{2i+1}^z \rangle$  SOM on  $L = 96$  sites (blue symbols) in (H,F) phase for  $\lambda \rightarrow 0$  (here  $\lambda = 0.1$ ,  $\alpha = 1$ , and  $\Delta = 0.1$ ). The inset (green circles) shows the site-resolved magnetization profile of SOM  $\langle S_{2i}^z \rangle \simeq \langle S_{2i+1}^z \rangle \simeq \langle T_i^z \rangle / 2$

$-\langle T_j^z e^{i\pi \sum_{k=j+1}^{j+i-1} T_k^z T_{j+i}^z} \rangle$  are presented in Fig.5.4(a) for both the spin-orbital model on  $L$  sites ( $L = 96$ ) and Haldane chain on  $L/2$  sites. As one can see the coincidence between the results for the Haldane chain and spin-orbital model in the (H,F) state for small  $\lambda$  is excellent.

Finally, the magnetization profile of the spin-orbital model  $\langle \mathbf{S}_{2i} + \mathbf{S}_{2i+1} \rangle$  in one of the ground states of the Kennedy-Tasaki triplet [114, 115] with total  $S^z = 1$  is presented in Fig.5.4(b). On the same plot we superimpose this profile with the corresponding profile of the Haldane chain and again observe the perfect matching between the two.

## 5.5 Full ground state phase diagram

### (a) Analytical estimates

Apart of the above determined exotic ground states for  $\lambda \rightarrow 0$  and the discovered effect of topological order-by-disorder, the bosonic problem studied here turns out to

be relevant for realistic condensed matter systems. To show this we address another limit,  $\lambda \gg 1$ .

We may then decompose  $H = H_0 + V$ , where  $H_0 = -\lambda \sum_i \sigma_i^x + 2(1-\Delta) \sum_i \mathbf{S}_i \mathbf{S}_{i+1}$ , and  $V$  may be treated as a perturbation. To the lowest order in  $1/\lambda$  the system becomes equivalent to a spin  $1/2$   $j_1 - j_2$  chain,

$$\lim_{\lambda \rightarrow \infty} H_S = \sum_i [j_1 \mathbf{S}_i \mathbf{S}_{i+1} + j_2 \mathbf{S}_i \mathbf{S}_{i+2}] \quad (5.5.1)$$

with  $j_1 = 2(\Delta - 1) + (4 - \Delta + \Delta^2)/2\lambda$  and  $j_2 = \lambda^{-1}$ . Higher order terms  $\sim 1/\lambda^2$  involve biquadratic terms in spin operators as well as bilinear interactions beyond second nearest neighbor and present irrelevant deviation from the  $j_1 - j_2$  chain similarly to the fermionic case. Note that the original microscopic model at  $\alpha = 1$  for bosons differs just by an overall sign from the corresponding fermionic expression; however it is not exactly the case for the effective spin models in large  $\lambda$ . From the known ground-state phase diagram of the spin  $1/2$   $j_1 - j_2$  zig-zag chain with  $j_2 > 0$  we map out ground-state phases for our bosonic system in the strong  $\lambda$  limit. For  $\Delta > 1 + 1/\lambda$  the system can be mapped on the  $j_1 - j_2$  zig-zag chain with  $j_1 > 4j_2$  with the gapless ground state of the isotropic Heisenberg chain. Orbital correlations are paramagnetic. We denote this phase by (iH,P). For  $1 - 1/\lambda < \Delta < 1 + 1/\lambda$  the spin sector can be mapped onto the SU(2) symmetric frustrated antiferromagnetic spin  $1/2$  chain with  $0 < j_1 < 4j_2$  with dimerized ground state. The representative state in this phase is realized for  $j_1 = 2j_2$  and is called the Majumdar-Ghosh state [81] that is made of the direct product of singlets involving the nearest spins. Because of the linear coupling between spin dimerization and orbitals present in Hamiltonian Eq. (3),  $\sum_i (\mathbf{S}_i \mathbf{S}_{i+1} - \mathbf{S}_i \mathbf{S}_{i-1}) \sigma_i^z$ , dimerization order in spin variables  $D = \langle \mathbf{S}_i \mathbf{S}_{i+1} - \mathbf{S}_i \mathbf{S}_{i-1} \rangle \neq 0$  is felt as a uniform magnetic field in orbital variables. Hence the occurrence of the dimerization pattern in spin variables will be accompanied by developing ferromagnetic correlations in orbital variables leading to a dimer-ferro phase (D,F).

For  $1 - 3/\lambda < \Delta < 1 - 1/\lambda$  the system can be mapped on the SU(2) symmetric frustrated ferromagnetic spin  $1/2$  chain with  $0 > j_1 > -4j_2$ . Numerical study of the ground state of the frustrated ferromagnetic chain based on the infinite-size

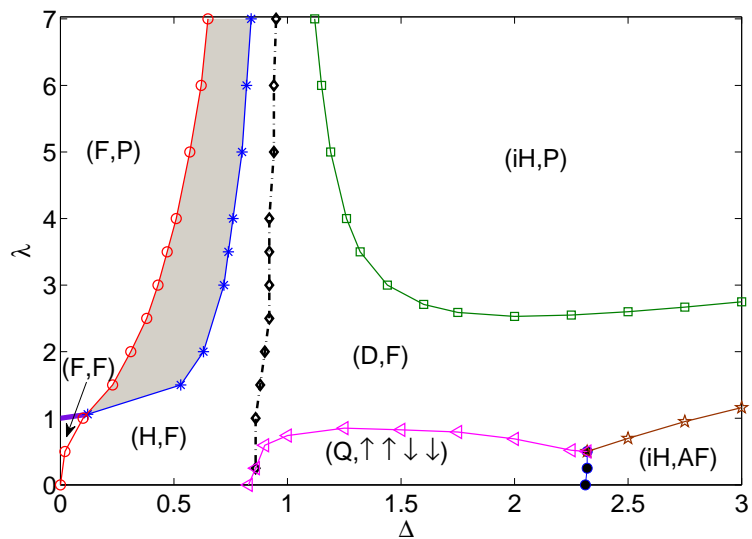


Figure 5.5: Effect of  $\lambda$  on the ground-state phases presented in Fig.5.1 for  $\alpha = 1$ . The dashed line between (H,F) and (D,F) phases represents a boundary phase transition, where edge spins at the end of the open chain disappear in the (D,F) phase. All second-order phase transition lines are obtained with the extrapolation procedure from finite system size data to infinite size.

algorithm suggests that the nearest bonds are characterized by ferro correlations with alternating strengths, and the phase was dubbed the Haldane dimer [85–87].

Finally in spin variables we obtain a fully polarized ferromagnetic state for  $\Delta < 1 - 3/\lambda$ , whereas orbital variables become paramagnetic again (F,P). In numerical part we present the numerical ground-state phase diagram for all values of  $\lambda$  which shows that our bosonic model interpolates smoothly between the Majumdar-Ghosh state of the (D,F) phase realized for  $\lambda \gg 1$  and an exact Haldane state of an effective spin-1 chain realized for  $\lambda \rightarrow 0$ .

### (b) Numerical results

We present the numerical ground-state phase diagram in the full parameter space of  $\Delta$  versus  $\lambda$  in Fig.5.5. The simplest task is to determine the boundary of the fully polarized ferromagnetic state since the total spin of the ground state jumps from the maximal  $S^T = L/2$  value to  $S^T = 0$ . Inside the fully polarized region for the orbital sector we obtain an exactly solvable quantum Ising model in transverse magnetic

field. Hence there is an Ising phase transition with increasing  $\lambda$  between the (F,F) and (F,P) states at  $\lambda = 2 - \alpha + \Delta/2$ . Ising phase transitions are usually captured numerically with studying fidelity susceptibility. For a generic Hamiltonian, with a phase transition driven by the changing strength of coupling constant  $\lambda$ , the fidelity susceptibility  $\chi = \chi_F$  with respect to the "perturbation"  $\lambda$  is defined as Eq.(2.7.5).

We have studied numerically fidelity susceptibility (see chapter 7) inside the fully polarized phase and obtained the phase transition line between (F,F) and (F,P) phases that matches accurately the analytical result. Similarly, between two gapped phases ( $Q, \downarrow\uparrow\downarrow$ ) and (D,F) due to symmetry considerations we expect the Ising phase transition. Scaling of the height of the peak of fidelity susceptibility with system size depicted in Fig.5.6(a) confirms our expectations.

Based on the behavior of order parameters, ground state, and low-energy excited states the phase transition from the (iH,AF) to (D,F) phase seems a smooth second-order transition. On general grounds we expect a Gaussian phase transition, respecting the  $SU(2)$  symmetry of the spin sector, driven by a marginal operator, being marginally irrelevant in the gapless (iH,AF) phase and becoming marginally relevant in the gapped (D,F) phase. Hence scaling of the fidelity susceptibility per site should be sublinear. Surprisingly to us, the scaling of the fidelity susceptibility peak per site with the system size in the vicinity of the phase transition from the (iH,AF) to (D,F) state is also linear as for the Ising case. However, the transition between the gapless (iH,AF) phase and gapped (D,F) phase cannot be of Ising nature. We interpret the linear scaling in the following way: since FS does not capture transition from the (D,F) to (iH,P) state (that is witnessed by singlet-triplet level crossing in the first excited states) from the FS point of view transition from (iH,AF) to (D,F) is similar to the transition from the (iH,AF) directly to the (iH,P) state that would be of Ising nature. Not only the height of the FS peak per site scales linearly with system size but also the position of the peak scales perfectly linearly with the inverse system size.

For open boundary conditions, (D,F) has a unique ground state, whereas (H,F) has a fourfold-degenerate ground state due to the edge spins. Hence these two phases cannot be smoothly connected for the case of open boundary conditions.

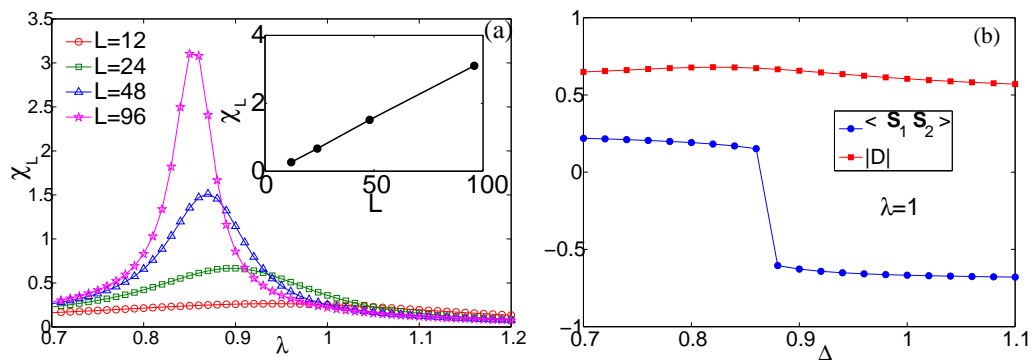


Figure 5.6: Phase transitions: (a) FS with respect to  $\lambda$  per site for  $\Delta = 1.5$ ,  $\alpha = 1$ . Linear scaling of fidelity susceptibility peak per site with system size confirms the Ising nature of the quantum phase transition from the  $(Q, \downarrow\uparrow\uparrow\downarrow)$  to  $(D,F)$  state. (b). Edge spins and dimerized parameter for  $(H,F)$  and  $(D,F)$  states

For periodic boundary conditions the Haldane state is smoothly connected with the  $(D,F)$  state and the ground-state degeneracy is two-fold. Pure spin models which interpolate smoothly between the Haldane state and dimerized state have been studied in Ref. [83, 116, 117] (see Fig.5.6(b)).

For values of  $\lambda = 2$  the topology of the ground-state phase diagram is similar to the fermionic case obtained in the strong  $\lambda$  case, though with reversed sequence of phases with increasing  $\Delta$  ( $\Delta_{Boson} \rightarrow 1/\Delta_{Fermion}$ ), and an identical approach to that did for fermions was performed to determine these phases and boundaries between them. In particular dimerization order vanished at the boundary of the shaded region (indicated by star symbols in Fig.5.5 and then reappears again inside the shaded region. However dimer order is very small adjacent to the  $(F,P)$  state where we cannot exclude the occurrence of other additional phases, though the ground state is a global singlet until reaching the  $(F,P)$  phase. According to our numerical data, in particular due to the very fast growth of the height of peak of fidelity susceptibility, we interpret the phase transition between  $(Q, \downarrow\uparrow\uparrow\downarrow)$  and  $(iH, AF)$  phases as first order.

## 5.6 Conclusion

Dipolar spinor bosons in orbitally degenerate zig-zag lattices develop topological order in extensively degenerate paramagnetic states due to arbitrary weak quan-



---

tum fluctuations of orbitals. This is a direct consequence of the interplay between the orbital frustration and the bosonic nature. Adjacent to the topological state the exact ground state presents spontaneously quadrupoled unit cells for a broad parameter regime of Hund's coupling and the ratio between on-site and long-range interactions. Moreover, by changing the strength of quantum fluctuations of orbitals our model interpolates between the exact ground state of the Haldane chain (realized for  $\lambda \ll 1$ ) and the Majumdar-Ghosh state of the spin 1/2 chain (realized for  $\lambda \gg 1$ ).



# Chapter 6

## Spin-orbit coupled fermions in ladder-like lattices

### 6.1 Introduction

Unidirectional spin-orbit coupling (USOC) resulting from an equal superposition of Rashba [33] and linear Dresselhaus [34] terms has been realized for both spinor Bose [16] and Fermi gases [17,18] with the help of counter-propagating Raman lasers. Recently this technique has allowed for observation of the superfluid Hall effect [119], Zitterbewegung [120], and the spin-Hall effect in a quantum gas [121]. Several theoretical works have discussed the creation of pure Rashba or Dresselhaus spin-orbit coupling (SOC) by optical [122] and magnetic means [123] and even proposed methods to generate three-dimensional (3D) SOC [124].

The presence of synthetic SOC is expected to lead to rich physics for atoms loaded in optical lattices. For 2D Hubbard models at half filling the effects of Rashba-like SOC were studied both for two-component bosons and fermions, for which exotic spin textures in the ground state such as coplanar spiral waves and stripes as well as noncoplanar vortex/antivortex configurations have been predicted [125–127]. Note, however, that the SOC introduces frustration, invalidating quantum Monte Carlo approaches, and hence most studies have relied on classical MC calculations.

In this chapter we analyze the effects of SOC in a two-component Fermi gas loaded in an optical lattice in the Mott-insulator regime. Since we are interested in

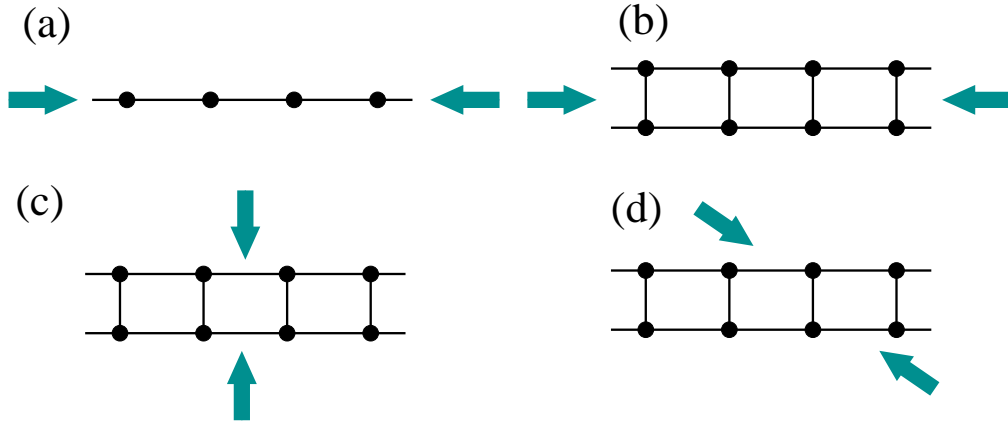


Figure 6.1: Different orientations of lasers: (a). Raman lasers counter-propagating along 1D ladder, (b). Raman lasers counter-propagating along the ladder legs, (c). Raman lasers counter-propagating along the ladder rungs, (d). Raman lasers counter-propagating along both the ladder legs and the ladder rungs.

the quantum spin-1/2 phases in the presence of SOC, we cannot rely on classical Monte Carlo and, hence, must employ exact diagonalization or DMRG techniques. We employ DMRG in this chapter, restricting our analysis to the minimal system where the non-Abelian character of the vector potential may be manifested, allowing nontrivial effects of SOC without the need to break the time-reversal invariance, namely, a two-leg ladderlike optical lattice, which may be created by incoherently combining a 1D lattice and a two-well potential. Different orientations of lasers are shown in Fig.6.1

## 6.2 Effective spin models for fermions

Recent experiments have realized USOC characterized by a Hamiltonian of the form [16–18]

$$H_{USOC} = \frac{1}{2m}(\mathbf{p}\sigma^0 - \mathbf{A})^2 - \frac{\hbar}{2}\sigma^x + \frac{\delta}{2}\sigma^z \quad (6.2.1)$$

where  $\sigma^x, \sigma^z$  are Pauli matrices,  $\sigma^0$  is the identity matrix, and the effective vector potential for counter-propagating Raman lasers on the  $xy$  plane is given by  $A = -\hbar\mathbf{k}_0\sigma^z$ , with  $\mathbf{k}_0 = (k_0^x, k_0^y, 0)$ . Here the eigenvectors of  $\sigma^z$  correspond to atomic hyperfine components, the term  $\frac{\delta}{2}\sigma^z$  is due to detuning from resonance, and  $\hbar$  is

the Rabi coupling. Crucially,  $\mathbf{A}$  cannot be completely gauged out, since it does not commute with the scalar potential  $\Phi = -\frac{\hbar}{2}\sigma^x + \frac{\delta}{2}\sigma^z$ .

Let us rewrite the Hamiltonian 6.2.1 for a 1D system in terms of the gauge field  $\mathbf{A} = (-\hbar k_0 \sigma^x, 0, 0)$  with the Peierls substitution (see Appendix B for details),

$$H = \sum_{j,\alpha,\beta} (-t e^{-ik_0 a \sigma^x} c_{j,\alpha}^\dagger c_{j+1,\beta} + h.c.) + U \sum_j n_{j\uparrow} n_{j\downarrow} - \frac{\hbar}{2} \sum_j c_j^\dagger \sigma^x c_j + \frac{\delta}{2} \sum_j c_j^\dagger \sigma^z c_j \quad (6.2.2)$$

Using the transformation

$$\begin{pmatrix} c_{j,\uparrow} \\ c_{j,\downarrow} \end{pmatrix} = e^{-ik_0 a j \sigma^x} \begin{pmatrix} \tilde{c}_{j,\uparrow} \\ \tilde{c}_{j,\downarrow} \end{pmatrix} \quad (6.2.3)$$

the Hamiltonian becomes,

$$H = \sum_j (-t \tilde{c}_j^\dagger \tilde{c}_{j+1} + h.c.) + U \sum_j \tilde{n}_{j\uparrow} \tilde{n}_{j\downarrow} - \hbar \sum_j \tilde{S}_j^x + \delta \sum_j (\cos(2k_0 a j) \tilde{S}_j^z + \sin(2k_0 a j) \tilde{S}_j^y) \quad (6.2.4)$$

Now we return to the standard Hubbard model. According to Eq.(2.6.26), the effective model for fermions in new variables  $\tilde{\mathbf{S}}_j$  is

$$H = \frac{4t^2}{U} \sum_j \tilde{\mathbf{S}}_j \tilde{\mathbf{S}}_{j+1} - \hbar \sum_j \tilde{S}_j^x + \delta \sum_j (\cos(2k_0 a j) \tilde{S}_j^z + \sin(2k_0 a j) \tilde{S}_j^y) \quad (6.2.5)$$

Because the unitary transformation does not change the physics of the system, we may easily know the phases in these new variables. For instance, if there are no Zeeman fields  $h = 0$ ,  $\delta = 0$ , one recovers the standard Heisenberg model with Luttinger liquid as its ground state. If  $h = 0$ ,  $k_0 a = \pi/2$ , one retrieves the Heisenberg model with a staggered field. From the definition of spin operator  $\tilde{\mathbf{S}}_j = (\tilde{c}_{j\uparrow}^\dagger, \tilde{c}_{j\downarrow}^\dagger) \frac{\boldsymbol{\sigma}}{2} \begin{pmatrix} \tilde{c}_{j,\uparrow} \\ \tilde{c}_{j,\downarrow} \end{pmatrix}$ , and the transformation Eq.(6.2.3), we have the following relations between  $\tilde{\mathbf{S}}_j$  and  $\mathbf{S}_j$ ,

$$\tilde{S}_j^x = S_j^x \quad (6.2.6)$$

$$\tilde{S}_j^y = \cos(2k_0 a j) S_j^y + \sin(2k_0 a j) S_j^z \quad (6.2.7)$$

$$\tilde{S}_j^z = \cos(2k_0 a j) S_j^z - \sin(2k_0 a j) S_j^y \quad (6.2.8)$$

Transforming back to the original variables  $\mathbf{S}_j$ , the effective model is

$$H_{eff} = \frac{4t^2}{U} \sum_j [\cos(2k_0a)\mathbf{S}_j\mathbf{S}_{j+1} + 2\sin^2(k_0a)S_j^x S_{j+1}^x + \sin(2k_0a)[\mathbf{S}_j \times \mathbf{S}_{j+1}]^x] - h \sum_j S_j^x + \delta \sum_j S_j^z \quad (6.2.9)$$

Similarly, we may obtain the effective Hamiltonian with spin-orbit coupling for 2D for the gauge field  $\mathbf{A} = (-\hbar k_0^x \sigma^x, -\hbar k_0^y \sigma^y, 0)$ ,

$$H_{eff} = \frac{4t^2}{U} \sum_j [\cos(2k_0^x a)\mathbf{S}_j\mathbf{S}_{j+\mathbf{e}_x} + 2\sin^2(k_0^x a)S_j^x S_{j+\mathbf{e}_x}^x + \sin(2k_0^x a)[\mathbf{S}_j \times \mathbf{S}_{j+\mathbf{e}_x}]^x] + \frac{4t^2}{U} \sum_j [\cos(2k_0^y a)\mathbf{S}_j\mathbf{S}_{j+\mathbf{e}_y} + 2\sin^2(k_0^y a)S_j^y S_{j+\mathbf{e}_y}^y + \sin(2k_0^y a)[\mathbf{S}_j \times \mathbf{S}_{j+\mathbf{e}_y}]^y] - h \sum_j S_j^x + \delta \sum_j S_j^z \quad (6.2.10)$$

where, the vector product of two nearest neighbouring spins is called Dzyaloshinskii-Moriya term.

If we consider a two-component Fermi gas loaded in a ladder-like optical lattice of intersite spacing  $a$ , with the ladder legs oriented along  $x$  and the rungs along  $y$ , and a gauge field  $\mathbf{A} = (-\hbar k_0^x \sigma^z, -\hbar k_0^y \sigma^z, 0)$  the effective model for two-component fermions is given by

$$H_{eff} = J_{\perp} \sum_j \{\cos(2k_0^y a)\mathbf{S}_{1,j}\mathbf{S}_{2,j} + 2\sin^2(k_0^y a)S_{1,j}^z S_{2,j}^z + \sin(2k_0^y a)[\mathbf{S}_{1,j} \times \mathbf{S}_{2,j}]^z\} + J_{\parallel} \sum_{\alpha,j} \{\cos(2k_0^x a)\mathbf{S}_{\alpha,j}\mathbf{S}_{\alpha,j+1} + 2\sin^2(k_0^x a)S_{\alpha,j}^z S_{\alpha,j+1}^z + \sin(2k_0^x a)[\mathbf{S}_{\alpha,j} \times \mathbf{S}_{\alpha,j+1}]^z\} - h \sum_{\alpha,j} S_{\alpha,j}^x + \delta \sum_{\alpha,j} S_{\alpha,j}^z \quad (6.2.11)$$

where  $J_{\parallel} = 4t_x^2/U$ ,  $J_{\perp} = 4t_y^2/U$ .  $j$  is the rung index and  $\alpha = 1, 2$  denote the up leg and down leg.

## 6.3 USOC for decoupled chains

### (a) Repulsive interactions

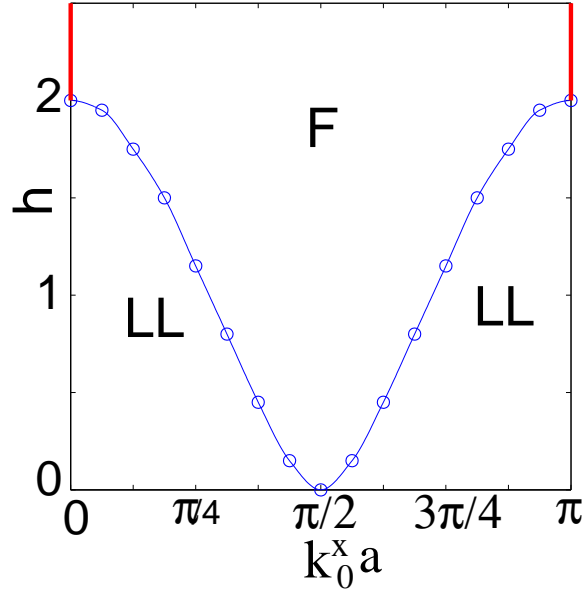


Figure 6.2: Ground states of a 1D spin-1/2 chain with USOC and a transverse magnetic field obtained using DMRG for 96 sites. The magnetic field is in units of  $J_{\parallel}$ . LL, Luttinger liquid phase; F, ferromagnetic state.

We first discuss the case of decoupled chains (see Fig.6.1(a)),  $J_{\perp} = 0$  (i.e.,  $t_y = 0$ ) and  $\delta = 0$ , which results in the 1D Hamiltonian

$$H_{eff} = J_{\parallel} \sum_j \{ \cos(2k_0^x a) \mathbf{S}_j \mathbf{S}_{j+1} + 2 \sin^2(k_0^x a) S_j^z S_{j+1}^z + \sin(2k_0^x a) [\mathbf{S}_j \times \mathbf{S}_{j+1}]^z \} - h \sum_j S_j^x \quad (6.3.1)$$

For  $k_0^x = 0$ , Eq.(6.3.1) describes an SU(2)-symmetric spin-1/2 antiferromagnetic chain in an external magnetic field, which is exactly solvable by means of the Bethe ansatz [128]. The ground state is a gapless Luttinger liquid (LL) for  $h < 2J_{\parallel}$ , and a fully polarized state for  $h > 2J_{\parallel}$ . These two phases are separated by a commensurate-incommensurate (C-IC) phase transition.

In order to discuss the effects of USOC it is convenient to introduce a gauge transformation that renders exchange interactions explicitly SU(2) invariant,  $H_{1D} \rightarrow U H_{1D} U^{\dagger} = \tilde{H}_{1D}$ , where  $U = \prod_j e^{-2ik_0^x a j S_j^z}$  as we did before, the Hamiltonian becomes

$$\tilde{H}_{1D} = J_{\parallel} \sum_j \tilde{\mathbf{S}}_j \tilde{\mathbf{S}}_{j+1} - \sum_j \mathbf{h}_j(\mathbf{k}_0) \tilde{\mathbf{S}}_j \quad (6.3.2)$$

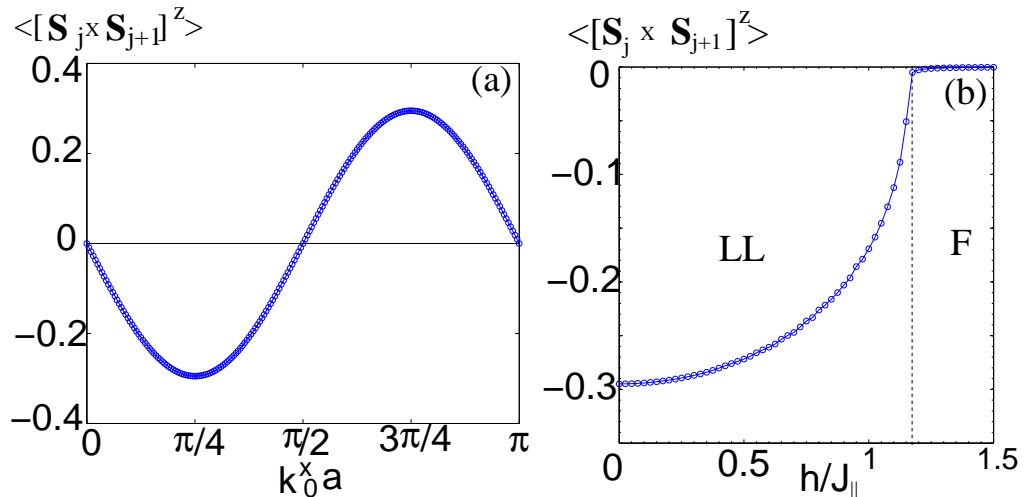


Figure 6.3: Expectation value of the vector product of two neighboring spins obtained by DMRG simulations for 96 sites as a function of (a) the USOC parameter,  $k_x a$ , for  $h = 0$  and (b) the magnetic field for  $k_x a = \pi/4$ .

where the effect of the USOC is entirely absorbed into an external magnetic field,  $\mathbf{h}_j(\mathbf{k}_0) = h(\cos(2k_0^x a j), \sin(2k_0^x a j), 0)$ , which spirals on the  $xy$  plane.

For  $k_0^x a = \pi/2$ ,  $\mathbf{h}_j(\mathbf{k}_0) = (-1)^j h \mathbf{e}_x$ , i.e., a staggered effective magnetic field. A staggered field constitutes a relevant perturbation (in the renormalization-group sense) as it couples to the Néel order, which is one of the leading instabilities in a 1D antiferromagnetic chain. As a result of this, a gap in the excitation spectrum,  $\Delta E \sim h^{2/3}$ , opens for any arbitrary coupling  $h$ . The low-energy behavior is described by a massive sine-Gordon model where one of the breather modes is degenerate with soliton and antisoliton excitations [129]. In the gauge-transformed variables the ground state develops Néel order, which, after undoing the gauge transformation, results for the original spin operators in an uniformly magnetized state, i.e., a ferromagnetic (F) state, although magnetization is never fully saturated for  $k_0^x a \neq 0$ .

For  $0 < k_0^x a < \pi/2$ ,  $\mathbf{h}_j(\mathbf{k}_0)$  is IC and hence the gapless LL phase survives up to a finite  $h$  value at which the F phase is reached. We have employed the matrix product formulation of the DMRG method to obtain numerically the phase diagram for arbitrary values of the USOC (see Fig.6.2). This phase diagram confirms the existence of a gapless LL and a gapped F phase separated by a C-IC transition. Note that



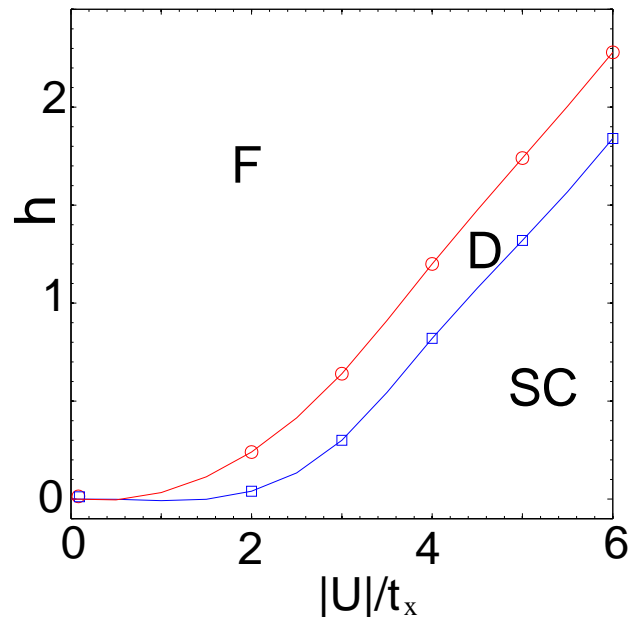


Figure 6.4: Phase diagram for an attractive two-component Fermi-Hubbard model on a chain at half filling with maximal USOC. D, dimerized phase; SC, 1D superconductor. The magnetic field is in units of  $t_x$ . Phase boundaries are obtained after finite-size extrapolation from data obtained for  $L=128, 256, 512,$  and  $1024$  sites.

correlation functions, which decay algebraically in the LL phase and exponentially in the F phase, are generically incommensurate due to the Dzyaloshinskii-Moriya anisotropy, and the vector product of two neighboring spins has finite expectation value  $\langle [\mathbf{S}_j \times \mathbf{S}_{j+1}]^z \rangle \sim -\sin(2k_0^x a)$  as depicted in Fig.6.3(a). Its magnetic-field dependence is presented in Fig.6.3(b). We note that  $\langle [\mathbf{S}_j \times \mathbf{S}_{j+1}]^z \rangle$  serves as an order parameter that is nonzero in the LL phase and vanishes rapidly in the F phase, showing cusplike behavior at the C-IC phase transition indicated by the dashed line in Fig.6.3(b).

### (b) Attractive interactions

For decoupled chains we have also studied the case of two-component fermions with attractive interactions. The most interesting ground-state physics occurs at half filling in the vicinity of the maximal USOC,  $k_0^x a = \pi/2$ . In this case, after particle-hole transformation the 1D Fermi-Hubbard model becomes dual to the repulsive ionic-Hubbard model [130–132], being characterized by the existence of a

dimerized (D) phase between a superconducting phase and the F state. With increasing magnetic field the superconducting phase undergoes a BKT transition into the D state, where translational symmetry is spontaneously broken. Further increasing the magnetic field results in a D-F Ising transition. We characterized the D phase in our numerical simulations by means of the dimerization order parameter, which, in a chain with  $L$  sites, is defined as

$$D = \sum_j \frac{(-1)^j}{L} \langle c_{j,\uparrow}^\dagger c_{j+1,\downarrow} - c_{j,\downarrow}^\dagger c_{j+1,\uparrow} \rangle. \quad (6.3.3)$$

The phase diagram of the 1D attractive Fermi-Hubbard model with  $k_0^x a = \pi/2$  at half filling is presented in Fig.6.4.

## 6.4 USOC along the ladder rungs

We analyze first the case of an USOC along the ladder rungs (see Fig.6.1(c)), i.e.,  $k_0^x = 0$  in Eq.(6.2.11). For  $k_0^y = 0$  the magnetic field introduces two C-IC phase transitions: from a rung-singlet (RS) into an LL and then from the LL into the fully polarized F state. As shown before, it is convenient to introduce the gauge transformation,

$$\tilde{S}_{\alpha,j}^x = \cos(2k_0^y a \alpha) S_{\alpha,j}^x - \sin(2k_0^y a \alpha) S_{\alpha,j}^y \quad (6.4.1)$$

$$\tilde{S}_{\alpha,j}^y = \cos(2k_0^y a \alpha) S_{\alpha,j}^y - \sin(2k_0^y a \alpha) S_{\alpha,j}^x \quad (6.4.2)$$

$$\tilde{S}_{\alpha,j}^z = S_{\alpha,j}^z \quad (6.4.3)$$

For the case of the maximal USOC,  $k_0^y a = \pi/2$ , the gauge-transformed Hamiltonian becomes

$$\tilde{H} = J_{\parallel} \sum_{\alpha=(1,2),j} \tilde{\mathbf{S}}_{\alpha,j} \tilde{\mathbf{S}}_{\alpha,j+1} + J_{\perp} \sum_j \tilde{\mathbf{S}}_{1,j} \tilde{\mathbf{S}}_{2,j} - h \sum_{\alpha=(1,2),j} (-1)^\alpha \tilde{S}_{\alpha,j}^x \quad (6.4.4)$$

In the strong-rung-coupling limit,  $J_{\perp} \gg J_{\parallel}$ , the ground state becomes a rung-product state of the form

$$|\tilde{RS}\rangle = \prod_j (|\tilde{\uparrow}_{1,j}\rangle \otimes |\tilde{\downarrow}_{2,j}\rangle - |\tilde{\downarrow}_{1,j}\rangle \otimes |\tilde{\uparrow}_{2,j}\rangle) / \sqrt{1 + \beta^2} \quad (6.4.5)$$

where  $\{\tilde{\uparrow}, \tilde{\downarrow}\}$  refer to the eigenstates of  $\tilde{S}^x$ . For  $h = 0, \beta = 1$  and the ground state is a product state of singlets along the rungs. With increasing magnetic field,  $\beta$  decreases, gradually tending to 0. For  $\beta = 0$  the ground state after undoing the gauge transformation translates into the F state. Hence, for  $k_0^y a = \pi/2$  the magnetic field just results in an adiabatic evolution of  $|\tilde{RS}\rangle$  into the F state.

To address the general case  $0 < k_0^y a < \pi/2$  we consider the case of weak USOC,  $k_0^y a \ll 1$ , closely following the strong- rung-coupling derivation in Ref. [133]. For  $h = 0$  the ground state is well approximated by a direct product of singlets along the rungs, and the energy gap to the lowest rung triplet excitation is  $\sim J_\perp$ . The external magnetic field splits the rung triplet excitations linearly, and the energy of the state where both spins of the rung point in the direction of the field approaches that of the RS state for  $h \sim J_\perp$ . Identifying the RS state on a rung with an effective spin-1/2 pointing down, and the  $S^x = 1$  component of the rung triplet state with the spin-1/2 pointing up, the effective pseudo-spin-1/2 model in the strong-rung coupling limit for  $h \sim J_\perp$  takes the form of an XXZ model in a tilted uniform magnetic field,

$$H_\tau = J_\parallel \sum_j \left( \frac{1}{2} \tau_j^x \tau_{j+1}^x + \tau_j^y \tau_{j+1}^y + \tau_j^z \tau_{j+1}^z \right) - h_x \sum_j \tau_j^x - h_y \sum_j \tau_j^y \quad (6.4.6)$$

where  $\tau^{x,y,z}$  are the pseudo-spin-1/2 operators,  $h_x = h - J_\perp \cos(2k_0^y a) + J_\perp (1 - \cos(2k_0^y a))/4 - J_\parallel/2$  and  $h_y = J_\perp \sin(2k_0^y a)/\sqrt{2}$ . With varying  $h_x$  model Eq.(6.4.6) undergoes changes in three ground-state phases [134–136]: two F phases separated by Ising transitions from an intermediate Néel phase in the  $\tau^z$  state. One of the F phases of the effective model, Eq.(6.4.6), translates to the RS phase of the ladder, whereas the Néel phase and the second F phase of Eq.(6.4.6) translate into identical ladder phases. Note that it is the Dzyaloshinskii-Moriya interaction that, in the leading order, breaks in Eq.(6.4.6) the U(1) rotation symmetry in the  $yz$  plane allowing for the Néel ordering.

We recall that for  $k_0^y a = \pi/2$  a growing magnetic field does not introduce any phase transition but rather adiabatically connects RS and F phases. Since in the vicinity of  $k_0^y a = 0$  an intermediate Néel phase occurs, we expect, as a function of  $k_0^y a$  and  $h$ , the presence of a Néel island inside an overall RS-F state. Our numerical results confirm this expectation, as depicted in Fig.6.5. Since Néel order

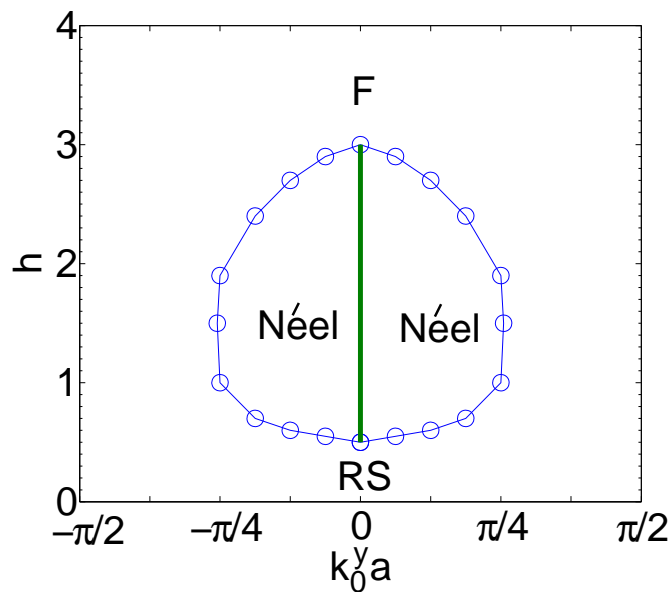


Figure 6.5: Phase diagram for USOC along ladder rungs. The phase transition curve into the Néel state is determined from the closing of the gap between the two lowest eigenstates; For  $k_0^y a = 0$  an LL line is realized between the RS and the F phases. The magnetic field is in units of  $J_{\parallel} = J_{\perp}$ .

is spontaneous, in our numerical calculations we monitor

$$n^2 \equiv \lim_{|i-j| \gg 1} |(-1)^{i-j} \langle S_{\alpha,i}^z S_{\alpha,j}^z \rangle| \quad (6.4.7)$$

The magnetic-field dependence of  $n^2$  is illustrated in Fig.6.6(a).

We have also studied the behavior of the excitation gap. The Néel state is characterized by a doubly degenerate ground state in the thermodynamic limit, whereas the RS and F states have unique gapped ground states. Hence a simple way to obtain the boundary of the Néel state is to follow the closing of the gap between the ground state and the first excited state (that becomes degenerate with the ground state in the thermodynamic limit in the Néel phase). We plot the behavior of the gap in Fig.6.6(b). The gaps close linearly with the magnetic field when approaching the quantum phase transition points, as expected from the Ising character.

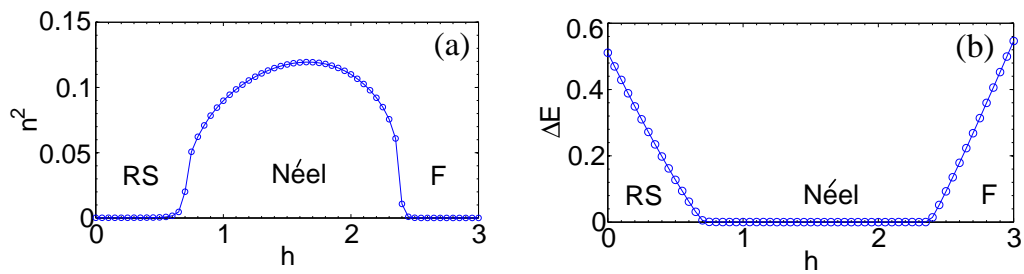


Figure 6.6: (a) Square Néel order as a function of the magnetic field along a cut through the RS-Néel-F phases for  $k_0^x a = 0$  and  $k_0^y a = \pm 3\pi/16$ . (b) Behavior of the energy gap between the two lowest eigenstates as a function of the magnetic field across the RS-Néel-F phases. The Néel state is characterized by doubly degenerate ground states. The magnetic field and the gap are both measured in units of  $J_{\parallel} = J_{\perp}$ .

## 6.5 USOC along the ladder legs

We consider that the USOC is oriented along the ladder legs (see Fig.6.1(b)), and hence  $k_0^y a = 0$  in Eq.(6.2.11). For  $k_0^x a = 0$ , the external magnetic field induces two consecutive C-IC phase transitions: the first from the RS into the gapless LL phase and the second from the LL into the fully polarized F state. For  $k_0^x a \neq 0$  we may perform a gauge transformation similar to those discussed above, which, for the maximal USOC,  $k_0^x a = \pi/2$ , results in a model similar to Eq.(6.4.6), but in this case with a field that couples uniformly to spins belonging to the same rung and alternates from rung to rung,  $-h \sum_{\alpha,j} (-1)^j \tilde{S}_{\alpha,j}^x$ . Using bosonization in the weak-rung-coupling limit,  $J_{\perp} \ll J_{\parallel}$ , and in the opposite limit,  $J_{\perp} \gg J_{\parallel}$ , employing strong-rung-coupling expansion it has been determined that such a magnetic field introduces Gaussian criticality between two gapped phases of the antiferromagnetic spin ladder [137], which, for our original spin variables, corresponds to the RS and F states.

The difference at maximal USOC between the case with USOC along the ladder legs and that with USOC along the rungs can be easily understood in the limit  $J_{\perp} \gg J_{\parallel}$ . For the case of USOC along the ladder legs the magnetic field couples uniformly to the spins on the same rung, and hence it favors a triplet state on each rung, with both spins pointing in the same direction, which alternates from one

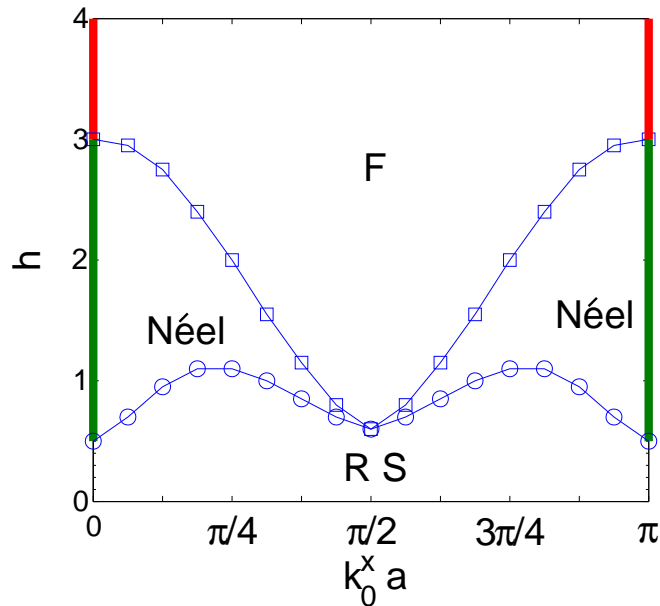


Figure 6.7: Phase diagram for USOC along ladder rungs. The phase transition curve into the Néel state is determined from the closing of the gap between the two lowest eigenstates; For  $k_0^y a = 0$  an LL line is realized between the RS and the F phases. The magnetic field is in units of  $J_{\parallel} = J_{\perp}$ .

rung to the next. This state is orthogonal to the RS configuration. In contrast, in Eq.(6.4.6) the magnetic field couples in a staggered way to the spins in the same rung, and the ground state favored by a strong magnetic field is not orthogonal to the RS state. As a result, for the USOC along rungs the RS state can be adiabatically connected to the F state, whereas for the USOC along legs this is not possible.

The ground-state phase diagram for USOC along the ladder legs is depicted in Fig.6.7. The ground states and phase transitions will be similar to the previous case of USOC along the rungs. Thus C-IC phase transition points (corresponding to U(1) symmetry at  $k_0^x a = 0$ ) evolve into Ising lines for  $0 < k_0^x a < \pi/2$ , and at  $k_0^x a = \pi/2$  these two Ising lines merge in a Gaussian criticality due to the enhanced symmetry (where U(1) symmetry is revived).

Our numerical results for  $n^2$  and the excitation gap from DMRG are depicted in Fig.6.8. Note that finite-size effects are more pronounced at the RS-to-Néel transition, whereas for the Néel-to-F transition finite-size effects are negligible. For the RS-to-Néel transition we have carefully performed finite-size scaling of the order

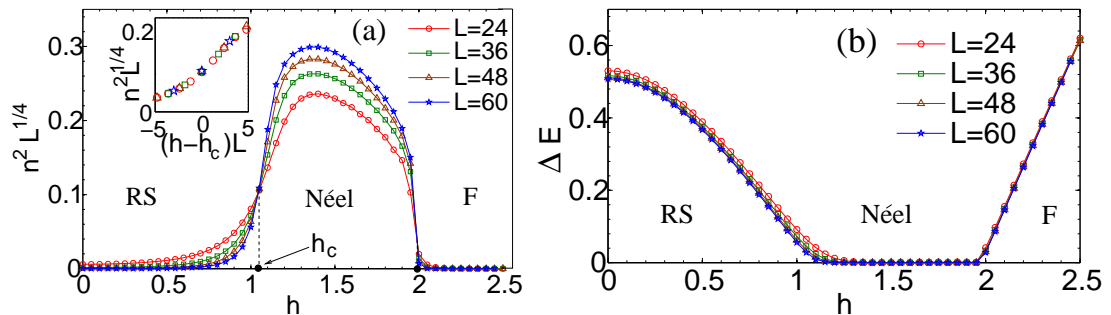


Figure 6.8: (a) Square Néel order,  $n^2$ , as a function of the magnetic field along a cut through the RS-Néel-F phases for  $k_0^x a = \pi/4$  and  $k_0^y a = 0$  and for different system sizes. Inset: Collapse of our numerical results for different system sizes on a single curve according to the Ising scaling. (b) Behavior of the energy gap between the two lowest eigenstates as a function of the magnetic field across the RS-Néel-F phases.

parameter and determined the critical field  $h_c$  corresponding to the phase transition from the intersection of the order parameter curves for different system sizes. The collapse of the order parameter for different system sizes in the vicinity of  $h_c$  on the single curve according to the Ising law is depicted in the inset in Fig.6.8(a).

## 6.6 Two-leg ladder with a non-Abelian vector potential

We consider at this point a non-Abelian vector potential of the form  $A = (-\hbar k_0^x \sigma^x, -\hbar k_0^y \sigma^y, 0)$  (see Fig.6.1(d)). Contrary to the case of USOC, the magnetic field,  $h$ , is not necessary to ensure the nontrivial character of SOC. We hence consider the time reversal symmetric case,  $h = 0$ , and a balanced mixture of up and down spin fermions. Effects of a magnetic field in a quarter filled Fermi Hubbard model with Rashba interaction was studied in Ref. [138]. The effective spin model in this

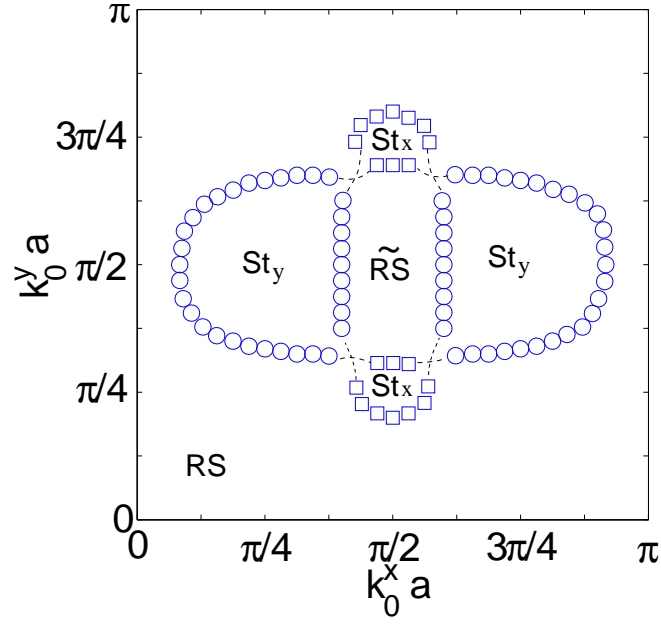


Figure 6.9: Ground states for a spin ladder with Rashba SOC. Numerical results correspond to DMRG calculations for  $L = 48$  rungs.

case acquires the form

$$\begin{aligned}
H_{eff} = & J_{\perp} \sum_j \{ \cos(2k_0^y a) \mathbf{S}_{1,j} \mathbf{S}_{2,j} + 2 \sin^2(k_0^y a) S_{1,j}^y S_{2,j}^y + \sin(2k_0^y a) [\mathbf{S}_{1,j} \times \mathbf{S}_{2,j}]^y \} \\
& + J_{\parallel} \sum_{\alpha,j} \{ \cos(2k_0^x a) \mathbf{S}_{\alpha,j} \mathbf{S}_{\alpha,j+1} + 2 \sin^2(k_0^x a) S_{\alpha,j}^x S_{\alpha,j+1}^x \\
& + \sin(2k_0^x a) [\mathbf{S}_{\alpha,j} \times \mathbf{S}_{\alpha,j+1}]^x \}
\end{aligned} \tag{6.6.1}$$

Our numerical results for the ground-state phase diagram are presented in Fig.6.9. In the vicinity of zero SOC,  $k_0^x a = k_0^y a = 0$ , the system is in the RS state. For the case of maximal SOC,  $k_0^x a = k_0^y a = \pi/2$ , we may employ the canonical transformation  $\mathbf{S}_{\alpha,i} \rightarrow \tilde{\mathbf{S}}_{\alpha,i} = U \mathbf{S}_{\alpha,i} U^\dagger$ , with

$$U = \prod_j e^{-i\pi S_{1,j}^y} \prod_{\alpha,k=2j} e^{-i\pi S_{\alpha,k}^x} \tag{6.6.2}$$

which transforms Hamiltonian (6.6.1) into an  $SU(2)$  symmetric antiferromagnetic spin ladder Hamiltonian of the form of Eq. (6.4.4) with  $h = 0$ .

Thus for  $k_0^x a = k_0^y a = \pi/2$  the system is in the RS phase but in the gauge-transformed spins (hence we denote it  $\tilde{RS}$ ), with no long-range order and exponentially decaying correlation functions. In the strong rung coupling limit the ground



state in gauge transformed variables is the RS product state Eq.(6.4.5) with  $\beta = 1$ , that for original variables transforms via  $U$  to the direct product of  $S^z = 0$  components of the rung triplets, also of the form of Eq.(6.4.5), but with  $\beta = -1$ . Since the  $\widetilde{RS}$  state is gapped it will occupy a finite region around the  $k_0^x a = k_0^y a = \pi/2$  point.

In the RS phase the vector product of two neighboring spins has finite expectation value: along the chains  $\langle [\mathbf{S}_{\alpha,j} \times \mathbf{S}_{\alpha,j+1}]^x \rangle \sim \sin(2k_0^x a)$ , and along the rungs  $\langle [\mathbf{S}_{1,j} \times \mathbf{S}_{2,j}]^y \rangle \sim \sin(2k_0^y a)$ . In the  $\widetilde{RS}$  phase the vector product of two neighboring spins is negligibly small.

Our numerical results also reveal the appearance of striped phases with long-range order where spins are ferromagnetically ordered in one direction and antiferromagnetically in the other. The case of F order along the rung ( $St_y$  phase) is best understood in the vicinity of the  $(k_0^x a, k_0^y a) = (\pi/4, \pi/2)$  point, where  $\cos(2k_0^x a) = 0$ , and  $\cos(2k_0^y a) = -1$ . For these parameters the coupling along the rung  $S_{1,j}^x S_{2,j}^x$  is F, whereas the intra-leg coupling  $S_{\alpha,j}^x S_{\alpha,j+1}^x$  is antiferromagnetic, which results in the  $St_y$  configuration observed in our numerical calculations (Fig.6.9).

We may understand in a similar way the appearance of the  $St_x$  phase (see Fig.6.9), analyzing the behavior in the vicinity of  $(k_0^x a, k_0^y a) = (\pi/2, \pi/4)$ , which is characterized by an F  $S_{\alpha,j}^y S_{\alpha,j+1}^y$  coupling along legs and an antiferromagnetic  $S_{1,j}^y S_{2,j}^y$  exchange along rungs. The  $St_x$  and  $St_y$  states are dual to each other with respect to the interchange of leg and rung directions and  $S^x$  and  $S^y$  components. Our numerical simulations suggest that, similarly to the USOC case, all phase transitions for the case of the non-Abelian vector potential are of second-order Ising nature. This is natural, since the system does not enjoy, in general, any continuous symmetry, and striped phases break spontaneously discrete  $Z^2$  symmetries:  $St_y$  breaks translation symmetry along the chains direction, whereas  $St_x$  breaks the parity symmetry associated with the exchange of ladder legs. Both striped phases also break time-reversal symmetry.

The RS and  $\widetilde{RS}$  phases present different parity symmetry for an odd number of rungs, where the RS phase is antisymmetric and the  $\widetilde{RS}$  is symmetric; as a result, these two phases can not be connected adiabatically with each other. We

could not determine numerically whether the RS and  $\widetilde{RS}$  states can be connected adiabatically for an even number of rungs in the parameter space  $(k_0^x a, k_0^y a)$  in Fig.6.9. In particular, the string order, defined for the pair of spins across the ladder diagonal, is finite for both the RS and the  $\widetilde{RS}$  states and vanishes in the striped phases. However, in the thermodynamic limit we expect the behaviors of odd and even numbers of rungs to converge, and hence it is most likely that in the model given in Eq.(6.6.1) the RS and  $\widetilde{RS}$  states are always separated by a phase transition (indicated by dashed lines in Fig.6.9).

## 6.7 Experimental realizations

Spin-orbit coupled Fermi gases are realized in Ref. [17] and Ref. [18]. Potassium  $^{40}\text{K}$  (Kalium 40), that has 19 protons, 21 neutrons and 19 electrons, hence is a fermionic atom. Ground state configuration has:  $1s^2 2s^2 p^6 3s^2 p^6 4s^1$  with the quantum numbers of total electron spin  $S = 1/2$ , total electron orbital moment  $L = 0$ . The hyperfine interaction  $\sim \mathbf{I}(\mathbf{S} + \mathbf{L})$  splits the ground state manifold. Total nuclear spin  $I = 4$ , thus  $F = 4 \pm 1/2$  manifolds are split by hyperfine interaction. (see Fig.6.10) Take hyperfine sublevels of  $^{40}\text{K}$ , split by magnetic field applied in  $z$  direction  $|\uparrow\rangle = |9/2, 9/2\rangle$  and  $|\downarrow\rangle = |9/2, 7/2\rangle$  (see Fig.6.10). Energy difference between these states  $\epsilon_1$  is due to Zeeman shift. Two Raman laser beams counterpropagate along  $\vec{e}_x$  and are linearly polarized along  $\vec{e}_y$  and  $\vec{e}_z$  that translate into  $\pi$  and  $\sigma^+$  polarizations along  $\vec{e}_z$  axes. Frequencies of these two lasers are such, that by stimulated absorption of a photon from one laser and stimulated emission of the photon into another laser  $|\downarrow\rangle$  swaps into  $|\uparrow\rangle$  and vice versa,  $\hbar(\omega_1 - \omega_2) = \epsilon_1$ . Wavevectors are  $|k_i| = 2\pi/\lambda_i = \omega_i/c$ , and have only  $x$  components:  $k_1^x = k_0 + \delta k$ ,  $k_2^x = -k_0 + \delta k$ . When absorbing one photon and stimulatingly emitting another, an atom gets kick of momentum  $2\hbar|k_0|$  in  $x$  direction. The recoil momentum (momentum obtained by atom when interacting with a single photon) is  $\simeq \hbar k_0$ , since  $\delta k \ll k_0$ .

During atom-photon interaction (absorption and emission) energy, momentum and  $z$  component of angular momentum of atom + photon system is conserved. Polarization of photons are such that during transition from  $|\uparrow\rangle$  to electronically

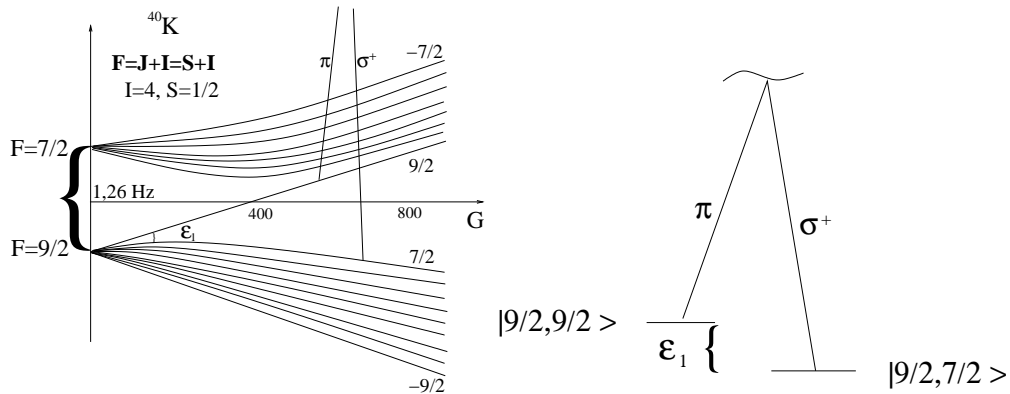


Figure 6.10: Hyperfine structure of  $^{40}\text{K}$  and stimulated 2 photon Raman optical pumping scheme of USOC.

excited state (by absorbing  $\pi$  polarized photon with respect to  $z$  axes. Magnetic moment projection on  $z$  axes of  $\pi$  polarized photon is zero) magnetic quantum number of atom  $m_F$  does not change. However during stimulated emission of  $\sigma^+$  polarized photon (photon with  $\sigma^+$  polarization with respect to  $z$  axes carries magnetic moment  $+\hbar$ ) when jumping from excited state to  $|\downarrow\rangle$  state, the  $m_F \rightarrow m_F - 1$ .

When measuring  $x$  component of the spin of a photon moving along  $\vec{e}_x$  direction (spin projection along the direction of motion is called helicity) it can have helicity  $+1$ , corresponding to  $\sigma^+$  polarization along  $\vec{e}_x$ , or helicity  $-1$ , corresponding to  $\sigma^-$  polarization along  $\vec{e}_x$  (0 is not allowed due to the fact that photon is massless particle). However it can be in arbitrary superposition of these two states (like spin of the electron), resulting e.g.  $\pi$  polarization.

## 6.8 Conclusion

In this chapter we have discussed the quantum spin phases and the associated quantum phase transitions for a two-component Fermi lattice gas, focusing on the case of a two-leg ladderlike lattice at half filling. We have shown that for USOC along the ladder rungs the Néel-state phase is located within the RS-F phase, in which an RS may be adiabatically connected to an F phase in the parameter space of  $h$  and the SOC. In contrast, for USOC along the ladder legs the RS and F states cannot be adiabatically connected and are separated by an intermediate Néel state,

which disappears at maximal SOC to lead to a direct Gaussian RS-F quantum phase transition. The case of Rashba-like SOC is characterized by the appearance of RS and striped phases. Compared to the classical spin phases predicted for fermions on a square lattice with SOC [127], only the striped configurations of the 2D lattice have identical quantum counterparts on the ladder. On the contrary, the Néel and spiral waves are substituted by gapped RS states, whereas noncoplanar configurations such as vortex/antivortex textures are not stabilized.

The Néel and striped phases show long-range magnetic order, thus they can be observed experimentally in ultracold spinor Fermi gases with artificial SOC [17, 18] by Bragg diffraction of light [139], provided that cooling is achieved below the spin degeneracy temperature. The RS and F states have no long-range order, though they can be revealed by probing the local order similarly to recent experiments in Ref. [140]; e.g., two sites on the same rung will show antiferromagnetic superexchange interaction in the RS state and F correlation in the F state.

# Chapter 7

## Fidelity susceptibility at Berezinskii-Kosterlitz-Thouless transition

The analysis of the fidelity susceptibility (FS) has been extensively employed in this Thesis to map ground-state phase diagrams. This technique must be however handled with care at BKT transitions, where, as shown in this Chapter, FS presents a peculiar behavior.

### 7.1 Scaling of the FS at phase transitions

As discussed in chapter 2, the FS per site is given in terms of fidelity  $|F|$  by

$$\chi_L = \chi_F/L = 1/L \lim_{\delta\lambda \rightarrow 0} \frac{-2 \ln |F|}{(\delta\lambda)^2} \quad (7.1.1)$$

Hereafter we will focus on a one dimensional system with finite size  $L$ . If there is a phase transition (in the thermodynamical limit) at  $\lambda_c$ , for a finite system there is usually a peak of FS  $\chi_L$  near the critical point  $\lambda^*$ , obeying some scaling law. If the FS  $\chi_L$  can capture the phase transition,  $\chi_L$  will diverge when increasing the system size to infinite  $L \rightarrow \infty$  and  $\lambda^*$  approaching  $\lambda_c$ . For instance, for the Ising model  $H_{Ising} = -\sum_i (\sigma_i^x \sigma_{i+1}^x + \lambda \sigma_i^z)$ , it is well known that the scaling between the FS  $\chi_L$  and the system size  $L$  near the critical value (or at the critical value)  $\lambda_c = 1$

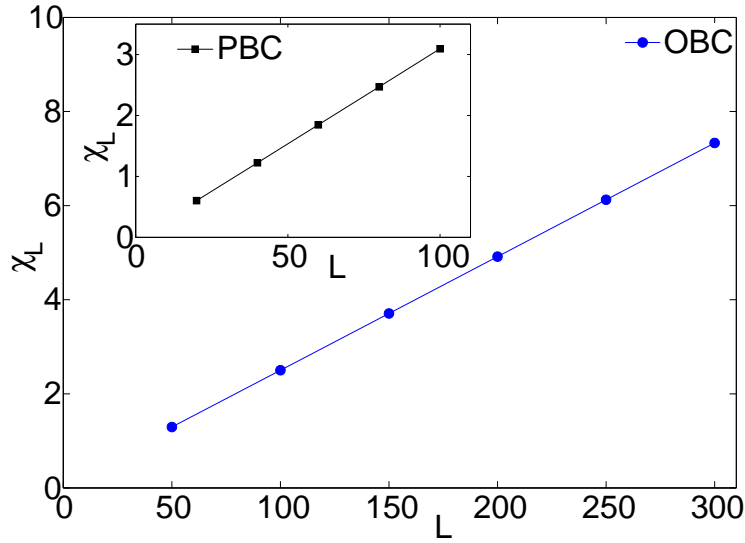


Figure 7.1: FS per site of the Ising model. Full blue circles correspond to our results for open boundary condition (OBC) up to  $L = 300$  sites. Full squares in the inset correspond to our results for periodic boundary condition (PBC) up to  $L = 100$  sites

is linear [42, 141]

$$\chi_L \propto L \quad (7.1.2)$$

This linear scaling dependence is confirmed by our DMRG calculations for both open boundary and periodic boundary conditions (see Fig.7.1). Assuming a translational invariant system with a unique ground state, perturbed by a local operator  $\hat{V} = \partial_\lambda \hat{\mathcal{H}} = \sum_x \hat{V}(x)$ , one obtains [142] the following connection between the FS and the reduced correlation function  $G(x, \tau) = \langle\langle \hat{V}(x, \tau) \hat{V}(0, 0) \rangle\rangle \equiv \langle \hat{V}(x, \tau) \hat{V}(0, 0) \rangle - \langle \hat{V}(0, 0) \rangle^2$ :

$$\chi_L = \int_a^L dx \int_0^\infty d\tau \tau G(x, \tau), \quad (7.1.3)$$

where the imaginary time evolution is defined by  $\hat{V}(x, \tau) = e^{\tau \hat{\mathcal{H}}} \hat{V}(x) e^{-\tau \hat{\mathcal{H}}}$ , averages are taken in the ground state  $|\psi_0(\lambda)\rangle$ , and  $a$  is the short-range (lattice) cutoff. Expression (7.1.3) diverges at  $L \rightarrow \infty$  as

$$\chi_L \propto L^{d+2z-2\Delta_V} \quad (7.1.4)$$

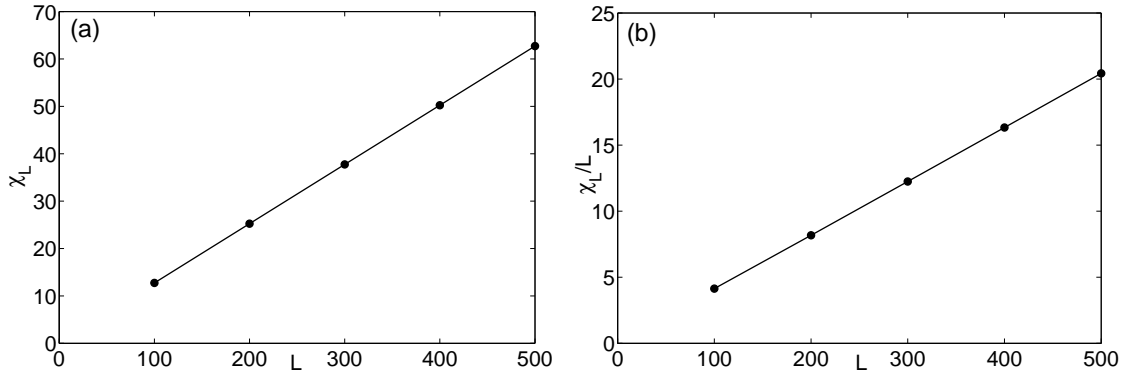


Figure 7.2: Finite-size scaling of FS at the peak position  $h = 0$  for spin- $\frac{1}{2}$  XXZ chain with a staggered field  $h$ , as a function of system size  $L$ ; symbols denote DMRG results, and lines are guide to the eye. (a)  $\lambda = 0$ ; (b)  $\lambda = 1$ ;

where  $\Delta_V$  is the scaling dimension of  $\hat{V}(x)$  at the critical point and  $z$  is the dynamic exponent, as long as  $\Delta_V < z + 1/2$ . At  $\Delta_V = z + 1/2$  there is only a logarithmic divergence [143], and with the further increase of  $\Delta_V$  the FS remains finite at the critical point.

To check the scaling law Eq.(7.1.4), let us consider the XXZ spin-1/2 chain with a staggered field  $h$  defined by the Hamiltonian

$$\hat{\mathcal{H}} = \hat{\mathcal{H}}_{XXZ} + h \sum_n (-1)^n S_n^z \quad (7.1.5)$$

where the XXZ model is defined by

$$\hat{\mathcal{H}}_{XXZ} = \sum_i (S_i^x S_{i+1}^x + S_i^y S_{i+1}^y + \lambda S_i^z S_{i+1}^z) \quad (7.1.6)$$

For XY model ( $\lambda = 0$  in Eq.(7.1.5)) with staggered field  $h$ , there is a Ising type transition at  $h = 0$  with,  $z = 1$  and  $\Delta_V = 1$ , the FS scales as  $\chi_L \propto L$ . For SU(2) Heisenberg model ( $\lambda = 1$  in Eq.(7.1.5)) with staggered field  $h$ , there is a Gaussian phase transition at  $h = 0$  with,  $z = 1$  and  $\Delta_V = 1/2$ , the FS scales as  $\chi_L \propto L^2$ . Our numerical results from DMRG up to  $L = 500$  sites show a very good agreement (see Fig.7.2) with the scaling law in Eq.(7.1.4).

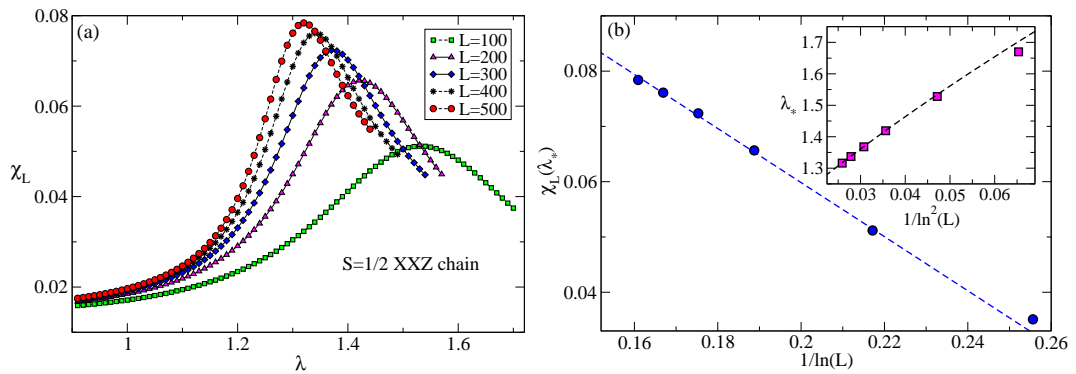


Figure 7.3: (a) FS for a spin- $\frac{1}{2}$  XXZ chain, as a function of the anisotropy  $\lambda$ ; symbols denote DMRG results, and lines are guide to the eye. (b) The finite-size scaling of the peak position  $\lambda_*$  and amplitude  $\chi_L(\lambda_*)$ ; lines result from fits to Eq.(7.2.1) and Eq.(7.2.2).

## 7.2 Fidelity susceptibility at BKT transitions

The above arguments [142] show that the FS must be insensitive not only against marginal and irrelevant perturbations ( $\Delta_V \geq z + 1$ ), but even against relevant perturbations with  $z + 1/2 < \Delta_V < z + 1$ . In the case of the BKT phase transition,  $z = 1$  and  $\Delta_V = 2$ , so it has been initially concluded [41,142,147] that transitions of this type cannot be detected by means of the finite-size scaling analysis of the FS.

So far the scaling law at a BKT transition has remained a controversial issue. It was shown in Ref. [144] and Ref. [145] that the FS diverges as  $\chi_{L \rightarrow \infty} \propto (1 - \lambda)^{-1}$ , whereas Ref. [146] reported a power law  $\chi_L = a + bL^c$ . However, on the other hand, in Ref. [41] and Ref. [147], it was shown that the FS does not diverge and cannot describe correctly BKT transitions. Recently, it was shown in Ref. [148] that the FS is logarithmic converged based on non-Abelian bosonization in terms of Wess-Zumino-Witten (WZW) theory,

$$\chi_L = \chi_0 - \chi_1/\ln(L/a) + O(1/\ln^2(L/a)) \quad (7.2.1)$$

$$\lambda_* = \lambda_0 + \lambda_1 + 1/\ln^2(L/a) + \dots \quad (7.2.2)$$

where  $a$  is the lattice cutoff. To support our calculations, we have performed DMRG calculations (using the MPS formulation) of the FS for the XXZ model, for large open chains of up to  $L = 500$  sites. The resulting FS as a function of  $\lambda$  is shown



### 7.3. Fidelity susceptibility at BKT transitions in other lattice models 101

in Fig. 7.3(a): as observed in previous studies for small systems, there is a peak with its height slowly growing and its position slowly converging with the increase of  $L$ . We start by fitting the finite-size dependence of the peak position  $\lambda_*$  with the help of the ansatz Eq.(7.2.2), which can be extracted by using standard scaling arguments [149] on the gapped side of the BKT transition: since the infinite-system correlation length in the vicinity of the transition behaves as  $\xi \propto ae^{-B/\sqrt{\lambda-\lambda_c}}$ , Eq. (7.2.2) is obtained by postulating that  $\xi \sim L$  at  $\lambda \sim \lambda_*$ . Further, when fitting the peak position  $\lambda_*$  according to Eq.(7.2.2), we fix  $\lambda_0 = 1$ , which allows us to extract the cutoff  $a$ . Subsequently, we use the extracted value of the cutoff when fitting the peak value  $\chi_L(\lambda_*)$  of the FS according to our result Eq.(7.2.1). The results of those fits, shown in Fig.7.3, demonstrate good agreement with the theory.

A note is in order: we have defined FS for non-degenerate ground states. For  $\lambda > 1$  the ground state of XXZ model in thermodynamic limit is doubly degenerate. However, for finite systems the ground state is unique for  $\lambda \simeq 1$ , even when  $\lambda > 1$ . With increasing system size the validity of our numerical FS data is shrinking in  $\lambda > 1$  region. Note that not all BKT phase transitions have such problems, i.e. the BKT phase transition in the 1D Bose Hubbard model and also the BKT transition in the spin-1 chain considered below are free of such a problem since both sides of the BKT phase transition are characterized by a unique ground state in the thermodynamic limit.

### 7.3 Fidelity susceptibility at BKT transitions in other lattice models

The above picture of non-diverging FS with strong logarithmic corrections due to marginal operators should be a generic feature of any BKT transition. To demonstrate that, we present here results of numerical studies for more models containing such transitions. The first model is the anisotropic spin-1 chain defined by the Hamiltonian

$$\hat{\mathcal{H}} = \sum_i \{J_1^\theta(\vec{S}_i \cdot \vec{S}_{i+1}) + J_2^\theta(\vec{S}_i \cdot \vec{S}_{i+1})^2 + D(S_i^z)^2\} \quad (7.3.1)$$

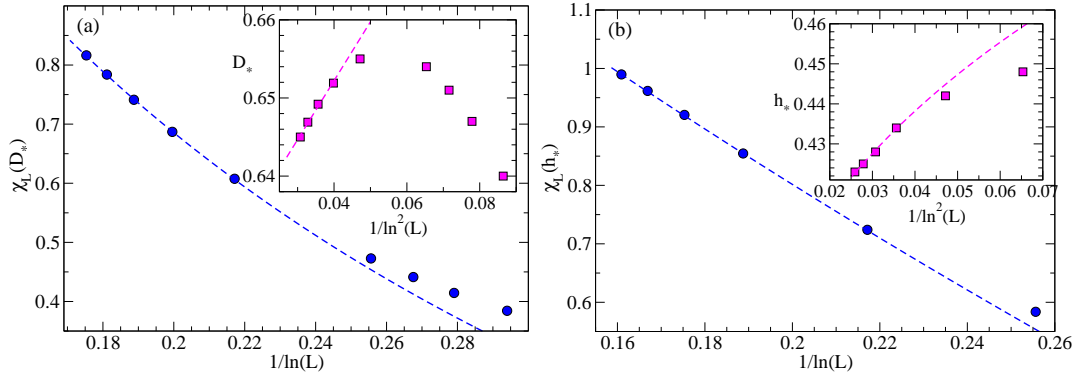


Figure 7.4: (a) Finite-size scaling of the peak position  $D_*$  and its value  $\chi_L(D_*)$ , for the FS with respect to the single-ion anisotropy  $D$  in the spin-1 chain model defined by the Hamiltonian (7.3.1) with  $\theta = -0.85\pi$ ; (b) the same for the peak position  $h_*$  and value  $\chi_L(h_*)$  of the FS with respect to the staggered field  $h$  in the spin- $\frac{1}{2}$  anisotropic chain Eq.(7.1.5) at  $\lambda = -0.9$ . Symbols show numerical (DMRG) results, and lines represent fits to the scaling laws (7.2.1), (7.2.2).

where  $\vec{S}_i$  are spin-1 operators at site  $i$ ,  $J_1^\theta = \cos \theta$  and  $J_2^\theta = \sin \theta$  are exchange constants, and  $D > 0$  is the single-ion anisotropy. For  $\theta \in [-\frac{3\pi}{2}, -\frac{3\pi}{4}]$ , with the increase of  $D$  this model exhibits a BKT transition from the gapless ferromagnetic XY phase to the gapped large- $D$  phase, recently studied [150] in the context of spinor bosons. Numerically, the FS as function of  $D$  exhibits a slowly growing peak [150], quite similar to the picture shown in Fig.7.3(a). Here we extend the result of Ref. [150] to much larger systems and show that the finite-size behavior of the peak height and position is consistent with the scaling formulas Eq.(7.2.1) and Eq.(7.2.2), (see Fig.7.4(a)).

One more example is the spin- $\frac{1}{2}$  ferromagnetic anisotropic chain perturbed by a staggered field  $h$  defined by Hamiltonian Eq.(7.1.5) with  $-1 < \lambda < 0$ ;

$$\hat{\mathcal{H}} = \hat{\mathcal{H}}_{XXZ} + h \sum_n (-1)^n S_n^z$$

For  $-1/\sqrt{2} < \lambda \leq 1$  any value of  $h$  opens up a gap in the excitation spectrum, and hence  $h = 0$  represents a Gaussian phase transition line with a continuously changing critical exponent as a function of  $\lambda$ . For  $-1 < \lambda < -1/\sqrt{2}$ , this model exhibits a BKT phase transition from a gapless Luttinger liquid (for  $|h| < |h_c|$ ) to a gapped

antiferromagnetic phase (for  $|h| > |h_c|$ ) at a finite value of the field  $|h| = |h_c(\lambda)| > 0$ . Our DMRG calculations for the FS as function of  $h$  show the same typical behavior of a slowly growing and poorly converging peak, and the finite-size scaling results presented in Fig.7.4(b) show that the numerical data is again consistent with the scaling laws Eq.(7.2.1), Eq.(7.2.2).

## 7.4 Conclusion

In summary, we have numerically shown that FS does not diverge at BKT transitions in one spatial dimension. Instead, it exhibits a finite-amplitude peak in the vicinity of the transition, with logarithmic finite-size scaling corrections of the form Eq.(7.2.1) and Eq.(7.2.2), which are too easy to confuse numerically with a logarithmic growth of the peak. On the practical side, our results indicate that using the FS as a tool to detect BKT transitions is extremely inconvenient, since the uncertainties of logarithmic fits remain too strong, even if one goes to the largest numerically tractable system sizes. Using other detection methods, e.g., looking at discontinuities of fidelity, as proposed in Ref. [152], might be a better alternative.



# Chapter 8

## Conclusions and outlook

In this thesis various scenarios were presented in which the physics of spin-orbital models may be studied with ultra-cold atoms or molecules in different kinds of optical lattices.

In chapters 4 and 5, Kugel-Khomskii type spin-orbital models were explored and studied for two-component dipolar fermions and bosons respectively in zig-zag lattices. We have shown, that thanks to the long-range properties of dipolar particles and the easily controllable properties of optical lattices, using fermions it is possible to engineer frustrated models and exotic phases relevant to solid states physics or even beyond, such as the  $SU(2)$  spontaneously symmetry broken spin-orbit liquid. Dipolar bosons in zig-zag optical lattices also show interesting properties e.g. they can develop a non-local topological order due to infinitesimal quantum fluctuations (order-by-disorder) and for certain parameters a quadratic dimerized phase with quadrupled unit cell can be realized.

In chapter 6, unidirectional spin-orbit coupling was studied for two-component fermions in ladder-like lattices. Because of the inherent strong 1D quantum fluctuations that are present in ladder systems, our DMRG simulations shed light on the rich ground state quantum phases for spin-orbit coupled systems that can be studied in future experiments.

In chapter 7, the behavior of the ground state fidelity at Berezinskii-Kosterlitz-Thouless quantum phase transitions in 1D systems was studied. It is shown that the fidelity susceptibility at BKT transitions does not diverge but logarithmically

converges to a finite value. The position of the peak in fidelity susceptibility scales logarithmically slowly in system size to its thermodynamic value. Therefore, one should be careful when using fidelity susceptibility to distinguish the BKT transitions numerically, while in contrast, fidelity susceptibility works quite well for locating thermodynamic critical point in Ising type transitions.

Possible extensions of the work of this thesis include:

- Whereas in this thesis we focused on magnetic properties it may be interesting to generalize our work to the original Hubbard models, where the interplay between "charge" degree of freedom and orbital degeneracy is expected to lead to interesting new phases.

- Another possible future direction is provided by density-dependent gauge fields, which may be induced by employing modulated interactions (as we recently studied in a work which has not been discussed in this thesis Ref. [153]). The interplay between density and phase is also expected to lead to interesting novel physics, mostly unexplored at this moment.

- Finally, more numerical work on other models of interest is desired to confirm the scaling laws for FS at BKT transitions and determine effect of boundary conditions.

# Bibliography

- [1] *Doping a Mott insulator: Physics of high-temperature superconductivity*, P. A. Lee, N. Nagaosa, and X.-G Wen, Rev. Mod. Phys. **78**, 17 (2006).
- [2] A. Auerbach, *Interacting electrons and quantum magnetism*, Springer, Heidelberg, 1998.
- [3] N. Nagaosa, *Quantum Field Theory in Strongly Correlated Electronic Systems*, Springer, Heidelberg, 1999.
- [4] T. Giamarchi, *Quantum Physics in one dimension*, Oxford University Press, (2003).
- [5] R. P. Feynman, *Simulating physics with computers*, Int. J. Theor. Phys. 21, 467-488 (1982).
- [6] K. G. Wilson, *The renormalization group: Critical phenomena and the Kondo problem*, Rev. Mod. Phys. **47**, 773 (1975).
- [7] S. R. White, *Density matrix formulation for quantum renormalization groups*, Phys. Rev. Lett. **69**, 2863 (1992).
- [8] S. R. White, *Density-matrix algorithms for quantum renormalization groups*, Phys. Rev. B **48**, 10345 (1993).
- [9] F. Verstraete, J.I. Cirac, V. Murg, *Matrix product states, projected entangled pair states, and variational renormalization group methods for quantum spin systems*, Adv. Phys. 57,143 (2008).

- [10] G. Vidal, *Class of Quantum Many-Body States That Can Be Efficiently Simulated*, Phys. Rev. Lett. **101**, 110501 (2008).
- [11] I. M. Georgescu, S. Ashhab, and F. Nori, *Quantum simulation*, Rev. Mod. Phys. **86**, 153 (2014).
- [12] I. Bloch, J. Dalibard, and W. Zwerger, *Many-body physics with ultracold gases*, Rev. Mod. Phys. **80**, 885 (2008).
- [13] M. Lewenstein, A. Sanpera, V. Ahufinger, B. Damski, A. Sen De, and U. Sen, *Ultracold atomic gases in optical lattices: mimicking condensed matter physics and beyond*, Adv. Phys. **56**, 243 (2007).
- [14] D. Jaksch, C. Bruder, J. I. Cirac, C. W. Gardiner, and P. Zoller, *Cold Bosonic Atoms in Optical Lattices*, Phys. Rev. Lett. **81**, 3108 (1998).
- [15] M. Greiner, O. Mandel, T. Esslinger, T. W. Hänsch, and I. Bloch, *Quantum phase transition from a superfluid to a Mott insulator in a gas of ultracold atoms*, Nature **415**, 39-44 (2002).
- [16] Y.-J. Lin, K. Jimenez-Garcia, and I. B. Spielman, *Spin-orbit-coupled Bose-Einstein condensates*, Nature **471**, 83 (2011).
- [17] P. Wang, Z. Q. Yu, Z. Fu, J. Miao, L. Huang, S. Chai, H. Zhai, and J. Zhang, *Spin-Orbit Coupled Degenerate Fermi Gases*, Phys. Rev. Lett. **109**, 095301 (2012).
- [18] L. W. Cheuk, A. T. Sommer, Z. Hadzibabic, T. Yefsah, W. S. Bakr, and M. W. Zwierlein, *Spin-Injection Spectroscopy of a Spin-Orbit Coupled Fermi Gas*, Phys. Rev. Lett. **109**, 095302 (2012).
- [19] G. Wirth, M. Ölschläger and A. Hemmerich, *Evidence for orbital superfluidity in the P-band of a bipartite optical square lattice*, Nature Physics **7**, 147 (2010).
- [20] C. Becker, P. Soltan-Panahi, J. Kronjäger, S. Dörscher, K. Bongs, K. Sengstock, *Ultracold quantum gases in triangular optical lattices*, New J. Phys. **12** 065025 (2010).



- [21] G. Sun, G. Jackeli, L. Santos, and T. Vekua, *Exploring spin-orbital models with dipolar fermions in zigzag optical lattices*, Phys. Rev. B **86**,155159 (2012).
- [22] . S. Greschner, L. Santos, and T. Vekua, *Ultracold bosons in zig-zag optical lattices*, Phys. Rev. A **87**, 033609 (2013).
- [23] I. Bloch, *Ultracold quantum gases in optical lattices*, Nature Physics **1**, 23-30 (2005).
- [24] L. D. Landau and E. M. Lifshitz, *Quantum Mechanics - Non-relativistic Theory*, Third Edition, **p504**, Elsevier Science, (1977).
- [25] J. Dalibard, *Collisional dynamics of ultra-cold atomic gases*, edited by M. Inguscio, S. Stringari, and C. E. Wieman, *Proceedings of the International School of Physics - Enrico Fermi*, **p321**, IOS Press, (1999).
- [26] D. J. Heinzen, *Ultracold atomic interactions*, edited by M. Inguscio, S. Stringari, and C. E. Wieman, *Proceedings of the International School of Physics - Enrico Fermi*, **p321**, IOS Press, (1999).
- [27] C. J. Pethick and H. Smith, *Bose-Einstein Condensation in Dilute Gases*, **p102**, Cambridge University Press, (2002).
- [28] T. Lahaye, C. Menotti, L. Santos, M. Lewenstein, and T. Pfau, *The physics of dipolar bosonic quantum gases*, Reports on Progress in Physics, **72**, 126401 (2009).
- [29] D. M. Stamper-Kurn and M. Ueda, *Spinor Bose gases: Symmetries, magnetism, and quantum dynamics*, Rev. Mod. Phys. **85**, 1191 (2013)
- [30] S. Yi and L. You, *Trapped atomic condensates with anisotropic interactions*, Phys. Rev. A **61**, 041604(R) (2010)
- [31] C. Trefzger, C. Menotti, B. Capogrosso-Sansone, and M. Lewenstein, *Ultracold dipolar gases in optical lattices* , J. Phys. B: At. Mol. Opt. Phys. **44**, 193001 (2011).

- [32] Y.-J. Lin, R. L. Compton, K. Jimenez-Garcia, J. V. Porto, and I. B. Spielman, *Synthetic magnetic fields for ultracold neutral atoms*, Nature **462**, 628 (2009).
- [33] Y. A. Bychkov and E. I. Rashba, *Oscillatory effects and the magnetic susceptibility of carriers in inversion layers*, J. Phys. C **17**, 6039 (1984).
- [34] G. Dresselhaus, *Spin-Orbit Coupling Effects in Zinc Blende Structures*, Phys. Rev. **100**, 580 (1955).
- [35] J. Alicea, Y. Oreg, G. Refael, F. von Oppen, and M. P. A. Fisher, *Non-Abelian statistics and topological quantum information processing in 1D wire networks*, Nat. Phys. **7**, 412 (2011).
- [36] E.M. Stoudenmire, J. Alicea, O.A. Starykh, and M.P.A. Fisher, *Interaction effects in topological superconducting wires supporting Majorana fermions*, Phys. Rev. B **84**, 014503 (2011).
- [37] K. I. Kugel and D. I. Khomskii, *The Jahn-Teller effect and magnetism: transition metal compounds*, Sov. Phys. Usp. **25**, 231 (1982).
- [38] L.F. Feiner, A.M. Oleś, and J. Zaanen, *Quantum Melting of Magnetic Order due to Orbital Fluctuations*, Phys. Rev. Lett. **78**, 2799 (1997).
- [39] P. Zanardi and N. Paunkovic, *Ground state overlap and quantum phase transitions*, Phys. Rev. E **74**, 031123 (2006).
- [40] L. Campos Venuti and P. Zanardi, *Quantum Critical Scaling of the Geometric Tensors*, Phys. Rev. Lett. **99**, 095701 (2007).
- [41] W.-L. You, Y.-W. Li, and S.-J. Gu, *Fidelity, dynamic structure factor, and susceptibility in critical phenomena*, Phys. Rev. E **76**, 022101 (2007).
- [42] S. J. Gu, *Fidelity approach to quantum phase transitions*, Int. J. Mod. Phys. B, **24**, 4371 (2010).
- [43] A. W. Sandvik, *Computational Studies of Quantum Spin Systems*, AIP Conf. Proc. bf 1297, 135 (2010).

- [44] Web: <http://www.caam.rice.edu/software/ARPACK/>  
and <http://www.netlib.org/lapack/>
- [45] S. R. White and R.M. Noack, *Real-space quantum renormalization groups*, Phys. Rev. Lett. **68**, 3487 (1992).
- [46] S. Ostlund and S. Rommer, *Thermodynamic Limit of Density Matrix Renormalization*, Phys. Rev. Lett. **75**, 3537 (1995).
- [47] S. Rommer and S. Ostlund, *Class of ansatz wave functions for one-dimensional spin systems and their relation to the density matrix renormalization group*, Phys. Rev. B **55**, 2164 (1997).
- [48] F. Verstraete, D. Porras, J. I. Cirac, *Density Matrix Renormalization Group and Periodic Boundary Conditions: A Quantum Information Perspective*, Phys. Rev. Lett. **93**, 227205 (2004).
- [49] U. Schollwöck, *The density-matrix renormalization group in the age of matrix product states*, Annals of Physics **326**, 96192 (2011).
- [50] G. Vidal, *Efficient Classical Simulation of Slightly Entangled Quantum Computations*, Phys. Rev. Lett. **91**, 147902 (2003).
- [51] G. Vidal, *Efficient Simulation of One-Dimensional Quantum Many-Body Systems*, Phys. Rev. Lett. **93**, 040502 (2004).
- [52] G. Vidal, *Classical Simulation of Infinite-Size Quantum Lattice Systems in One Spatial Dimension*, Phys. Rev. Lett. **98**, 070201 (2007).
- [53] A. J. Daley, C. Kollath, U. Schollwöck and G. Vidal, *Time-dependent density-matrix renormalization-group using adaptive effective Hilbert spaces*, J. Stat. Mech. **P04005**, (2004).
- [54] S. R. White and Adrian E. Feiguin, *Real-Time Evolution Using the Density Matrix Renormalization Group*, Phys. Rev. Lett. **93**, 076401 (2004).
- [55] S. Singh, R. N. C. Pfeifer, G. Vidal, *Tensor network decompositions in the presence of a global symmetry*, Phys. Rev. A **82**, 050301 (2010).

- [56] S. Singh, R. N. C. Pfeifer, G. Vidal, *Tensor network states and algorithms in the presence of a global  $U(1)$  symmetry*, Phys. Rev. B **83**, 115125 (2011).
- [57] E. Jeckelmann, *Density-matrix renormalization group algorithms*, Computational Many Particle Physics, **597-619**, Springer-Verlag, Berlin, Heidelberg, (2008).
- [58] Y. Tokura and N. Nagaosa, *Orbital Physics in Transition-Metal Oxides*, Science **288**, 462 (2000).
- [59] E. Dagotto, *Complexity in Strongly Correlated Electronic Systems*, Science **309**, 257 (2005).
- [60] G. Khaliullin and S. Maekawa, *Orbital Liquid in Three-Dimensional Mott Insulator:  $LaTiO_3$* , Phys. Rev. Lett. **85**, 3950 (2000).
- [61] F. Wang and A. Vishwanath,  *$Z_2$  spin-orbital liquid state in the square lattice Kugel-Khomskii model*, Phys. Rev. B **80**, 064413 (2009).
- [62] P. Corboz, A.M. Läuchli, K. Penc, M. Troyer, and F. Mila, *Simultaneous Dimerization and  $SU(4)$  Symmetry Breaking of 4-Color Fermions on the Square Lattice*, Phys. Rev. Lett. **107**, 215301 (2011).
- [63] J. Chaloupka, G. Jackeli, and G. Khaliullin, *Kitaev-Heisenberg Model on a Honeycomb Lattice: Possible Exotic Phases in Iridium Oxides  $A_2IrO_3$* , Phys. Rev. Lett. **105**, 027204 (2010).
- [64] G. Jackeli and D.A. Ivanov, *Dimer phases in quantum antiferromagnets with orbital degeneracy*, Phys. Rev. B **76**, 132407 (2007).
- [65] G. Jackeli and D.I. Khomskii, *Classical Dimers and Dimerized Superstructure in an Orbitally Degenerate Honeycomb Antiferromagnet*, Phys. Rev. Lett. **100**, 147203 (2008).
- [66] C. Wu, D. Bergman, L. Balents, and S. Das Sarma, *Flat Bands and Wigner Crystallization in the Honeycomb Optical Lattice*, Phys. Rev. Lett. **99**, 070401 (2007).

- [67] M. Hermele, V. Gurarie, and A. M. Rey, *Mott Insulators of Ultracold Fermionic Alkaline Earth Atoms: Underconstrained Magnetism and Chiral Spin Liquid*, Phys. Rev. Lett. **103**, 135301 (2009).
- [68] A.V. Gorshkov, M. Hermele, V. Gurarie, C. Xu, P. S. Julienne, J. Ye, P. Zoller, E. Demler, M. D. Lukin, and A. M. Rey, *Two-orbital  $SU(N)$  magnetism with ultracold alkaline-earth atoms*, Nature Physics **6**, 289 (2010).
- [69] C. Chin, R. Grimm, P. Julienne, and E. Tiesinga, *Feshbach resonances in ultracold gases*, Rev. Mod. Phys. **82**, 1225 (2010).
- [70] J. Struck, C. Ölschläger, R. Le Targat, P. Soltan-Panahi, A. Eckardt, M. Lewenstein, P. Windpassinger, and K. Sengstock, *Quantum Simulation of Frustrated Classical Magnetism in Triangular Optical Lattices*, Science **333**, 996 (2011).
- [71] G.-B. Jo, J. Guzman, C. K. Thomas, P. Hosur, A. Vishwanath, and D. M. Stamper-Kurn, *Ultracold Atoms in a Tunable Optical Kagome Lattice*, Phys. Rev. Lett. **108**, 045305 (2012).
- [72] T. Lahaye, T. Koch, B. Fröhlich, M. Fattori, J. Metz, A. Griesmaier, S. Giovanazzi, and T. Pfau, *Strong dipolar effects in a quantum ferrofluid*, Nature **448**, 672 (2007).
- [73] M. Lu, N. Q. Burdick, S. H. Youn, and B. L. Lev, *Strongly Dipolar Bose-Einstein Condensate of Dysprosium*, Phys. Rev. Lett. **107**, 190401 (2011).
- [74] K.-K. Ni, S. Ospelkaus, D. Wang, G. Quémener, B. Neyenhuis, M. H. G. de Miranda, J. L. Bohn, J. Ye, and D. S. Jin, *Dipolar collisions of polar molecules in the quantum regime*, Nature **464**, 1324 (2010).
- [75] K. Góral, L. Santos, and M. Lewenstein, *Quantum Phases of Dipolar Bosons in Optical Lattices*, Phys. Rev. Lett. **88**, 170406 (2002).
- [76] L. He and W. Hofstetter, *Supersolid phase of cold fermionic polar molecules in two-dimensional optical lattices*, Phys. Rev. A **83**, 053629 (2011).

- [77] M.J. Konstantinović, J. van den Brink, Z. V. Popović, V. V. Moshchalkov, M. Isobe, and Y. Ueda, *Orbital dimerization in  $\text{NaTiSi}_2\text{O}_6$ : An orbital analogue of the spin-Peierls phase transition*, Phys. Rev. B **69**, 020409(R) (2004).
- [78] T. Hikihara and Y. Motome, *Orbital and spin interplay in spin-gap formation in pyroxene  $\text{ATiSi}_2\text{O}_6$  ( $A=\text{Na},\text{Li}$ )*, Phys. Rev. B **70**, 214404 (2004).
- [79] G. Jackeli and G. Khaliullin, *Magnetically Hidden Order of Kramers Doublets in  $d^1$  Systems:  $\text{Sr}_2\text{VO}_4$* , Phys. Rev. Lett. **103**, 067205 (2009).
- [80] E. Lieb, T. Schultz, and D. Mattis, *Two soluble models of an antiferromagnetic chain*, Ann. Phys. (NY) **16**, 407 (1961).
- [81] C. K. Majumdar and D. Ghosh, *On Next-Nearest-Neighbor Interaction in Linear Chain*, J. Math. Phys. **10**, 1388 (1969).
- [82] K. Okamoto and K. Nomura, *Fluid-dimer critical point in  $S = \frac{1}{2}$  antiferromagnetic Heisenberg chain with next nearest neighbor interactions*, Phys. Lett. A **169**, 433 (1992).
- [83] S. R. White and I. Affleck, *Dimerization and incommensurate spiral spin correlations in the zigzag spin chain: Analogies to the Kondo lattice*, Phys. Rev. B **54**, 9862 (1996).
- [84] A.A. Nersesyan, A.O. Gogolin, and F. H. L. Eßler, *Incommensurate Spin Correlations in Spin-1/2 Frustrated Two-Leg Heisenberg Ladders*, Phys. Rev. Lett. **81**, 910 (1998).
- [85] S. Furukawa, M. Sato, and S. Onoda, *Chiral Order and Electromagnetic Dynamics in One-Dimensional Multiferroic Cuprates*, Phys. Rev. Lett. **105**, 257205 (2010).
- [86] M. Sato, S. Furukawa, S. Onoda, and A. Furusaki, *Competing phases in spin-1/2  $J_1 - J_2$  chain with easy-plane anisotropy*, Mod. Phys. Lett. B **25**, 901 (2011).

- [87] S. Furukawa, M. Sato, S. Onoda, and A. Furusaki, *Ground-state phase diagram of a spin-1/2 frustrated ferromagnetic XXZ chain: Haldane dimer phase and gapped/gapless chiral phases*, Phys. Rev. B **86**, 094417 (2012).
- [88] J. M. Kosterlitz and D. J. Thouless, *Ordering, metastability and phase transitions in two-dimensional systems*, J. Phys. C **6**, 1181 (1973).
- [89] J. N. Fuchs, D. M. Gangardt, T. Keilmann, and G. V. Shlyapnikov, *Spin Waves in a One-Dimensional Spinor Bose Gas*, Phys. Rev. Lett. **95**, 150402 (2005).
- [90] M. T. Batchelor, M. Bortz, X. W. Guan, and N. Oelkers, *Collective dispersion relations for the one-dimensional interacting two-component Bose and Fermi gases*, J. Stat. Mech. P03016 (2006).
- [91] M. B. Zvonarev, V. V. Cheianov, and T. Giamarchi, *Spin Dynamics in a One-Dimensional Ferromagnetic Bose Gas*, Phys. Rev. Lett. **99**, 240404 (2007).
- [92] A. Kleine, C. Kollath, I. P. McCulloch, T. Giamarchi, and U. Schollwöck, *Excitations in two-component Bose gases*, New J. Phys. **10**, 045025 (2008).
- [93] M.-C. Chung and A. B. Bhattacharjee, *Dynamical Structure Factor and Spin-Density Separation for a Weakly Interacting Two-Component Bose Gas*, Phys. Rev. Lett. **101**, 070402 (2008).
- [94] T. Shimokawa and H. Nakano, *Frustration-Induced Ferrimagnetism in  $S = 1/2$  Heisenberg Spin Chain*, J. Phys. Soc. Jpn. **80**, 043703 (2011).
- [95] S. Ospelkaus, K.-K. Ni, G. Quéméner, B. Neyenhuis, D. Wang, M. H. G. de Miranda, J. L. Bohn, J. Ye, and D. S. Jin, *Controlling the Hyperfine State of Rovibronic Ground-State Polar Molecules*, Phys. Rev. Lett. **104**, 030402 (2010).
- [96] A. Frisch, K. Aikawa, M. Mark, F. Ferlaino, E. Berseneva, and S. Kotochigova, *Hyperfine structure of laser-cooling transitions in fermionic erbium-167*, Phys. Rev. A **88**, 032508 (2013).

- [97] D. McKay and B. DeMarco, *Cooling in strongly correlated optical lattices: prospects and challenges*, Rep. Prog. Phys. **74**, 054401 (2011).
- [98] T. Giamarchi, C. Rüegg, and O. Tchernyshyov, *Bose-Einstein condensation in magnetic insulators*, Nat. Phys. **4**, 198 (2008).
- [99] S. Sachdev, *Quantum magnetism and criticality*, Nat. Phys. **4**, 173 (2008).
- [100] L. Balents, *Spin liquids in frustrated magnets*, Nature **464**, 199 (2010).
- [101] S. Trotzky, Y. A. Chen, U. Schnorrberger, P. Cheinet, and I. Bloch, *Controlling and Detecting Spin Correlations of Ultracold Atoms in Optical Lattices*, Phys. Rev. Lett. **105**, 265303 (2010).
- [102] A. de Paz, A. Sharma, A. Chotia, E. Maréchal, J. H. Huckans, P. Pedri, L. Santos, O. Gorceix, L. Vernac, and B. Laburthe-Tolra, *Nonequilibrium Quantum Magnetism in a Dipolar Lattice Gas*, Phys. Rev. Lett. **111**, 185305 (2013).
- [103] K. Aikawa, D. Akamatsu, J. Kobayashi, M. Ueda, T. Kishimoto, and S. Inouye, *Toward the production of quantum degenerate bosonic polar molecules  $^{41}\text{K}^{87}\text{Rb}$* , New J. Phys. **11**, 055035 (2009).
- [104] F. D. M. Haldane, *Continuum dynamics of the 1-D Heisenberg antiferromagnet: Identification with the  $O(3)$  nonlinear sigma model*, Phys. Lett. A **93**, 464 (1983).
- [105] *Nonlinear Field Theory of Large-Spin Heisenberg Antiferromagnets: Semiclassically Quantized Solitons of the One-Dimensional Easy-Axis Néel State*, Phys. Rev. Lett. **50**, 1153 (1983).
- [106] M. den Nijs and K. Rommelse, *Preroughening transitions in crystal surfaces and valence-bond phases in quantum spin chains*, Phys. Rev. B **40**, 4709 (1989).
- [107] H. T. Diep, *Frustrated Spin Systems* (World Scientific, Singapore, 2004).
- [108] J. Villain, R. Bidaux, J. P. Carton, and R. Conte, *Order as an effect of disorder*, J. Physique **41**, 1263 (1980).



- [109] A. Chubukov, *Order from disorder in a kagomé antiferromagnet*, Phys. Rev. Lett. **69**, 832 (1992).
- [110] E. Rastelli and A. Tassi, *Order produced by quantum disorder in the Heisenberg rhombohedral antiferromagnet*, J. Phys. C **20**, L303 (1987).
- [111] C. L. Henley, *Ordering due to disorder in a frustrated vector antiferromagnet*, Phys. Rev. Lett. **62**, 2056 (1989).
- [112] J. L. Song, G. W. Semenoff, and F. Zhou, *Uniaxial and Biaxial Spin Nematic Phases Induced by Quantum Fluctuations*, Phys. Rev. Lett. **98**, 160408 (2007).
- [113] A. M. Turner, R. Barnett, E. Demler, and A. Vishwanath, *Nematic Order by Disorder in Spin-2 Bose-Einstein Condensates*, Phys. Rev. Lett. **98**, 190404 (2007).
- [114] T. Kennedy and H. Tasaki, *Hidden  $Z_2 \times Z_2$  symmetry breaking in Haldane-gap antiferromagnets*, Phys. Rev. B **45**, 304 (1992).
- [115] T. Kennedy and H. Tasaki, *Hidden symmetry breaking and the Haldane phase in  $S = 1$  quantum spin chains*, Commun. Math. Phys. **147**, 431 (1992).
- [116] R. Chitra, S. Pati, H. R. Krishnamurthy, D. Sen, and S. Ramasesha, *Density-matrix renormalization-group studies of the spin-1/2 Heisenberg system with dimerization and frustration*, Phys. Rev. B **52**, 6581 (1995).
- [117] S. Brehmer, H. J. Mikeska, and U. Neugebauer, *The phase diagram and hidden order for generalized spin ladders*, J. Phys.:Condens. Matter **8**, 7161 (1996).
- [118] K. Góral, K. Rzażewski, and T. Pfau, *Bose-Einstein condensation with magnetic dipole-dipole forces*, Phys. Rev. A **61**, 051601(R) (2000).
- [119] L. J. LeBlanc, K. Jiménez-García, R. A. Williams, M. C. Beeler, A. R. Perry, W. D. Phillips, and I. B. Spielman, *Observation of a superfluid Hall effect*, Proc. Natl. Acad. Sci. USA **109**, 10811 (2012).

- [120] L. J. LeBlanc, M. C. Beeler, K. Jiménez-García, A. R. Perry, S. Sugawa, R. A. Williams, and I. B. Spielman, *Direct observation of zitterbewegung in a Bose-Einstein condensate*, New J. Phys. **15**, 073011 (2013).
- [121] M. C. Beeler R. A. Williams, K. Jiménez-García, L. J. LeBlanc, A. R. Perry and I. B. Spielman, *The spin Hall effect in a quantum gas*, Nature 498, 201 (2013).
- [122] D. L. Campbell, G. Juzeliunas, and I. B. Spielman, *Realistic Rashba and Dresselhaus spin-orbit coupling for neutral atoms*, Phys. Rev. A **84**, 025602 (2011).
- [123] B. M. Anderson, I. B. Spielman, and G. Juzeliunas, *Magnetically Generated Spin-Orbit Coupling for Ultracold Atoms*, Phys. Rev. Lett. **111**, 125301 (2013).
- [124] B. M. Anderson, G. Juzeliunas, V. M. Galitski, and I. B. Spielman, *Synthetic 3D Spin-Orbit Coupling*, Phys. Rev. Lett. **108**, 235301 (2012).
- [125] Z. Cai, X. Zhou, and C. Wu, *Magnetic phases of bosons with synthetic spin-orbit coupling in optical lattices*, Phys. Rev. A **85**, 061605(R) (2012).
- [126] W. S. Cole, S. Zhang, A. Paramekanti, and N. Trivedi, *Bose-Hubbard Models with Synthetic Spin-Orbit Coupling: Mott Insulators, Spin Textures, and Superfluidity*, Phys. Rev. Lett. **109**, 085302 (2012).
- [127] J. Radic, A. Di Ciolo, K. Sun, and V. Galitski, *Exotic Quantum Spin Models in Spin-Orbit-Coupled Mott Insulators*, Phys. Rev. Lett. **109**, 085303 (2012).
- [128] M. Takahashi, *Thermodynamics of One-Dimensional Solvable Models* (Cambridge University Press, Cambridge, UK, 1999).
- [129] M. Oshikawa and I. Affleck, *Field-Induced Gap in  $S=1/2$  Antiferromagnetic Chains*, Phys. Rev. Lett. **79**, 2883 (1997).
- [130] M. Fabrizio, A. O. Gogolin, and A. A. Nersesyan, *From Band Insulator to Mott Insulator in One Dimension*, Phys. Rev. Lett. **83**, 2014 (1999).

- [131] A. P. Kampf, M. Sekania, G. I. Japaridze, and P. Brune, *Nature of the insulating phases in the half-filled ionic Hubbard model*, J. Phys.: Condens. Matter **15**, 5895 (2003).
- [132] S. R. Manmana, V. Meden, R. M. Noack, and K. Schönhammer, *Quantum critical behavior of the one-dimensional ionic Hubbard model*, Phys. Rev. B **70**, 155115 (2004).
- [133] K. Penc, J. B. Fouet, S. Miyahara, O. Tchernyshyov, and F. Mila, *Ising Phases of Heisenberg Ladders in a Magnetic Field*, Phys. Rev. Lett. **99**, 117201 (2007).
- [134] A. A. Ovchinnikov, D. V. Dmitriev, V. Y. Krivnov, and V. O. Chervanovskii, *Antiferromagnetic Ising chain in a mixed transverse and longitudinal magnetic field*, Phys. Rev. B **68**, 214406 (2003).
- [135] D. V. Dmitriev and V. Y. Krivnov, *Anisotropic Heisenberg chain in coexisting transverse and longitudinal magnetic fields*, Phys. Rev. B **70**, 144414 (2004).
- [136] J.-S. Caux, F. H. L. Essler, and U. Löw, *Dynamical structure factor of the anisotropic Heisenberg chain in a transverse field*, Phys. Rev. B **68**, 134431 (2003).
- [137] Y.J. Wang, F. H. L. Essler, and M. Fabrizio, and A. A. Nersisyan, *Quantum criticalities in a two-leg antiferromagnetic  $S = 1/2$  ladder induced by a staggered magnetic field*, Phys. Rev. B **66**, 024412 (2002).
- [138] J. A. Riera, *Spin polarization in the Hubbard model with Rashba spin-orbit coupling on a ladder*, Phys. Rev. B **88**, 045102 (2013).
- [139] T. A. Corcovilos, S. K. Baur, J. M. Hitchcock, E. J. Mueller, and R. G. Hulet, *Detecting antiferromagnetism of atoms in an optical lattice via optical Bragg scattering*, Phys. Rev. A **81**, 013415 (2010).
- [140] D. Greif, T. Uehlinger, G. Jotzu, L. Tarruell, and T. Esslinger, *Short-Range Quantum Magnetism of Ultracold Fermions in an Optical Lattice*, Science **340**, 1307 (2013).

- [141] B. Damski, *Fidelity susceptibility of the quantum Ising model in a transverse field: The exact solution*, Phys. Rev. E **87**, 052131, (2013).
- [142] L. Campos Venuti and P. Zanardi, *Quantum Critical Scaling of the Geometric Tensors*, Phys. Rev. Lett. **99**, 095701 (2007).
- [143] S.-J. Gu and H.-Q. Lin, *Scaling dimension of fidelity susceptibility in quantum phase transitions*, EPL **87**, 10003 (2009).
- [144] M. F. Yang, *Ground-state fidelity in one-dimensional gapless models*, Phys. Rev. B **76**, 180403(R) (2007).
- [145] J. O. Fjærestad, *Ground state fidelity of Luttinger liquids: a wavefunctional approach*, J. Stat. Mech. P07011 (2008).
- [146] B. Wang, M. Feng, and Z.-Q. Chen, *Berezinskii-Kosterlitz-Thouless transition uncovered by the fidelity susceptibility in the XXZ model*, Phys. Rev. A **81**, 064301 (2010).
- [147] S. Chen, L. Wang, Y. Hao, and Y. P. Wang, *Intrinsic relation between ground-state fidelity and the characterization of a quantum phase transition*, Phys. Rev. A **77**, 032111 (2008).
- [148] G. Sun, A. K. Kolezhuk, T. Vekua, *Fidelity at Berezinskii-Kosterlitz-Thouless quantum phase transitions*, arXiv:1408.2739 (2014)
- [149] N. Schultka and E. Manousakis, *Finite-size scaling in two-dimensional superfluids*, Phys. Rev. B **49**, 12071 (1994).
- [150] K. Rodríguez, A. Argüelles, A. K. Kolezhuk, L. Santos, and T. Vekua, *Field-Induced Phase Transitions of Repulsive Spin-1 Bosons in Optical Lattices*, Phys. Rev. Lett. **106**, 105302 (2011).
- [151] T. Sowiński, M. Lacki, O. Dutta, J. Pietraszewicz, P. Sierant, M. Gajda, J. Zakrzewski, and M. Lewenstein, *Tunneling-Induced Restoration of the Degeneracy and the Time-Reversal Symmetry Breaking in Optical Lattices*, Phys. Rev. Lett. **111**, 215302 (2013).

- 
- [152] H.-L.Wang, A.-M. Chen, B. Li, and H.-Q. Zhou, *Ground-state fidelity and KosterlitzThouless phase transition for the spin-1/2 Heisenberg chain with next-to-the-nearest-neighbor interaction*, J. Phys.A: Math. Theor. **45**, 015306 (2012).
- [153] S. Greschner, G. Sun, D. Poletti, L. Santos, *Density dependent synthetic gauge fields using periodically modulated interactions*, arXiv:1311.3150 (2013).



# Appendix A

## Wannier functions

Let us consider two-component particles in a lattice,  $V(\mathbf{r})$ . In second quantization the Hamiltonian acquires the form:

$$H = \sum_{\sigma} \int \psi_{\sigma}^{\dagger}(\mathbf{r}) \left[ -\frac{\hbar^2}{2m} \nabla^2 + V(\mathbf{r}) \right] \psi_{\sigma}(\mathbf{r}) d\mathbf{r} + \sum_{\sigma, \sigma'} \int \psi_{\sigma}^{\dagger}(\mathbf{r}_1) \psi_{\sigma'}^{\dagger}(\mathbf{r}_2) \frac{U(\mathbf{r}_1 - \mathbf{r}_2)}{2} \psi_{\sigma'}(\mathbf{r}_2) \psi_{\sigma}(\mathbf{r}_1) d\mathbf{r}_1 d\mathbf{r}_2 \quad (\text{A.0.1})$$

where  $U(\mathbf{r}_1 - \mathbf{r}_2)$  is interparticle interaction. In absence of interactions, the eigenstates of Eq.(A.0.1) are described by Bloch waves  $\phi_{\alpha\mathbf{k}}(\mathbf{r})$ . where,  $\alpha$  is the band, and  $\mathbf{k}$  is the wave number in the first Brioullin zone. One may expand the field operator in terms of Bloch states as,

$$\psi_{\sigma}^{\dagger}(\mathbf{r}) = \sum_{\alpha, \mathbf{k}} \phi_{\alpha\mathbf{k}}^*(\mathbf{k}) c_{\alpha\mathbf{k}\sigma}^{\dagger} \quad (\text{A.0.2})$$

$$\psi_{\sigma}(\mathbf{r}) = \sum_{\alpha, \mathbf{k}} \phi_{\alpha\mathbf{k}}(\mathbf{r}) c_{\alpha\mathbf{k}\sigma} \quad (\text{A.0.3})$$

where  $c_{\alpha\mathbf{k}\sigma}^{\dagger}$  and  $c_{\alpha\mathbf{k}\sigma}$  are the creation and annihilation operations, respectively. Alternatively, one may employ Wannier functions insteads of Bloch states by introducing the following transformation,

$$w_{\alpha}(\mathbf{r} - \mathbf{R}_j) = \frac{1}{\sqrt{L^d}} \sum_{\mathbf{k}} e^{-i\mathbf{k}\cdot\mathbf{R}_j} \phi_{\alpha\mathbf{k}}(\mathbf{r}) \quad (\text{A.0.4})$$

$$\phi_{\alpha\mathbf{k}}(\mathbf{r}) = \frac{1}{\sqrt{L^d}} \sum_j e^{i\mathbf{k}\cdot\mathbf{R}_j} w_{\alpha}(\mathbf{r} - \mathbf{R}_j) \quad (\text{A.0.5})$$

The Wannier functions  $w_\alpha(\mathbf{r} - \mathbf{R}_j)$  are localized around minima  $\mathbf{R}_j$  of lattice. By further introducing the Fourier transformation between the  $\mathbf{k}$  space creation (annihilation) operations  $c_{\alpha\mathbf{k}\sigma}^\dagger$  ( $c_{\alpha\mathbf{k}\sigma}$ ) and real space creation (annihilation) operations  $c_{\alpha j\sigma}^\dagger$  ( $c_{\alpha j\sigma}$ ),

$$c_{\alpha j\sigma} = \frac{1}{\sqrt{L^d}} \sum_{\mathbf{k}} e^{i\mathbf{k}\cdot\mathbf{R}_j} c_{\alpha\mathbf{k}\sigma} \quad (\text{A.0.6})$$

$$c_{\alpha\mathbf{k}\sigma} = \frac{1}{\sqrt{L^d}} \sum_j e^{-i\mathbf{k}\cdot\mathbf{R}_j} c_{\alpha j\sigma} \quad (\text{A.0.7})$$

one may expand the field operators of Eq.(A.0.2) and Eq.(A.0.3) in terms of the Wannier functions

$$\psi_\sigma^\dagger(\mathbf{r}) = \sum_{\alpha,j} w_\alpha^*(\mathbf{r} - \mathbf{R}_j) c_{\alpha j\sigma}^\dagger \quad (\text{A.0.8})$$

$$\psi_\sigma(\mathbf{r}) = \sum_{\alpha,j} w_\alpha(\mathbf{r} - \mathbf{R}_j) c_{\alpha j\sigma} \quad (\text{A.0.9})$$



# Appendix B

## Peierls substitution

Here we show that the Hamiltonian with spin orbit coupling could be written in terms of the Peierls substitution. As shown in Eq.(2.4.3), the Hamiltonian with spin orbit coupling term in 1D is

$$H = \frac{1}{2m}(p_x - A)^2 - \frac{\hbar}{2}\sigma^x + \frac{\delta}{2}\sigma^z \quad (\text{B.0.1})$$

where  $A = -\hbar k_0 \sigma^x$ . The eigenfunctions of  $\frac{1}{2m}(p_x - A)^2$  can be expressed with the help of Bloch functions,

$$\tilde{\phi}_{\alpha k}(x) = e^{iAx/\hbar} \phi_{\alpha k}(x) \quad (\text{B.0.2})$$

$$(-i\hbar\partial_x - A)^2 = e^{iAx/\hbar} (-i\hbar\partial_x)^2 e^{-iAx/\hbar} \quad (\text{B.0.3})$$

the eigenequation of  $\frac{1}{2m}(p_x - A)^2$  is

$$\begin{aligned} \left[ \frac{(-i\hbar\partial_x - A)^2}{2m} + V(x) \right] \tilde{\phi}_{\alpha k}(x) &= e^{iAx/\hbar} \left[ \frac{(-i\hbar\partial_x)^2}{2m} + V(x) \right] e^{-iAx/\hbar} \phi_{\alpha k}(x) \\ &= E_{\alpha k} \tilde{\phi}_{\alpha k}(x) \end{aligned} \quad (\text{B.0.4})$$

where  $V(x)$  is the local-site potential. Hence, the Wannier function is

$$\tilde{w}_\alpha(x - x_j) = \frac{1}{\sqrt{L}} \sum_k e^{-ikx_j} \tilde{\phi}_{\alpha k}(x) = \frac{1}{\sqrt{L}} \sum_k e^{-ikx_j} e^{iAx/\hbar} \phi_{\alpha k}(x) \quad (\text{B.0.5})$$

$$= e^{iAx/\hbar} w_\alpha(x - x_j) \quad (\text{B.0.6})$$

It is clear that if spin-orbit coupling is small  $Aa \ll 1$ , then  $\tilde{w}_\alpha(x - x_j)$  is well defined, and will be localized at  $x = x_j$ . In second quantization, the tunneling  $\tilde{t}_{i,j}$  for the

lowest band becomes

$$\begin{aligned}
 \tilde{t}_{ij} &= - \int dx \tilde{w}^\dagger(x - x_j) \left[ \frac{(p_x - A)^2}{2m} + V(r) \right] \tilde{w}(x - x_i) \\
 &= - \int dx w^\dagger(x - x_j) e^{-\frac{iA(x-x_i)}{\hbar}} e^{\frac{iAx}{\hbar}} \left[ \frac{(p_x - A)^2}{2m} + V(r) \right] e^{-\frac{iAx}{\hbar}} e^{\frac{iA(x-x_i)}{\hbar}} w(x - x_i) \\
 &= t_{ij} e^{\frac{iA(x_j-x_i)}{\hbar}} = t_{ij} e^{-ik_0(x_j-x_i)\sigma^x}
 \end{aligned} \tag{B.0.7}$$

where  $\tilde{w}(x - x_j) = \begin{pmatrix} \tilde{w}_\uparrow(x-x_j) \\ \tilde{w}_\downarrow(x-x_j) \end{pmatrix}$ . Let us now consider spin-orbit Hamiltonian with the Zeeman fields  $\sigma^x$ ,  $\sigma^z$ . Since  $\sigma^x$  commutes with  $e^{-ik_0x\sigma^x}$ , we just consider the  $\sigma^z$  term. In second quantization, it is

$$\begin{aligned}
 \tilde{t}_{ij}^\delta &= - \int dx \tilde{w}^\dagger(x - x_j) \left( \frac{\delta}{2} \sigma^z \right) \tilde{w}(x - x_i) \\
 &= - \int dx \tilde{w}^\dagger(x - x_j) e^{-ik_0x\sigma^x} \frac{\delta}{2} (\cos(2k_0x)\sigma^z + \sin(2k_0x)\sigma^y) e^{ik_0x\sigma^x} \tilde{w}(x - x_i) \\
 &= - \int dx w^\dagger(x - x_j) e^{-ik_0x_j\sigma^x} \frac{\delta}{2} (\cos(2k_0x)\sigma^z + \sin(2k_0x)\sigma^y) e^{ik_0x_i\sigma^x} w(x - x_i) \\
 &= - \int dx w^\dagger(x - x_j) \frac{\delta}{2} (\cos(2k_0(x - x_j))\sigma^z + \sin(2k_0(x - x_j))\sigma^y) w(x - x_j)
 \end{aligned} \tag{B.0.8}$$

where only the leading on-site contribution term  $x_i = x_j$  is considered, and the following relations are used,

$$e^{-ik_0x_j\sigma^x} \frac{\delta}{2} \sigma^z e^{ik_0x_j\sigma^x} = \frac{\delta}{2} (\cos(2k_0a_j)\sigma^z - \sin(2k_0a_j)\sigma^y) \tag{B.0.9}$$

$$e^{-ik_0x_j\sigma^x} \frac{\delta}{2} \sigma^y e^{ik_0x_j\sigma^x} = \frac{\delta}{2} (\cos(2k_0a_j)\sigma^y + \sin(2k_0a_j)\sigma^z) \tag{B.0.10}$$

If the lattice potential is spin independent as well as the kinetic energy (equal masses),  $w_\uparrow(x - x_j) = w_\downarrow(x - x_j) = w_0(x - x_j)$ , we obtain

$$\begin{aligned}
 -\tilde{t}_{ij} &= \frac{\delta}{2} \sigma^z \int dy \cos(2k_0y) |w_0(y)|^2 + \frac{\delta}{2} \sigma^y \int dy \sin(2k_0y) |w_0(y)|^2 \\
 &= \frac{\delta}{2} \sigma^z \int dy \cos(2k_0y) |w_0(y)|^2
 \end{aligned} \tag{B.0.11}$$

where  $y = x - x_j$ . For weak spin-orbit coupling  $k_0 \ll 1$ ,  $\int dy \cos(2k_0y) |w_0(y)|^2 = 1$ . Hence, if the vector potential  $A = (-\hbar k_0^x \sigma^x, -\hbar k_0^y \sigma^y, 0)$ , the nearest hopping will transform as

$$t_x \rightarrow t_x e^{-ik_0^x a \sigma^x}, \quad t_y \rightarrow t_y e^{-ik_0^y a \sigma^y} \tag{B.0.12}$$

# Appendix C

## On-site interaction energies of dipolar bosons

Here we discuss on-site interaction energies of dipolar bosons in  $p$ -bands of zigzag optical lattice that may be realized by incoherent superposition of triangular lattice and an additional superlattice [22]. We will estimate the system parameters for the case of a quasi-2D square lattice  $V(\mathbf{r}) = V_0(\sin^2 \pi x/a + \sin^2 \pi y/a + \frac{V_0^z}{V_0} \sin^2 \pi z/a)$  and neglect the modification due to the additional superlattice. To simplify further the estimation we use the harmonic approximation and take  $V_0^z/V_0 = 2$  and  $V_0 = 25E_R$  (the optical lattice should be deep enough to neglect the tunneling of molecules in  $s$  orbitals), where  $E_R = \frac{\hbar^2 \pi^2}{2ma^2}$  is the recoil energy,  $m$  is the mass of molecule, and  $a = 0.5 \mu\text{m}$  (typical lattice constant for optical lattices). We note that the harmonic approximation overestimates the interaction energies and may even (for the case of average occupation of particles per site greater than 1) miss quantitative features [151]; however it may serve as a rough estimate of the interaction energies involved in the problem.

We divide the on-site interaction energies into a contact part and dipolar part,  $U_{\parallel(\perp)} = U_{\parallel(\perp)}^c + U_{\parallel(\perp)}^d$ . In the case of disoriented dipoles the dominant on-site contribution comes from the contact  $s$ -wave scattering: for bosons occupying the same orbital  $U_{\parallel}^c = \frac{4\pi a_s \hbar^2}{m} \int d\mathbf{r} p_\alpha^4(\mathbf{r}) \sim 0.5E_R$ , for  $s$ -wave scattering length  $a_s \sim 100a_0$ , with  $a_0$  being the Bohr radius. On-site interaction for bosons occupying orthogonal orbitals is  $U_{\perp}^c = \frac{4\pi a_s \hbar^2}{m} \int d\mathbf{r} p_x^2(\mathbf{r}) p_y^2(\mathbf{r}) = U_{\parallel}^c/3$ , the ratio  $U_{\perp}^c/U_{\parallel}^c = 1/3$

being independent of  $V_0^z/V_0$  in the harmonic approximation. To estimate the dipolar contribution in on-site energies we Fourier-transform the dipolar potential and use a similar approximation as discussed for the dipolar Bose gas in the spherical trap [118] as well as in the presence of an optical lattice [31]. For molecules with strong dipolar moment (of the order of Debye) on-site energy from dipolar interactions can be comparable to  $U_{\parallel}^c$ . As opposed to the case of contact interactions, the ratio  $U_{\perp}^d/U_{\parallel}^d$  depends on  $V_0^z/V_0$ . For the case  $V_0^z/V_0 = 2$  we get  $U_{\perp}^d/U_{\parallel}^d \simeq 4.43$ . Hund exchange is dominated by the contact interactions,  $J_H \sim U_{\parallel}^c/3$ . One can tune the model parameters in Eq.(5.2.3) from  $\alpha \simeq 3$ ,  $\Delta \gg 1$  (corresponding to the case of weakly polarized dipoles) to  $\alpha < 2$ ,  $\Delta < 1$  by aligning the dipoles perpendicular to the zigzag plane with an electric field.

# Acknowledgements

I would like to thank my PhD supervisors Prof. Luis Santos and Prof. Temo Vekua for giving me the chance to study in their groups and their help throughout my PhD research. I was very happy to learn from them, and enjoyed very much talking, discussing with them.

I would like to thank Prof. Alexei Kolezhuk, Prof. George Jackeli, Prof. Dario Poletti, Sebastian Greschner, and Juan Jaramillo for their fruitful collaboration, which helped and taught me a lot. I would like to especially thank Sebastian Greschner for translating the German abstract "Zusammenfassung".

I would like to thank Prof. Eric Jeckelmann, Dr. Xiaolong Deng, Frau Gitta Richter and all other members for their help to my research, my life in Hannover.

I would like to thank the support from Institute for Theoretical Physics, QUEST (Center for Quantum Engineering and Space-Time Research) and DFG Research Training Group (Graduiertenkolleg) 1729.



# List of Publications

## Publications

1. G. Sun, A.K. Kolezhuk, T. Vekua, "*Fidelity at Berezinskii Kosterlitz Thouless quantum phase transitions*", arXiv:1408.2739 (2014)
2. S. Greschner, G. Sun, D. Poletti, L. Santos, "*Density dependent synthetic gauge fields using periodically modulated interactions* ", accepted by Phys. Rev. Lett., arXiv:1311.3150 (2013)
3. G. Sun, T. Vekua, "*Topological order-by-disorder in orbitally degenerate dipolar bosons in zig-zag lattice*", Phys. Rev. B **90**, 094414 (2014)
4. G. Sun, A.K. Kolezhuk, L. Santos, T. Vekua, "*Ferromagnetic spin-orbital liquid of dipolar fermions in zigzag lattices*", Phys. Rev. B **89**, 134420 (2014)
5. G. Sun, J. Jaramillo, L. Santos, and T. Vekua, "*Spin-orbit coupled fermions in ladderlike optical lattices at half filling*", Phys. Rev. B **88**, 165101 (2013)
6. G. Sun, G. Jackeli, L. Santos, and T. Vekua, "*Exploring spin-orbital models with dipolar fermions in zigzag optical lattices*", Phys. Rev. B **86**, 155159 (2012)

Chapter 4 of this thesis is based on results published in 4 and 6; Chapter 5 is presented in 3; Chapter 6 is discussed in 5; Finally Chapter 7 is discussed in 1.

## Other publications of the author:

1. Gao-Yong Sun, Su-Peng Kou, "*Possible anomalous spin dynamics of the Hubbard model on a honeycomb lattice*", J. Phys.: Condens. Matter **23**, 045603 (2011)
2. Gao-Yong Sun, Su-Peng Kou, "*Quantum non-magnetic state near metal insulator transition - A possible candidate of spin liquid state*", Europhys. Lett., **87**, 67002 (2009)



# Curriculum Vitae

## Personal Information

Name: Gaoyong Sun

Phone: 00495117625888

Email: gaoyong.sun@itp.uni-hannover.de

Sex: Male

Citizenship: Chinese

## Education

09.2010 - present, PhD, Leibniz Universität Hannover, Germany.

09.2007 - 07.2010, M.Sc., Beijing Normal University, P. R. China.

09.2002 - 07.2006, B.Sc., Northwest University, P. R. China.

